A PASSIVE RFID TRANSPONDER USING HARMONIC GENERATION OF NONLINEAR TRANSMISSION LINES

A Dissertation

Presented to the Faculty of the Graduate School

of Cornell University

In Partial Fulfillment of the Requirements for the Degree of

Doctor of Philosophy

by

Fan Yu

August 2012

A PASSIVE RFID TRANSPONDER USING HARMONIC GENERATION OF NONLINEAR TRANSMISSION LINES

Fan Yu, Ph.D.

Cornell University 2012

In conventional passive RFID systems, the reader (interrogator) transmits signals to serve not only as an interrogation signal, but also as a power source to the tag (transponder). The continuous-wave (CW) signal to power up the passive tags inevitably couples to the receiver input as strong self-interference. In addition, the multipath reflection from the objects in view also results in strong in-band blocker. Both interfering signals present a major challenge to the reader's receiver design.

To avoid this problem, a frequency multiplier is proposed to generate a harmonic of the interrogation signal, providing a unique response signal among the leakage from the transmitter as well as the incidental backscatter from the linear objects in view. Instead of using the active frequency multiplier or diode doubler, we propose a novel frequency doubling transponder utilizing harmonic generation by integrated nonlinear transmission lines (NLTLs), where the local data signal on the transponder is modulated onto the second harmonic of the interrogating carrier. By modulating the bias voltage of the NLTLs, the transponder is capable of Amplitude Shift Keying (ASK), Phase Shift Keying (PSK) and other similar coding schemes.

This dissertation discusses (1) the introduction of passive RFID tag and (2) the harmonic generation theory of nonlinear transmission lines, (3) the design of reflective nonlinear transmission lines, (4) a study of the wireless link between the reader and the tag, (5) analog modulation of NLTL based capacitive sensor tag, as well as (6) digital modulation of NLTL based passive RFID tag. As a related effort, we also

append a similar usage of taper-section NLTL in ultra-high frequency transmitters driven by baseband signal power. Finally, we summarize the our contribution and reflect on the possible future directions.

BIOGRAPHICAL SKETCH

Fan Yu was born in the south part of China. She grew up in Shangrao of Jiangxi province and attended University of Science and Technology of China, where she received her B.E degree in 2007. After finishing her undergraduate studies, she joined the Ph.D. program at the school of Electrical and Computer Engineering, Cornell University in Ithaca, NY. In the summer of 2010, she was a Research Intern with GE Global Research, Niskayuna, NY. Her research interests include RFID systems, ultra-wideband radio, nonlinear circuits and flexible electronics.

To my parents, Guolin Yu and Yongjuan Liu

ACKNOWLEDGMENTS

This work would not have been possible without the help and support from many wonderful people.

I would like to express my deepest gratitude to my Ph.D. supervisor, Prof. Edwin C. Kan, for his excellent guidance, caring, patience. Throughout my thesis-writing period, he provided encouragement, sound advice, good teaching, good company, and lots of good ideas. I would have been lost without him. Thank you for always being supportive as a mentor, and as a friend. It is also my great honor to have Prof. Ehsan Afshari and Prof. Alyssa Apsel on my Ph.D. committee. Their comments and suggestions provided new insights and helped reevaluate my work from fresh viewpoints.

I would like to thank Keith G. Lyon for being my mentor in the project. His comprehensive work and valuable comments laid a solid foundation for my research. I am also grateful to my group members: Jonathan, Shantanu, Krishna, Joshua, Sarah, Lieh-Ting, Xiaoyang, Philip, Yuan, Yinglei, Yunfei, and Kshitij for their support. I would also like to thank other fellow graduate students at Cornell: Bo Xiang, Rajeev Dokania, Xiao Wang, Meng Wang, Emma Wang, Guansheng Li, Wooram Lee for their friendship and help.

Special thanks to my parents for their unconditional love. They always taught me to be honest, truthful and diligent, which I benefit in my whole life. They also tried their best to provide a good growth environment for me and supported me in my decisions. Finally, I thank my husband, Xiaohang Li, who kept me company along the way, shared my joys and worries, and gave me lots of support.

TABLE OF CONTENTS

LIST OF FIGURES

LIST OF TABLES

CHAPTER 1

INTRODUCTION

The automatic and simultaneous identification, localization, and targets tracking using electromagnetic radiation started mainly as a military application in radar systems. In the early 1970s, commercial tracking of large and expensive goods emerged, followed by smaller items by the end of the 20th century [1]. Since then, Radio-frequency identification (RFID) became almost ubiquitous in commercial applications, which uses radio-frequency electromagnetic fields to transfer data from a tag to a reader.

The applications of RFID are widespread. Inductive RFID systems, that operate at low-frequency (LF: 125 – 134.2 kHz and 140-148.5 kHz) and high-frequency (HF: 13.56 MHz) bands are widely adopted, especially for access control, where short operational range and low rate are sufficient [2]. For example, Near Field Communication (NFC) is a set of standards to establish communication among the smart phones and similar devices at a distance of 4 cm or less, based on RFID systems at 13. 56 MHz. In recent years, the ultra high-frequency (UHF: 868 MHz – 927 MHz) band has also been utilized for RFID [3-6]. Unlike the near-field-based systems at LF and HF, the UHF RFID systems are radiating traveling waves and they offer an operational range of a few meters with low-cost battery-less transponders. This makes UHF RFID desirable for the applications like packages tracing and inventory control. For some applications, such as the localization of the transponders, microwave frequencies at the 2.45 GHz industrial-scientific-medical (ISM) band are used [7, 8].

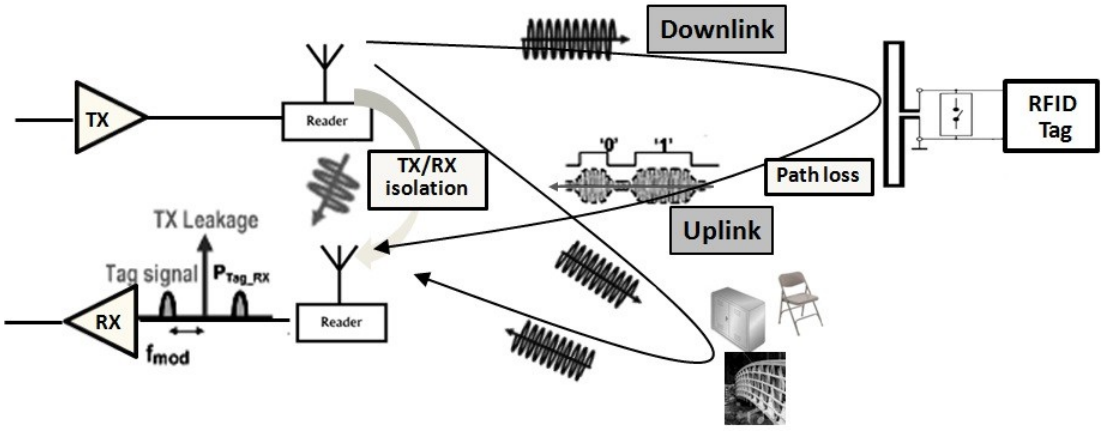

Figure 1-1 System diagram for conventional RFID system with backscattering.

1.1 Conventional RFID System

Nowadays, there is an urgent need to develop passive millimeter-scale RFID transponders (including antenna) for various embedded sensors [2]. Miniaturization of the tag antenna often severely compromises the reading range as the antenna aperture is reduced with respect to the areas of other scatters, and hence the signal-to-noise (S/N) ratio is severely degraded. A wide variety of possible solutions had been proposed, mainly in the way of simple backscatters with amplitude [3], phase [4], or a controlled time delay [9]. In such systems, the RFID reader transmits the continuous-wave (CW) signal to power up and collects reflected waves from the RFID tag. The block diagram of a conventional UHF RFID system is shown in Figure 1-1. The RFID tag communicates to the reader by modulating its tag impedance with data rate f_{mod}, which reflects a portion of the reader signal back to the reader.

From Figure 1-1, it can be found that the reflected signal is received by the reader along with a simultaneous leakage from the transmitter's CW signal as well as the multipath reflection from the nearby objects. Both transmitter's leakage and the multipath reflection, which act as large in-band blockers, are very close to the desired signal in frequency band (only hundreds of kHz frequency separation). The small separation between the blocker and signal frequencies make it very difficult to use high-Q bandpass filter like surface acoustic wave (SAW) filters to reject blocker without attenuating the data signal. Typically, for the off-chip circulator with 20 dB isolation between TX/RX, the TX signal present at the receiver input is greater than +10 dBm. For a passive RFID tag, the strength of the backscattered signal from tag is usually smaller than –85 dBm at the receiver input for maximum range of coverage. As a result, the biggest challenge in RFID reader design, is receiving a weak tag signal less than –80 dBm over several meters along with strong self-interference larger than +10 dBm, which implies an input dynamic range greater than 90 dB.

1.2 Existing Non-Self-Jamming RFID Tags

To solve this self-interference problem, two different communication links can be employed in the tag to provide a unique response signal among the leakage from the transmitter as well as the multipath reflection. According to the required power consumption, the non-self-jamming RFID tags can be categorized as either active or passive.

For the active type, the simplest method is to use a LC oscillator to generate the uplink response operating at different frequency, which is easily to be distinguished from the interrogation signal in the downlink. For wireless applications, the operating frequency of oscillator should be larger than hundreds of MHz to transmit over several

meters. However, the circuit dissipates more than 1 mW DC power and requires a relatively stable 1V supply voltage [10]–[12]. For example, a recent proposal uses an active injection-locked LC oscillator to generate the 2nd harmonic of the interrogation signal with active current of the oscillator at more than 650 μA [12]. In a small passive RFID system, the power harvested by the RF-to-DC rectifier in the tag is limited to tens of μW, which is insufficient to power up the active oscillator. To reduce the power consumption, there are some tags proposing the power-efficient UWB signal in the uplink due to the low duty-cycle of transmitted signal [13] – [14], which will also increase the data rate in tag-to-reader communication. However, the power consumption for the active UWB transmitter is still not usually affordable by passive RFID tag without any external energy storage component. For example, the UWB transmitter of [13] consumes 91.8 μW at a 10 MHz pulse rate and needs a 211 nF off chip storage capacitance to support the peak current. Many of the active-type RFID system then resort to battery-assisted operation [12, 17], which can severely undermine system size, lifetime and maintenance. More of the RF-to-DC power scavenging schemes will be further analyzed in Chap. 6.

In contrast to the active method, the passive one utilizes a nonlinear device to generate a harmonic or sub-harmonic of the interrogation signal without consuming any DC power. It is also widely called harmonic RFID tag [15] – [18]. Figure 1-2 shows the system block diagram for the passive harmonic RFID tag. Since there is no additional power needed, the passive harmonic tags can relax the downlink distance from the reader to the tag, which is usually a big constraint limiting the communication distance for the active mode even with the assistance of a RF-to-DC convertor. For example, assuming the RF frequency f is 950 MHz, the distance d is 1 m, and the tag antenna gain G_r is 2 dBi, the path loss is calculated to be 32 dB. When the effective isotropic radiation RF power of the reader is 4 W_{EIRP} (36 dBm), which is

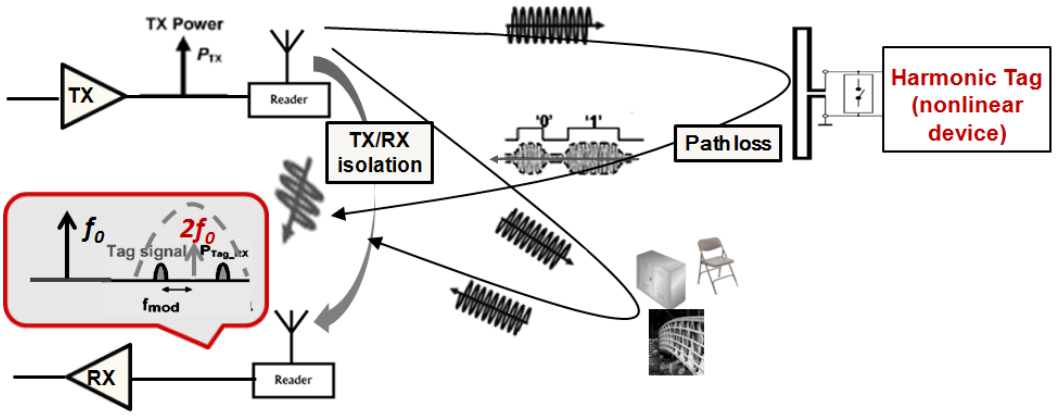

Figure 1-2 System block diagram for harmonic RFID tag.

the maximum possible output power complying with USA and Japanese regulations of the UHF band, the received power at the tag is around 4 μW. With a typical RF-to-DC efficiency around 20 % [26], the available supply power for the tag would be 1.2 μW, which is still far from the minimum required power on the order of hundreds of μW by the active harmonic generation [12]. To operate correctly, the active mode is only possible when the distance is less than 10 cm. For the passive harmonic generation, if we assume a relatively large conversion loss of 20 dB for the nonlinear device with the received input power of 6 dBm, the 2nd harmonic power at the reader would be around –50 dBm, which guarantees correct detection with the typical reader sensitivity of –85 dBm.

Several approaches have been proposed for harmonic [15]–[16] or subharmonic [17] generated by a single diode. For diode frequency doublers in [15]–[16], the input and output matching networks designed at fundamental and harmonic frequencies consume large amount of circuit area and introduce additional losses. In addition, the design in [16] employed a varactor diode to modify the impedance matching, leading to an On-Off Keying (OOK) modulation. However, the tunable range of the input

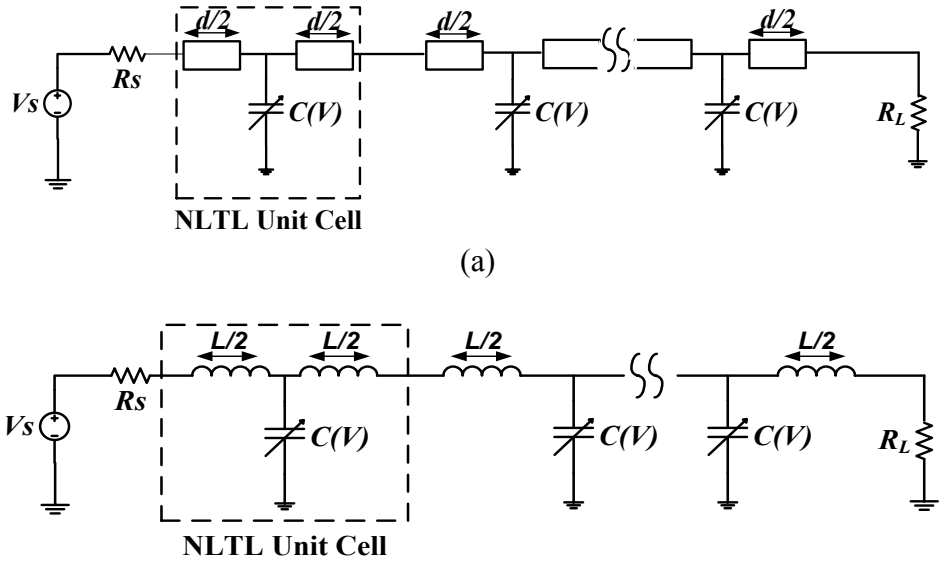

Figure 1-3 Circuit model (a) semi-discrete configuration (b) discrete configuration of periodically loaded NLTLs.

impedance is limited by changing the capacitance value of the varactor. In [16], 17 V bias voltage difference with 70% capacitance variation gives only 10 dB conversion gain difference. Another approach [17] used the diode as a frequency mixer to generate the sideband signal of second harmonic. The circuit was advantageous when an interrogator received reflections of its own transmitted harmonics. However, the mixing product is basically a third-order term, which has lower conversion efficiency compared with second-order harmonic. Besides, the generation of the signal to be up converted also required DC power. In this proposal, 1 mA operating current from 1.5 V battery was consumed to generate the 10 MHz sideband signal.

1.3 Motivation of NLTL based RFID Tag

Nonlinear transmission lines (NLTLs) have been used for many years in GaAs technologies for harmonic generation and impulse generation in very high frequency applications [19] – [20]. Recent demonstrations of NLTLs fabricated in CMOS technology open the door to the application in new areas such as interconnects and impulse radio transmitters using the NLTL's wave shaping and impedance tuning properties [21] – [23].

In this dissertation, we propose a novel frequency doubling transponder utilizing harmonic generation by integrated nonlinear transmission lines (NLTLs), where the local data signal on the transponder is modulated onto the second harmonic of the interrogating carrier. A NLTL is most often implemented as a transmission line where the shunt capacitance varies with voltage, which can be in either semi-discrete or discrete configuration as shown in Figure 1-3. The periodic nature makes NLTL act as a low-pass filter and its cutoff frequency is the Bragg frequency.

As opposed to the single-diode frequency multipliers, which exhibit reactive input impedances, the positive and real impedances of the NLTLs provide easier broadband matching [18] –[20]. For the diode multiplier, a reflector for fundamental frequency f_0 (like $\lambda/4$ transmission line at f_0) is usually connected at the output matching network to reflect the fundamental signal back so that all the input power can flow into the varactors without leaking into the output [24] - [25]. However, for operation frequency lower than 20 GHz, the TL would have a length in millimeters, which is not only area consuming but also introduces significant losses to the generated 2^{nd} harmonic. The multiple reflections at the transmitting antenna also make phase information unusable, which constrains the data modulation method. In addition, for the NLTLs, the Bragg frequency can effectively limit the power spilling to higher harmonics, and the number

of stages provides additional degree of freedom to control the phase of the generated 2nd harmonic signal for phase-match conditions. These additional design factors can enhance the conversion efficiency in comparison with the lump diode with TL reflectors.

1.4 Components and Options to Enable Digital ID

In NLTLs, the nonlinearity can come from either shunt capacitance or series inductance, which is dependent on the voltage or current. Common designs use a conventional transmission line periodically loaded with Schottky diodes or MOS capacitance (varactors) for high frequency application. Considering the impractical area required by the distributed NLTLs with large number of sections, the series inductance is usually preferred in low frequency less than 20 GHz. For the shunt capacitance, we use the nonlinearity of the varactors for the operation. Since the varactor is a major carrier device, its intrinsic frequency response is determined by the dielectric relaxation time less than 1 ps in moderately doped silicon. Therefore, the NLTLs offer the possibility for the extreme high frequency applications.

Utilizing the power and phase of second harmonic dependence on the bias voltage or the terminating varactors of the NLTLs, the transponder is capable of Amplitude Shift Keying (ASK), Phase Shift Keying (PSK) and other similar coding schemes for digital ID generation. The designer has considerable flexibility to choose the coding scheme based on the specific applications. More details about the modulation scheme will be discussed in Chapter 6.

1.5 Thesis Organization

This dissertation intends to discuss the designs of the passive harmonic RFID tag using NLTLs with great details. A thorough analysis of the harmonic generation, impedance matching and data modulation abilities of the NLTLs will help the design of the NLTL based RFID tags for various sensor applications.

Chapter 2 presents the harmonic generation theory of the NLTLs. Based on the small signal model, different design parameters have been optimized to achieve the maximum harmonic output power. In Chapter 3, we will introduce the reflective NLTLs to save one antenna area for the tag and also reduce the transmission line size. After that, Chapter 4 will demonstrate the wireless link between the reader and the tag based on both of the matched and the reflective NLTLs.

Chapter 5 presents the design of the NLTL RFID sensor tag with analog phase modulation. To offer broader applications, Chapter 6 discusses the digital modulation of NLTL based RFID tag. As a related effort, we append a similar usage of taper-section NLTL in ultra-high frequency transmitters driven by baseband signal power in Chapter 7.

Finally, Chapter 8 concludes the dissertation with the contributions, the common traps in this work and also suggestion for future work.

REFERENCES

[1] D. M. Dobkin, *The RF in RFID*. New York: Elsevier, 2007, 13: 978-0750682091.

[2] K. Finkenzeller*, RFID Handbook*, *2nd Ed*. New York: Wiley, 2003.

[3] J. P. Curty, N. Joehl, C. Dehollain, and M. J. Declercq, "Remotely powered addressable UHF RFID integrated system," *IEEE J. Solid-State Circuits*, vol. 40, no. 11, pp. 2193-2202, Nov. 2005.

[4] U. Karthaus, and M. Fischer, "Fully integrated passive UHF RFID transponder IC with 16.7-μW minimum RF input power," *IEEE J. Solid-State Circuits*, vol. 38, no. 10, pp. 1602-1608, Oct. 2003.

[5] R. Barnett, G. Balachandran, S. Lazar, B. Kramer, G. Konnail, S. Rajasekhar, V. Drobny, "A pssive IHF RFID transponder for EPC Gen 2 with -14 dBm sensitivity in 0.13 μm CMOS," *ISSCC Dig. Tech. Papers,* pp. 582-584, Feb. 2007.

[6] L. Catarinucci, R. Colella, and L. Tarricone "A cost effective UHF RFID tag for transmission of generic sensor data in wireless sensor networks," *IEEE Trans. Microwave Theory and Tech.*, vol. 57, no. 5, pp. 1291-1296, May 2009.

[7] W. G. Yeoh, et al, "A CMOS 2.45 GHz radio frequency identification tag IC with read/write memory," *IEEE RFIC Symp. Dig.*, pp. 365-368, June 2005.

[8] S. Robinet, B. Gomez, N. Delorme, "A CMOS-SOI 245 GHz remote powered sensor tag," *ISSCC Dig. Tech. Papers*, pp. 198-199, Feb. 2008.

[9] A. Chamarti, and K. Varahramyan, "Transmission delay line based ID generation circuit for RFID applications," *IEEE Microw. Wireless Compont. Lett*., vol. 16, no. 11, pp. 286–287, 2006.

[10] M. Tiebout, “Low-power low-phase-noise differentially tuned quadrature VCO design in standard CMOS,” *IEEE J. Solid-State Circuits*, vol. 36, no. 7, pp. 1018-1024, Jul. 2001.

[11] L. H. Lu, H. H. Hsieh, and Y. T. Liao, “A wide tuning-range CMOS VCO with a differential tunable active inductor,” *IEEE Trans. Microwave Theory and Tech.*, vol. 54, no. 9, pp. 3462-3468, Sep. 2006.

[12] F. Kocer, and M. P. Flynn, “A new transponder architecture with on-chip ADC for long-range telemetry applications,” *IEEE J. Solid-State Circuits*, vol. 41, no. 5, pp. 1142–1148, May 2006.

[13] M. B. Nejad, D. S. Mendoza, Z. Zou, S. Radiom, G. Gielen, L. Zheng, H. Tenhunen, "A remote-powered RFID tag with 10 Mb/s UWB uplink and -18.5 dBm sensitivity UHF downlink in 0.18 um CMOS," *ISSCC Dig. Tech. Papers*, pp. 198-199, Feb. 2009.

[14] M. Pelissier, J. Jantunen, B. Gomez, J. Arponen, G. Masson, S. Dia, J. Varteva, and M. Gary, "A 112 Mb/s full duplex remotely-powered impulse-UWB RFID transceiver for wireless NV-memory applications," *IEEE J. Solid-State Circuits*, vol. 46, no. 4, pp.916-927, Apr. 2011.

[15] M. Bouthinon, J. Gavan, and F. Zadworny, “Passive microwave transponder, frequency doubler for detecting avalanche victims,” in *Proc. 10th European Microwave Conf.*, pp. 579-583, Sept. 1980.

[16] S. M. Aguilar, and T. M. Wellerl, “Tunable harmonic re-radiator for sensing applications,” in *IEEE MTT-S International Microwave Symposium Digest*, vol. 2, pp. 1565–1568, June 2009.

[17] C. W. Pobanz, and T. Itoh, “A microwave noncontact identification transponder using subharmonic interrogation,” *IEEE Trans. Microwave Theory and Tech.*, vol. 43, no. 7, pp. 1673-1679, July 1995.

[18] F. Yu, K. G. Lyon, and E. C. Kan, "Harmonic generation from integrated nonlinear transmission lines for RFID applications," in *IEEE MTT-S International Microwave Symposium Digest*, June 2010.

[19] E. Carman, M. Case, M. Kamegawa, R. Yu, K. Giboney, and M. Rodwell, "V-band and w-band broadband, monolithic distributed frequency multipliers," in *IEEE MTT-S* International *Microwave Symposium Digest*, vol. 2, pp. 819–822, June 1992.

[20] D. Salameh, D. Linton, "Microstrip GaAs transmission-line (NLTL) harmonic and pulse generators", *IEEE Microwave Theory and Tech*., vol. 47, no. 7, pp. 1118-1122, 1999.

[21] P. Wang, G. Pei, and Edwin C. Kan, "Pulse wave interconnect," *IEEE Trans. VLSI Syst.* , vol. 12, no. 5, pp. 453 – 463, 2004.

[22] J. Kim, W. Ni, and Edwin c. Kan, "A novel global interconnect method using nonlinear transmission lines," *Custom Integrated Circuits Conference (CICC)*, 2005, pp 617-620, 18-21, Sept. 2005.

[23] Keith G. Lyon, Fan Yu, and Edwin C. Kan, "A UWB-IR transmitter using frequency conversion in nonlinear transmission lines with 16 pJ/pulse energy consumption," *IEEE Trans. Microw. Theory Tech.*, vol.58, no. 12, pp. 3617–3625, Dec. 2010.

[24] C. Mao, C. Nallani, S. Sankaran, E. Seok and K. K. O, "125-GHz diode frequency doubler in 0.13-μm CMOS," *IEEE J. Solid-State Circuits*, vol. 44, no. 5, pp. 1531-1538, May 2009.

[25] U. R. Pferiffer, C.Mishra, R. M. Rassel, S. Pinkett, and S. K. Reynolds, "Schottky barrier diode circuits in silicon for future millimeter-wave and Terahertz applications," *IEEE Trans. Microw. Theory Tech.*, vol.56, no. 2, pp. 364–371, Feb. 2008.

[26] T. Umeda, et al, “A 950 MHz rectifier circuit for sensor networks with 10 m distance,” *ISSCC Dig. Tech. Papers*, pp. 256-257, Feb. 2005.

CHAPTER 2

NLTL BASED RFID TAG

The conventional right-hand (RH) nonlinear transmission line (NLTL) can be implemented with a ladder of series inductances and shunt capacitances as the circuit model. For RH NLTLs, the spectrum of the input sinusoidal wave at the TL output contains the fundamental frequency together with its higher harmonics, whose amplitudes decay with frequency due to the low-pass filter property. There is another category of the NLTLs, also known as left-hand (LH) NLTLs, which consists of series capacitances and shunt inductances. Harmonic generation in a LH NLTL is possible in a higher frequency range than in RH NLTL because of the high-pass nature of the structure. As any non-ideal transmission lines, both of the RH and LH s have three fundamental characteristics, which are nonlinearity, dispersion, and dissipation. These properties define its interface and propagation characteristics along with other parameters such as impedance and length. This work focuses on the harmonic generation properties of RH NLTL, which is mainly limited by the nonlinearity of the varactors, the dispersion and dissipation.

2.1 Semi-Discrete and Lumped-Element Models

For high-frequency applications, NLTLs often use a section of conventional transmission line as the series inductance due to higher quality factor than that of a lumped inductor. This configuration may be regarded as a transmission line periodically loaded with voltage-variable capacitors (varactors), forming the unit cell in Figure 2-1. Thus, only the varactors are lumped, or discrete, elements, while the rest

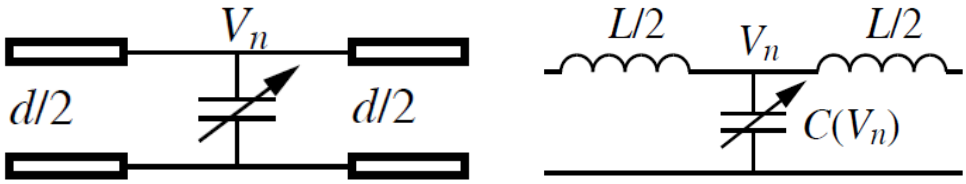

(a) (b)

Figure 2-1 Circuit models for unit cell of (a) semi-discrete and (b) lumped-element NLTLs.

of the device is a distributed, periodic structure. To determine characteristic impedance and dispersion relationships for an arbitrary reciprocal network having the transmission matrix:

$$\begin{bmatrix} A & B \\ C & D \end{bmatrix} \tag{2.1}$$

For a conventional transmission line such as coplanar waveguide (CPW) [1], the propagation constant γ and characteristic impedance Z_{ABCD} can be determined from $\cosh(\gamma d) = (A+D)/2$ and $Z_{ABCD} = \sqrt{B/C}$.

For the lossless semi-discrete NLTL cell (Figure 2-1(a)), the characteristic ABCD matrix of the cell inductance is

$$\begin{bmatrix} A & B \\ C & D \end{bmatrix} = \begin{bmatrix} \cos\left(\frac{\omega d}{2v}\right) & jZ_0 \cos\left(\frac{\omega d}{2v}\right) \\ \frac{j}{Z_0}\cos\left(\frac{\omega d}{2v}\right) & \cos\left(\frac{\omega d}{2v}\right) \end{bmatrix} \cdot \begin{bmatrix} 1 & 0 \\ j\omega C_0 & 1 \end{bmatrix} \cdot \begin{bmatrix} \cos\left(\frac{\omega d}{2v}\right) & jZ_0 \cos\left(\frac{\omega d}{2v}\right) \\ \frac{j}{Z_0}\cos\left(\frac{\omega d}{2v}\right) & \cos\left(\frac{\omega d}{2v}\right) \end{bmatrix} \tag{2.2}$$

and results in the dispersion relation and Block impedance:,

$$\cos(\beta) = \cos\left(\frac{\omega d}{v}\right) - \frac{\omega Z_0 C_0}{2}\sin\left(\frac{\omega d}{v}\right) \tag{2.3}$$

and

$$Z_{NLTL} = \sqrt{\frac{\sin\left(\frac{\omega d}{v}\right) + \frac{\omega Z_0 C_0}{2}\left(\cos\left(\frac{\omega d}{v}\right) - 1\right)}{\sin\left(\frac{\omega d}{v}\right) + \frac{\omega Z_0 C_0}{2}\left(\cos\left(\frac{\omega d}{v}\right) + 1\right)}} \tag{2.4}$$

where β is the propagation constant for the NLTL cell, d is the physical length of line, ω is the angular frequency, v is the phase velocity of the CPW, Z_0 is the characteristic impedance of the transmission line, and C_0 is the loading capacitance when V_{bias} = 0 V.

Using the lumped LC equivalent of the NLTL cell (Figure 2-1(b)), much simpler ABCD matrices:

$$\begin{bmatrix} A & B \\ C & D \end{bmatrix} = \begin{bmatrix} 1 & j\omega\frac{L}{2} \\ 0 & 1 \end{bmatrix} \cdot \begin{bmatrix} 1 & 0 \\ j\omega C & 1 \end{bmatrix} \cdot \begin{bmatrix} 1 & j\omega\frac{L}{2} \\ 0 & 1 \end{bmatrix} \tag{2.5}$$

This results in the dispersion

$$\cos(\beta) = 1 - \frac{\omega^2 LC}{2} \tag{2.6}$$

and the impedance

$$Z_{NLTL} = \sqrt{\frac{L}{C} - \frac{\omega^2 L^2}{4}} \tag{2.7}$$

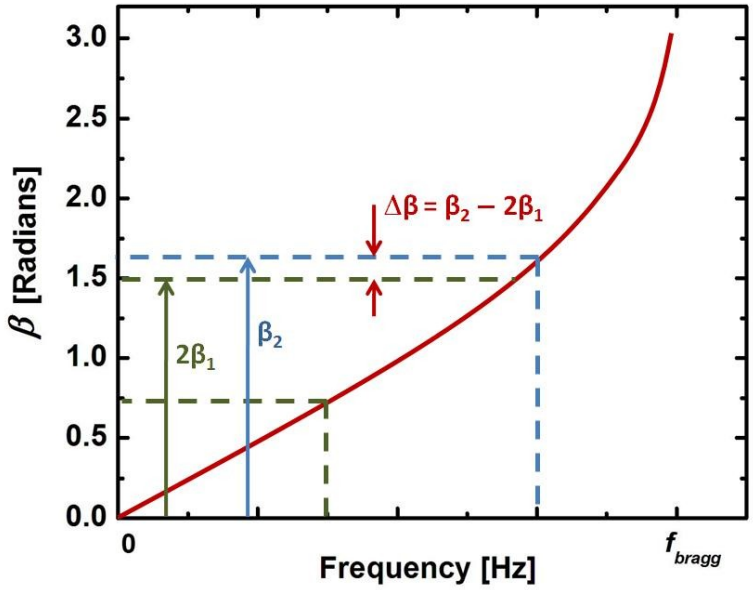

Figure 2-2 Dispersion diagram for the lumped-element model of a NLTL unit cell (β_1 and β_2 are the phase constants of the fundamental and 2nd harmonic signals).

From (2.3) and (2.6), both dispersion relations exhibit low pass characteristics, and the signals at frequencies above the low pass corner are strongly attenuated. This low pass corner is called the Bragg frequency since the reflections from this one-dimensional electrical lattice bear a similarity to the reflections seen in X-ray scattering in a periodic crystal lattice [5]. Figure 2-2 shows the dispersion diagram of the lumped LC model of the typical NLTL unit cell. From Figure 2-2, it can be found that the propagation factor $\beta = \pi$ at the Bragg frequency f_{bragg}. It is easy to determine that $\omega_B = 2/\sqrt{LC}$ with (2.6). Due to the discreteness of the artificial transmission lines, the dispersion is non-negligible and results in the phase shift between the fundamental signal and the second harmonic signal, shown in Figure 2-2. The phase shift will affect the conversion efficiency and phase modulation.

2.2 Small Signal Model for Harmonic Generation

To analyze their small-signal harmonic generation characteristics, an analytical expression [2] is derived for the harmonic amplitude in the NLTLs. Assuming negligible resistive/substrate losses and impedance matching at the source port, the amplitude of *m*-th harmonic in the *n*-th section of the NLTL biased at V_{bias} is:

$$V_m(n) = \frac{1}{2} K_m V_0^{\,m} \beta_m n F(\varphi)\, e^{-j\beta_m n} \tag{2.8}$$

where V_0 is the amplitude of the fundamental wave excited at the input port; β_m is the per-stage propagation constant of *m*-th harmonic; K_m is the factor describing the nonlinear C-V characteristics:

$$K_m = \frac{q^{(m)}(V_{bias})}{m! q'(V_{bias})} \tag{2.9}$$

where $q(V)$ is the charge on nonlinear capacitance and $F(\varphi)$ is a coherence function defined as:

$$F(\varphi) = \frac{\sin\dfrac{(m\beta_1 - \beta_m)n}{2}}{\dfrac{(m\beta_1 - \beta_m)n}{2}} = \frac{\sin(\varphi/2)}{\varphi/2} \tag{2.10}$$

$F(\varphi)$ passes through zero for $\varphi = 2k\pi$, which defines the "coherence length" of the interaction from the fundamental wave to its harmonics as:

$$N_c = \frac{2\pi}{\left|\beta_m - m\beta_1\right|} \tag{2.11}$$

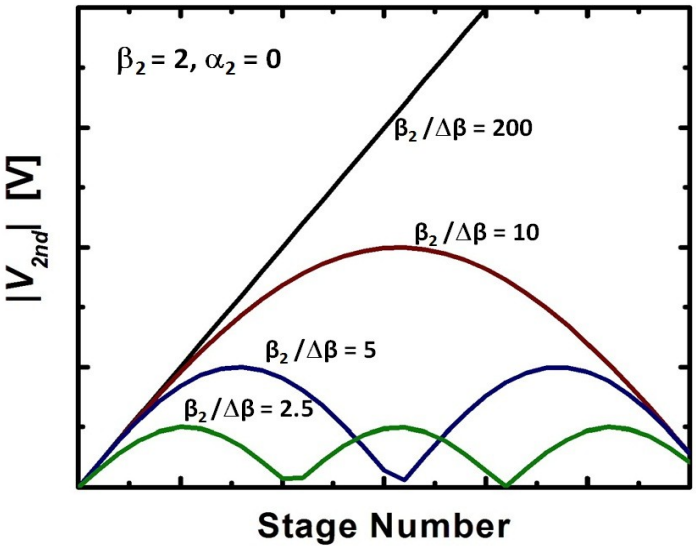

Figure 2-3. The phase-match effect on the growth of harmonics amplitude with the section number.

The magnitude of m-th harmonic V_m is plotted as a function of n in Figure 2-3. It can be seen that V_m is a periodic function of the stage number n and the period is determined by the dispersion characteristics. In the case of perfect phase-match where $|\beta_m - m\beta_1| = 0$, the magnitude of harmonics grows linearly with increasing n. In the case of phase mismatch, where $|\beta_m - m\beta_1| \neq 0$, for $n < N_{opt}$, where $N_{opt} = 0.5N_c$, the fundamental frequency and m-th harmonic propagate together and interfere constructively. Especially when $n < 0.25N_c$, V_m grows almost linearly with n. At $n = N_{opt}$, V_m reaches its maximum. For weak dispersion, where $|\beta_m - m\beta_1|$ is small, the coherence length is longer, which gives rise to higher harmonic conversion efficiency.

In addition to coherence length, V_m is also proportional to β_m. For NLTLs with cutoff frequency f_{bragg}, β_m is small in the low frequency range, exhibiting weak dispersion. When the operating frequency approaches f_{bragg}, β_m tends toward π, but the coherence length is decreased due to strong dispersion in the proximity of f_{bragg}. The

combined effects will determine the input frequency with maximal conversion efficiency.

Considering the transmission line and substrate losses, the amplitude of m-th harmonic in the n-th section of the NLTL biased at V_{bias} is:

$$\left|V_m(n)\right| = \left| K_m V_0^{\,m} \frac{\beta_m}{\beta_m - m\beta_1} \sin\frac{(m\beta_1 - \beta_m)n}{2} e^{-\alpha_m n} \right| \tag{2.12}$$

2.3 Design Parameters Optimization

From (2.12), several parameters will affect the efficiency of harmonic generation of the NLTL, such as n, V_0, V_{bias}, etc. For a given process, the designers have more freedom to control the stage number n, the Bragg frequency f_{bragg} and the bias point V_{bias}.

2.3.1. The stage number *n*

V_m is a periodic function of the stage number n in the lossless case. With pure TEM waves where $|\beta_m - m\beta_1| = 0$, the magnitude of harmonics always grows linearly with increasing n. When $|\beta_m - m\beta_1| \neq 0$, for $n < \pi/(\beta_m - m\beta_1)$, the fundamental frequency and m-th harmonic propagate together and interfere constructively. Especially when $n < 0.5\pi/(\beta_m - m\beta_1)$, V_m grows almost linearly with n. After n passes $\pi/(\beta_m - m\beta_1)$, the two waves get out of phase to result in destructive interference. Considering the loss of transmission line and varactor, the propagating harmonic wave would be a combined process of growing with n periodically and attenuating exponentially at the same time.

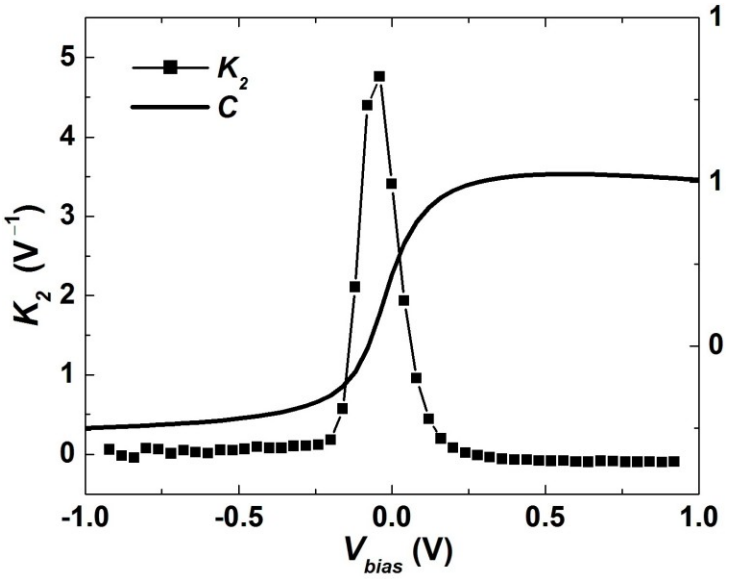

Figure 2-4 Extracted second-order nonlinearity K_2 and C-V characteristic for a typical nMOS varactor in IBM 8RF 0.13 μm CMOS process.

Thus, there exists an optimal section number n for the highest conversion efficiency. By differentiation of (2.12), one finds that:

$$n_{opt} = \left| \frac{2}{\beta_m - m\beta_1} \arctan \frac{\beta_m - m\beta_1}{2\alpha_m} \right| \tag{2.13}$$

2.3.2. The Bragg frequency f_{bragg}

In addition to section number n, V_m is also related to β_m. For NLTLs with Bragg frequency f_{bragg}, β_m is small in the low frequency range, while exhibiting weak dispersion. When the operating frequency approaches f_{bragg}, β_m increases toward π, but $\sin\left((\beta_m - m\beta_1)n/2\right)/\left(\beta_m - m\beta_1\right)$ is decreased due to strong dispersion in the proximity of f_{bragg}. The combined effects will determine the input frequency with maximal

conversion efficiency for certain f_{bragg}. In RFID design domain, f_{bragg} needs to be chosen carefully for a given input frequency transmitted by the interrogator.

2.3.3. The bias point V_{bias}

By varying the bias point of the varactors, K_m would have different values that change amplitude of output harmonic. In Figure 2-4, the extracted second-order nonlinearity K_2 for a typical nMOS varactor in IBM 8RF 0.13 μm CMOS process is shown. It is easy to find that the optimal bias point should be at $V_{bias} = 0$ where K_2 shows a maximum value. To get a stable zero bias voltage, a large capacitance is needed to filter out the unwanted high frequency components. However, the tags usually have the limitation of the stabilizing capacitance value due to the size and weight consideration. In this case, the differential NLTL appears advantageous because it has accurate definition of the ground potential without the use of external capacitance.

2.4 Design Examples

2.4.1. Simulation results

To demonstrate the efficiency of harmonic generation under low input-power level, three NLTLs are designed and simulated. Design 1 is based on lumped inductors with $f_{bragg} = 10$ GHz. Designs 2 and 3 are based on distributed high-impedance coplanar stripline (CPS) at the same $f_{bragg} = 25$ GHz but with different dimensionless parameter $k = (Z_0 / Z_{NLTL})^2 - 1$ [3]. The choice of NLTL configuration mainly depends on the frequency range. Discrete NLTLs are usually preferred in the low frequency range for

Parameter	Design 1	Design 2	Design 3
f_{bragg}	10 GHz	25 GHz	25 GHz
Z_0	/	143 Ω	102 Ω
k	∞	8	8
d	/	540 μm	788 μm
C_0	350 fF	194 fF	176 fF
n	10	10	10
L	1.45 nH	/	/

Table 2-1 NLTL harmonic generator parameters. The capacitance values are taken at a bias of $V_{gs} = 0$ V.

the compact size, while transmission-line based NLTLs are chosen due to their higher Q factor at high frequency.

The parameters of three NLTL designs are given in Table 2-1, where d and Z_0 are the section length and the characteristic impedance, respectively. To characterize the transmission loss of CPS in the 0.13μm RF-CMOS process, full-wave simulations of the structure are conducted in Ansoft's High Frequency Structure Simulator (HFSS) to extract the S-parameter model, which is exported to circuit simulation [4]. The spiral-inductor and the MOS varactor of NLTLs are based on IBM's foundry device models. The section number n is chosen to be 10, giving the maximum conversion efficiency for second harmonic, which will be shown later.

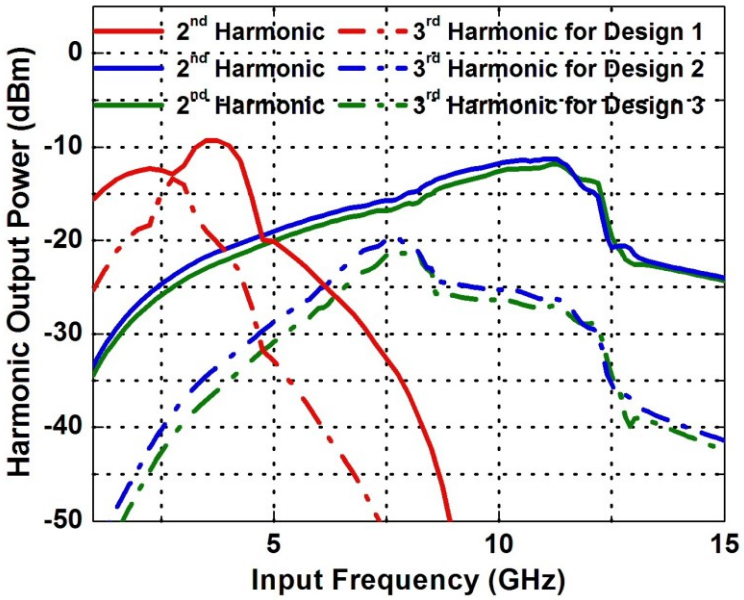

Figure 2-5 Simulated and calculated 2nd and 3rd harmonic output power of NLTLs excited by a 0 dBm sinusoidal signal.

	f_{in}	P_{2nd}
Single Diode 1	3.5 GHz	−16 dBm
NLTL Design 1	3.5 GHz	−9 dBm
Single Diode 2	11 GHz	−23 dBm
NLTL Design 2	11 GHz	−11 dBm

Table 2-2 Simulation results of single diode frequency doublers and corresponding NLTL designs.

The input ports of NLTLs are fed by a sinusoid $V_s = V_0 \sin(\omega t)$, whose input power is chosen to be 0 dBm, close to the practical RFID applications at the tag receiving antenna. Figure 2-5 shows the simulated output power of generated 2nd and 3rd harmonics of three NLTLs. It can be seen that the conversion efficiency for the m^{th}

harmonic (being 2 or 3) peaks slightly below f_{bragg}/m where the Bragg cutoff has filtered all the higher-order harmonics. In addition, Design 2 exhibits 1-2 dBm higher output harmonic power compared to Design 3, since Design 2 experiences less transmission line loss as well as larger nonlinearity of varactors. To further demonstrate the harmonic generation efficiency of the NLTL, we also simulate two single-diode frequency doublers in the same technology. One is designed for f_{in} = 3.5 GHz and compared with Design 1. The other one is for f_{in} = 11 GHz and compared with Design 2. For fair comparison, the capacitance values of single diodes are chosen to be the sum of all loaded varactors of the corresponding NLTLs, and the matching network loss of the single diodes is assumed negligible. The simulation results are shown in Table 2-2. For both designs, it can be found that the NLTL frequency doublers have at least 7 dBm higher harmonic power. Although the efficiency of single diode doublers may be further enhanced by using a larger diode, it would need larger inductance or longer transmission line for matching, which will occupy large circuit area and introduce further losses. For example, a first-order tunable impedance matching network in 'T' configuration at 1.95 GHz has at least 1.15 dB insertion loss. The shunt inductance used for matching is around 4.7 nH with Q = 55 [6].

To investigate the harmonic formation process along the NLTL stages, Figure 2-6 shows the harmonic output power of Design 1 at several section number n. For the 2nd and 3rd harmonic, the optimum n is around 10 and 5, respectively. The shorter length with maximum conversion efficiency for 3rd harmonic comes from larger attenuation loss and stronger dispersion. With lower input frequency, the optimum n should be larger according to (2.13).

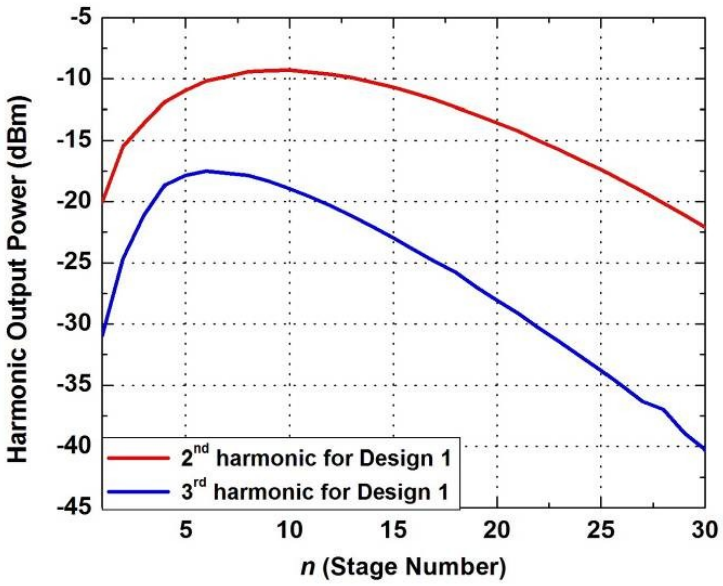

Figure 2-6 Simulated 2nd and 3rd harmonic output power of Design 1 versus the section number *n* with a 0 dBm and 3.5 GHz input sinusoidal signal.

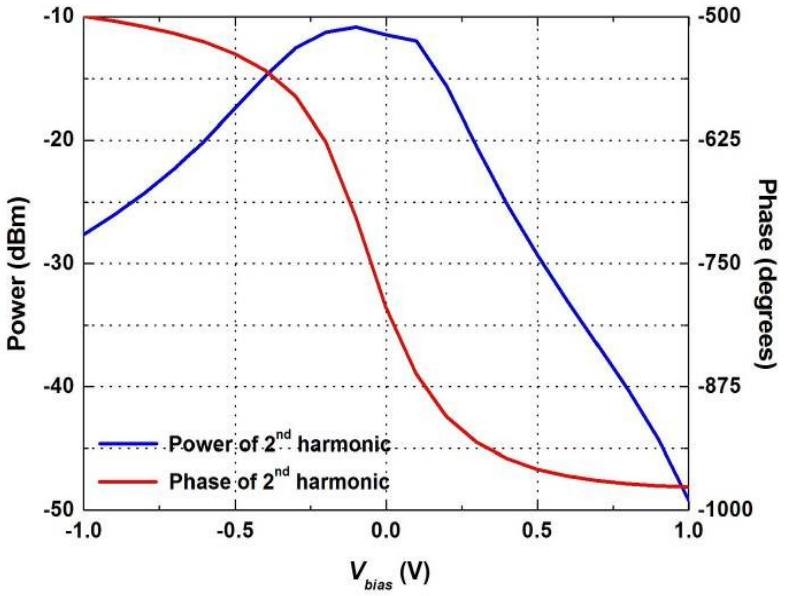

Figure 2-7 Simulated second harmonic output power and phase of Design 1 at different V_{bias} with the input frequency f_{in} = 3 GHz and the input power P_{in} = 0 dBm.

Figure 2-7 shows the simulated output power and phase of 2nd harmonic of Design 1 at various bias points. It can be found that the maximum conversion occurs around V_{bias} = 0. The second-harmonic power in the positive bias shows a sharper decrease than in the negative bias region. This is because the large capacitance at higher V_{bias} lowers down f_{bragg}, which introduces more Bragg reflection for the second harmonic signal. From Figure 2-7, one can also see the sharp phase change near V_{bias} = 0 V while the amplitude of the 2nd harmonic is almost constant. Specifically, almost 180° phase change can be achieved when V_{bias} is switched from –0.25 V to 0 V. The output power and phase of second harmonic dependence on the bias voltage can be used to modulate the local sensor data on the second harmonic signal with ASK or PSK. Other similar modulation schemes are also possible.

2.4.2. Harmonic generation measurements

We fabricated three NLTL designs in IBM 8RF 0.13μm CMOS process with parameters given in Table 2-1, as shown in Figure 2-8. The NLTLs are excited by a CW RF signal generated by Agilent E8257D. Spectrum analyzer Agilent 8564EC is used to measure the output power of the desired harmonics at each input frequency. To evaluate the loss in the fundamental wave, the transmission coefficients $|S_{21}|$ are measured. De-embedding is done by TRL calibration with Agilent E8364B.

Figure 2-9 shows the measured output power of the 2nd and 3rd harmonics as well as the fundamental loss of Design 1. The maximum 2nd harmonic output power is −10 dBm at an input frequency of 3.4 GHz, while the 3rd harmonic peaks at 2.6 GHz with output power of −15 dBm.

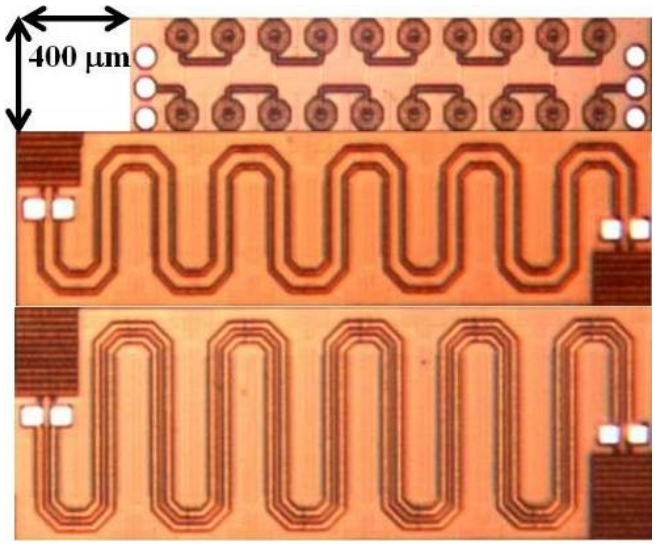

Figure 2-8 Scaled die photographs of three on-chip NLTLs: Design 1 with lumped inductor (top), Design 2 with CPS (middle), and Design 3 with CPS (bottom).

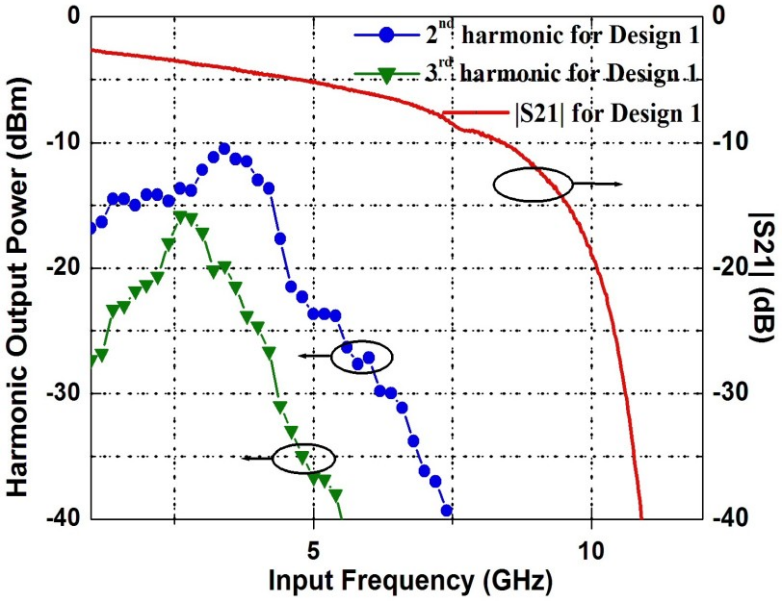

Figure 2-9 Measured 2nd and 3rd harmonic output power of Design 1 excited by 0 dBm sinusoidal signal.

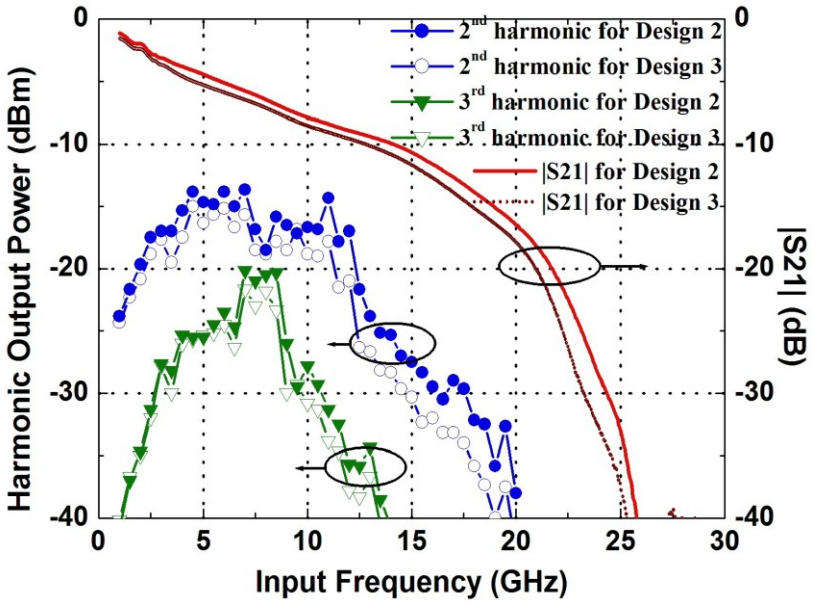

Figure 2-10 Measured 2nd and 3rd harmonic output power of Designs 2 and 3 excited by 0 dBm sinusoidal signals.

Figure 2-10 shows the measured output power of the 2nd and 3rd harmonics as well as the transmission characteristics of Designs 2 and 3. Compared to Figure 2-5, the measurements in Figure 2-10 follow the circuit simulation profile closely except the flattened peaks of harmonics, owing to the accuracy of the transmission line model and inclusion of other additional loss mechanisms such as the substrate effect. Consistent with simulation, Design 2 has slightly better conversion efficiency over Design 3 due to stronger nonlinearity of varactors. The maximum output power of the second harmonic for Designs 2 and 3 is −14 dBm and −15 dBm, respectively. For the third harmonic, both designs achieve around −21 dBm output power.

2.5 Conclusion

We present a novel radio frequency identification (RFID) transponder based on nonlinear transmission lines (NLTLs). The NLTL provides an effective solution to self-jamming with the harmonic generation property and is passive, compact as well as offering ready impedance matching. Analytical modeling is developed to facilitate the design procedures. Both simulation and measurements of the NLTL prototypes show the efficient harmonic generation under small input power. Three NLTLs are fabricated with different Bragg cutoff frequency f_{bragg} in IBM 8RF 0.13μm CMOS process. The 0.4 mm by 1.8 mm NLTL with f_{bragg} = 10 GHz shows −10 dBm 2nd harmonic and −15 dBm 3rd harmonic power by 0 dBm small signal input.

REFERENCES

[1] Reinmut K. Ho®mann, *Handbook of Microwave Integrated Circuits*, Artech House, Inc., 1987.

[2] K. S. Champlin and D. R. Singh, "Small-signal second harmonic generation by a nonlinear transmission line," *IEEE Trans. Microwave Theory and Tech.*, vol. 34, no. 3, pp. 351-353, Mar. 1986.

[3] K. G. Lyon, F. Yu, and E. C. Kan, "Space efficient CMOS nonlinear transmission lines," in *Proceedings of IEEE International* Symposium *on Circuits and Systems*, pp.2073-2076, May 2009.

[4] Cadence Design Systems, *http://www.cadence.com/products/rf.html*.

[5] M. G. Case, "Nonlinear transmission lines for picosecond pulse, impulse and millimeter-wave harmonic generation," *Ph.D.* dissertation, Univ. California at Santa Barbara, CA, 1993.

[6] P. Scheele, F. Goelden, A. Giere, S. Mueller and R. Jakoby, "Continuously tunable impedance matching network using ferroelectric varactors," in *IEEE MTT-S* International *Microwave Symposium Digest*, pp. 603–606, June 2005.

CHAPTER 3

REFLECTIVE NLTLS

In this chapter, we propose a novel harmonic RFID transponder based on the reflective NLTLs. By employing the single antenna configuration, the total footprint of the device can be reduced significantly without degradation in the harmonic conversion efficiency. The reflective NLTL can also achieve reasonable dual-band impedance matching without any additional matching network.

3.1 Motivation

In the harmonic RFID system, the tag generally consists of a receiving antenna, a nonlinear device that generates the harmonic or subharmonic backscatter signal, and a separate harmonic-transmitting antenna [5] – [10], due to the narrow-band nature of most antenna and matching network. One such example used a Schottky diode doubler to generate second harmonic [5]. Another approach used the injection-locked LC oscillator for harmonic generation [8], which however requires more than 1 mW power, not practical in the passive RFID transponder with an RF-to-DC converter. All the above configurations require the additional harmonic antenna as well as the matching network for second harmonic, in comparison with the conventional backscattering scheme. Since the antennas are often the largest components from aperture constraints, the additional harmonic-transmitting antenna would significantly increase the footprint of the sensor device.

Another proposal used harmonic re-radiation for insect tracking [11]. In this tag design, a single broadband dipole antenna served to both receive and transmit the

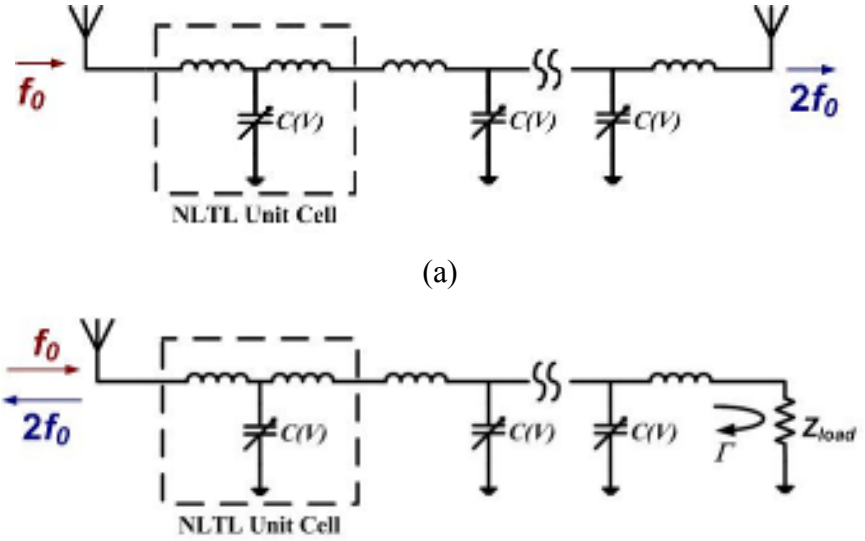

Figure 3-1. The circuit model of the matched and the reflective NLTLs with the antennas.

signal, while a Schottky diode was used to generate the second harmonic. However, additional area and lossy impedance matching network are invoked, which consists of a 1 mm-diameter inductive loop and a single discrete diode. In addition, the harmonic conversion efficiency decreases with the increasing interrogation power, which imposes a strong limit to the communication range of 100 m even though a 4kW reader power is used.

We present a harmonic RFID tag based on reflective nonlinear transmission lines (NLTLs). A unique feature of the transmission line is that termination can be used to reflect the travelling waves, and hence the harmonic signal can be radiated from the same receiving antenna. Only one dual-band/broadband antenna is needed for this harmonic tag if the antenna loss is sufficiently low for both the fundamental and harmonic frequencies. The reflective configuration can also halve the stage number in NLTL for the same power level of the output harmonic. In addition, NLTLs enable

tunable impedance to match both the fundamental and harmonic signals, which is not achievable in the single-diode configuration.

3.2 Harmonic Generation Model

Figure 3-1 shows the circuit models of the matched and the reflective NLTLs with antennas. Both input and output of the matched NLTL are connected to an individual antenna with impedance of 50 Ω. For the reflective NLTL, one end is matched, while the other end is terminated with the load impedance Z_{load}. By solving the differential equations [13], the voltage amplitude of the reflected second harmonic signal at the input port is:

$$V_{2nd}^{-}(0) = A_2\left[\Gamma_1^{\,2}\left(1-e^{(2\gamma_1-\gamma_2)N}\right)-\Gamma_2\left(1-e^{-(2\gamma_1-\gamma_2)N}\right)\right] \quad (3.1)$$

where $A_2 = q^{(2)}(V_{bias})\ \gamma_2 V_0^{\,2}/[4q^{(1)}(V_{bias})(2\gamma_1-\gamma_2)]$; $\gamma_1=\alpha_1+j\beta_1$; $\gamma_2=\alpha_2+j\beta_2$; , α_1 and α_2, β_1 *and* β_2 are the per-stage attenuation constants and phase constants of fundamental frequency and the second harmonic signals; N is the number of stages; V_0 is the amplitude of the fundamental wave at the input port; $q(V_{bias})$ is the charge on nonlinear capacitance as a function of the varactor bias voltage; $q^{(1)}(V_{bias})$ and $q^{(2)}(V_{bias})$ denote the first and second derivatives with respect to V_{bias}; Γ_1 *and* Γ_2 are the reflection coefficients for the fundamental and second harmonic signals. To achieve the complete reflection and avoid additional loss on the load impedance, $|\Gamma|$ is chosen to be 1, where the NLTL can be either open-ended or short-ended. For open-ended termination, Eq. (3.1) can be rewritten as:

$$V_{2nd\_open}^{-}(0) = A_2\left(e^{-(2\gamma_1-\gamma_2)N} - e^{(2\gamma_1-\gamma_2)N}\right) \tag{3.2}$$

Considering the lossless case for simplicity, where $\gamma_1 = j\beta_1$ and $\gamma_2 = j\beta_2$, (2) can be reduced to:

$$V_{2nd\_open}^{-}(0) = \left|2A_2 \sin\left[\left(2\beta_1 - \beta_2\right)N\right]\right| \tag{3.3}$$

Similarly, for short-ended termination, $\Gamma_1 = \Gamma_2 = -1$, and the reflected second harmonic is:

$$V_{2nd\_short}^{-}(0) = A_2\left(2 - e^{-(2\gamma_1-\gamma_2)N} - e^{(2\gamma_1-\gamma_2)N}\right) \tag{3.4}$$

which can be simplified in the lossless case as:

$$V_{2nd\_short}^{-}(0) = \left|4A_2 \sin^2\left[\left(2\beta_1 - \beta_2\right)N/2\right]\right| \tag{3.5}$$

From (3.3) and (3.5), we can find that the reflected 2nd harmonic amplitude of both open-ended and short-ended NLTLs is a periodic function of N and the period is determined by the dispersion characteristics, which is the same as the matched NLTL [9]. With the same input frequency and dispersion condition, the optimal number of sections to achieve the largest harmonic amplitude for the open-ended NLTL is $\pi/2/(2\beta_1-\beta_2)$, which is only half of the stage number of the matched NLTL. For the short-ended NLTL, although it needs the same section number of $\pi/(2\beta_1-\beta_2)$ as the matched one, the largest harmonic amplitude is almost doubled.

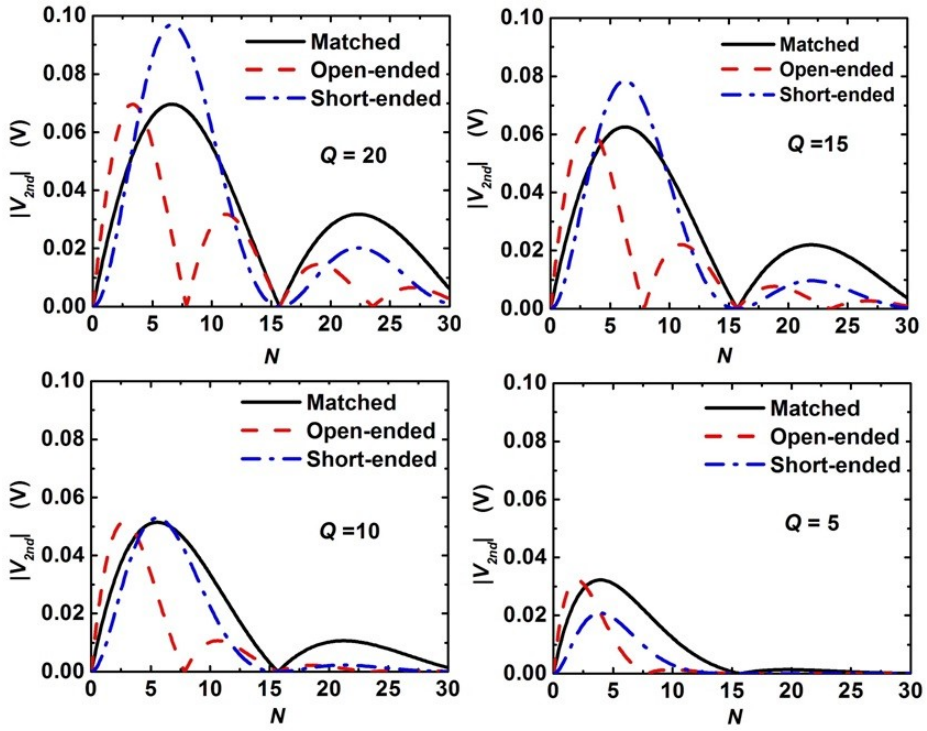

Figure 3-2. Calculated output second harmonic power versus stage number N for reflective and matched NLTLs with different quality factors and the same f_{in}.

Now considering the loss of the transmission line and varactor, the propagating harmonic wave would be a combined process of growing with N periodically and attenuating exponentially at the same time. According to (3.2) and (3.4), Figure 3-2 shows the calculated amplitude of second harmonic versus the stage number N with different magnitude of losses. The quality factor $Q = \beta / 2\alpha$ is used to define the losses of the NLTL. From Figure 3-2, it is evident that the optimal stage number of the open-ended NLTL is only half of the short-ended and matched ones. In addition, with the increasing loss (lower Q), the 2nd harmonic amplitude is attenuated faster along the length, leading to decreasing optimal stage number. When the NLTL has small transmission loss with $Q > 10$, the short-ended one achieves the largest maximum harmonic power. On the other hand, when the NLTL is lossy with $Q < 10$, the open-

ended line shows larger harmonic power than the short-ended line. Therefore, the open-ended or short-ended configuration should be chosen correspondingly based on different technology.

3.3 Impedance Matching

The remaining design challenge is how to simultaneously match impedance for both fundamental and second harmonic signals of the reflective NLTLs at the input port. As the input matching of short-ended NLTL is just quarter-wavelength shift from the open-ended one, we only need to analyze the open configuration here.

The input impedance looking into the open-ended NLTL is:

$$Z_{in} = Z_{NLTL} \frac{e^{(\alpha+j\beta)N} + e^{-(\alpha+j\beta)N}}{e^{(\alpha+j\beta)N} - e^{-(\alpha+j\beta)N}} \tag{3.6}$$

At the oscillation frequencies where $\beta = k\,\pi / N$ ($k = 0, 1, \ldots, N$), the imaginary of input impedance vanishes and the real part would be:

$$\begin{aligned} Z_{in} &= Z_{NLTL}\left(1 + \frac{2}{e^{2\alpha N} - 1}\right) = Z_{NLTL}\left(1 + \frac{2}{e^{\beta N/Q} - 1}\right) \\ &= Z_0\sqrt{\frac{1+\cos\beta}{2}}\left(1 + \frac{2}{e^{\beta N/Q} - 1}\right) \end{aligned} \tag{3.7}$$

where $\beta = \cos^{-1}(1-2\omega^2/\omega_{bragg}{}^2)$ and ω_{bragg} is the Bragg frequency of NLTL.

Figure 3-3 shows a simulated plot with real and imaginary parts of input impedance Z_{in} of a 9-stage open-ended NLTL with $f_{bragg} = \omega_{bragg}/2\pi = 10$ GHz. We can find that

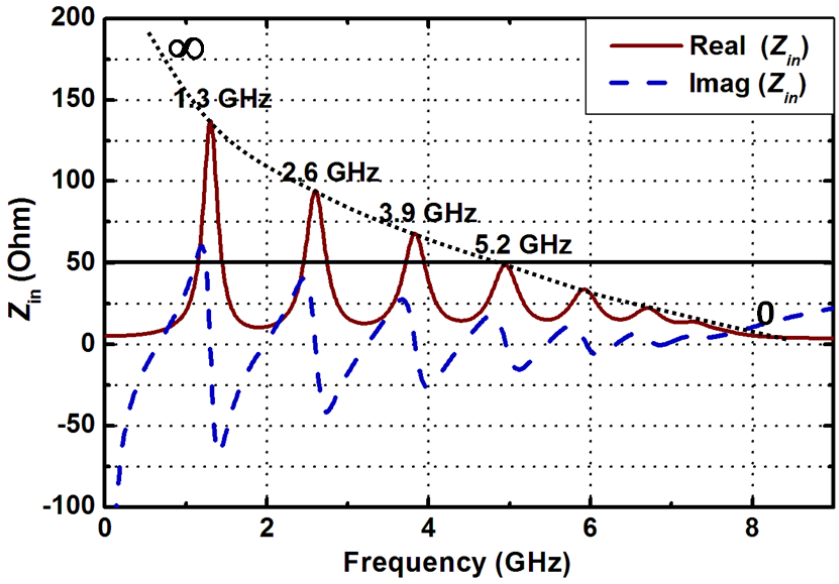

Figure 3-3 Simulated real and imaginary parts of input impedance of open-ended NLTL versus frequencies for N = 9 and Q = 8. The dotted line shows the lossless asymptote where Z_{in} approaches infinity.

Z_{in} becomes purely real near the oscillation frequency 1.3 GHz and its harmonics. From (3.7), when increasing the frequency from DC to the Bragg frequency ω_{bragg}, Z_{NLTL} would decrease from Z_0 to 0, while β increases from 0 to π. As a result, the real part of Z_{in} at oscillation frequencies would decrease from infinity to zero with increasing frequency. For a source impedance of 50 Ω, the open-ended NLTL would have a reasonable matching near the harmonics of 1.3 GHz without additional matching network.

To investigate the effects of the loss and the stage number on the matching condition, we change the quality factor and the length of the NLTL. According to (7), Figure 3-4 shows the calculated real part of input impedance of open-ended NLTL versus normalized frequency with different Q and N. In Figure 3-4 (a), with larger N, the decreasing rate of Z_{in} would be faster. The open-ended NLTL can be matched to

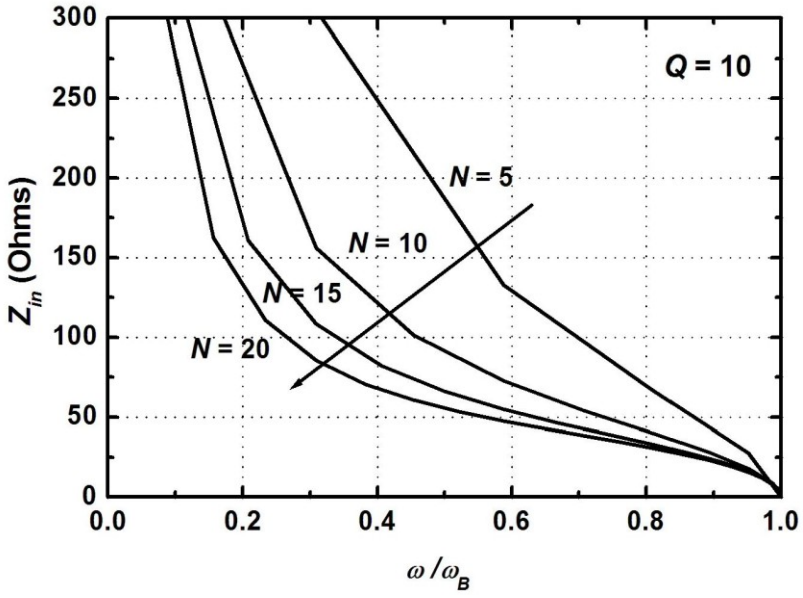

(a)

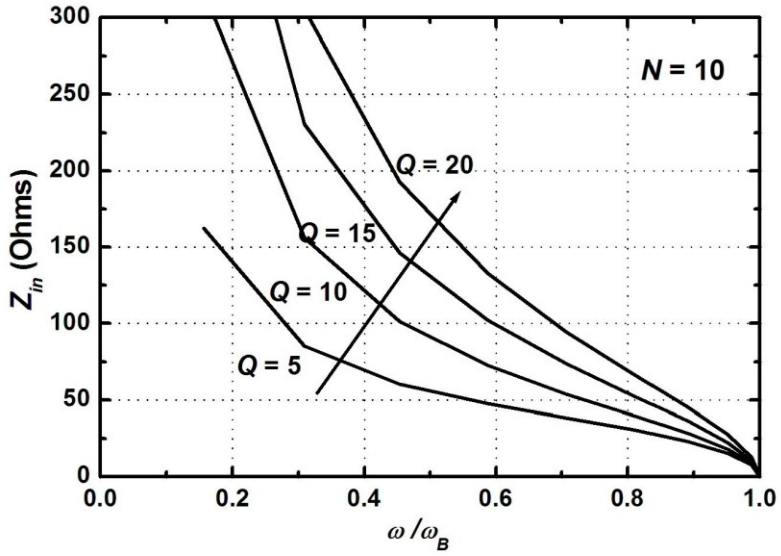

(b)

Figure 3-4 Calculated real part of Z_{in} of open-ended NLTL versus normalized frequencies (a) Effect of stage number N for $Q = 20$ (b) Effect of quality factor Q for $N = 20$.

50 Ohms at lower frequencies. Similar to the stage number, with more losses (smaller Q), it is easier for the NLTL to achieve 50 Ohms impedance matching before getting strong Bragg reflection losses, as shown in Figure 3-4 (b). Generally, large stage number can be utilized to improve the impedance matching. If the loss is significant with $Q < 10$, small stage number is already feasible to achieve impedance matching.

3.4 Simulation Results

To demonstrate the harmonic efficiency of reflective NLTLs, we designed and simulated two 5-stage open, short NLTLs and one 10-stage matched NLTL with f_{bragg} = 10 GHz. The spiral-inductor and MOS varactor of NLTLs are based on IBM's 0.13μm 8RF device models.

To estimate the transmission line loss, we first simulated the quality factor of the NLTL, which can be calculated by $Q = \beta / 2\alpha$. The phase and attenuation constant per-section is extracted from S parameter simulation. As shown in Figure 3-5, the peak Q is around 10 in the middle of the 1 – 9 GHz frequency band. According to Figure 3-2, the open-ended and short-ended NLTLs would achieve similar maximum harmonic generation efficiency when Q is 10.

The input ports of NLTLs are fed by a sinusoid $V_s = V_0 \sin(\omega t)$, whose input power is chosen to be 0 dBm. Figure 3-6 shows the simulated power of generated 2nd harmonics of three NLTLs in Cadence. Both open-ended and short-ended NLTLs only need half of the stage number of the matched NLTL to achieve the same maximum harmonic power. However, for open-ended NLTL, the maximum harmonic conversion efficiency occurs around the input frequency of 2.6 - 3 GHz compared to the optimal input frequency of 3.8 GHz for the short-ended one. With different reflective loads,

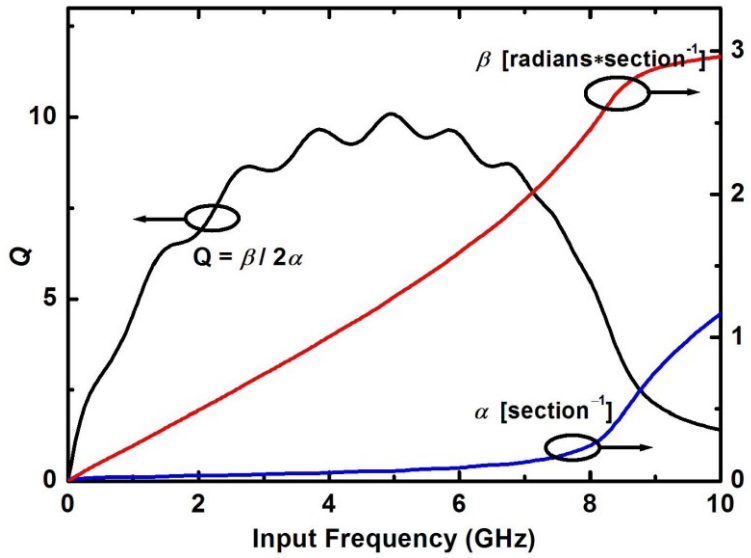

Figure 3-5 Simulated quality factor and per-section phase constant, attenuation constant of the NLTL.

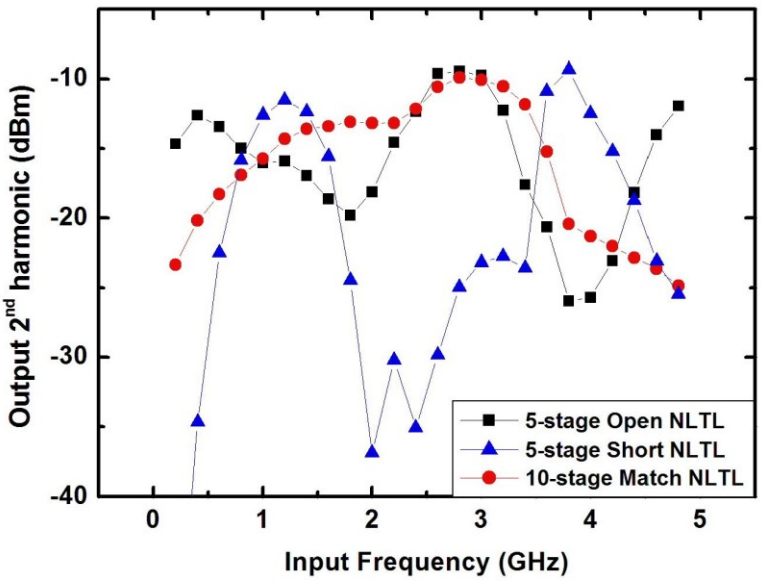

Figure 3-6 Simulated 2nd harmonic output power of NLTLs excited by a 0 dBm sinusoidal signal.

the optimal input frequency can be roughly estimated from Eqs. (3.3) and (3.5): f_{in} should be the frequency where $|2\beta_1 - \beta_2| = \pi/2N$ for open-ended NLTL and $|2\beta_1 - \beta_2| = \pi/N$ for short-ended one. Due to the stronger dispersion near f_{bragg}, the short-ended NLTL has higher optimal input frequency compared to the open-ended and matched NLTLs.

Figure 3-7 shows the input matching performance of the reflective NLTLs. We can find S_{11} oscillates near 2.5 GHz and its harmonics for the open-ended NLTL. The input matching of short-ended NLTL is approximately quarter-wavelength shift from the open-ended one. According to Eq. (3.6), the oscillation frequency can be estimated by:

$$f_{osc} = \frac{k\, f_{bragg}}{N} \left(k = 1, \ldots, N-1\right) \tag{3.8}$$

For a source impedance of 50 Ω, the open-ended NLTL shows a good matching performance of $S_{11} < -10$ dB near the frequencies 5 GHz and 6.8 GHz from Figure 3-7. The input matching performance would not only affect how much fundamental signal can be injected into the NLTL, but also the efficiency of delivering the 2nd harmonic power into the antenna. The former effect directly impacts the conversion efficiency of harmonic generation. This explains the oscillating behavior of the harmonic power versus input frequency of the reflective NLTLs compared to the matched one. Because the best input matching point does not always overlap with the optimal input frequency defined by the dispersion condition, the input frequency for highest harmonic power generation may differ from that defined by Eqs. (3.3) and (3.5).

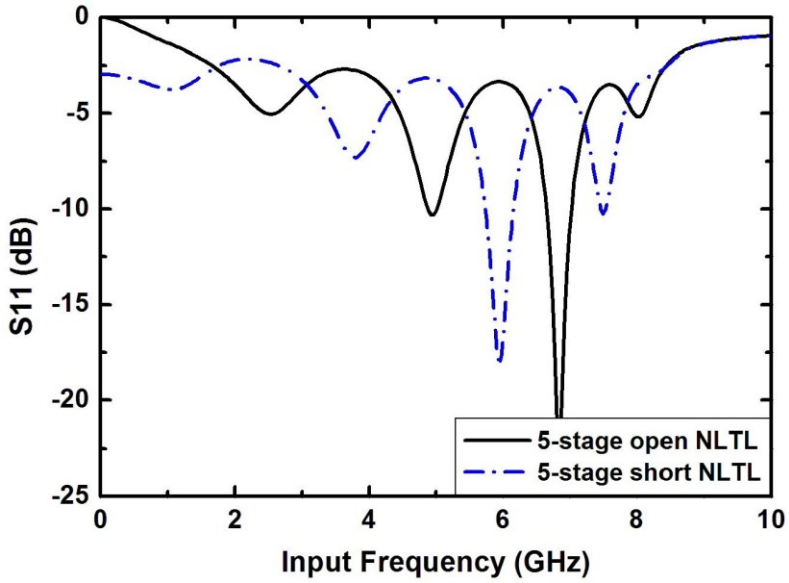

Figure 3-7 Simulated input matching by S_{11} for 5-stage open-ended and short-ended NLTLs.

Therefore, numerical simulations are required for accurate prediction of the optimal input frequency considering both the dispersion and matching conditions. From Figure 3-7, when the output second harmonic is 5.2 GHz giving −10 dBm maximum harmonic power, the open-ended NLTL provides input matching of S_{11} around −10 dB. Similarly, the short-ended NLTL achieves reasonable matching for the maximum harmonic power at 7.6 GHz without any additional matching network.

In our design, we set *N* to be five also for a small footprint consideration. We can already achieve maximum harmonic power and reasonable matching with five sections. Figure 3-8 shows the output 2nd harmonic power versus input frequency for the open-ended NLTL with different stage numbers. It can be found that the maximum harmonic power is reduced from −8 dBm to −15 dBm when the stage number is increased from 5 to 15. This is because the fundamental and second harmonic signals do not always propagate in phase together and interfere constructively. With

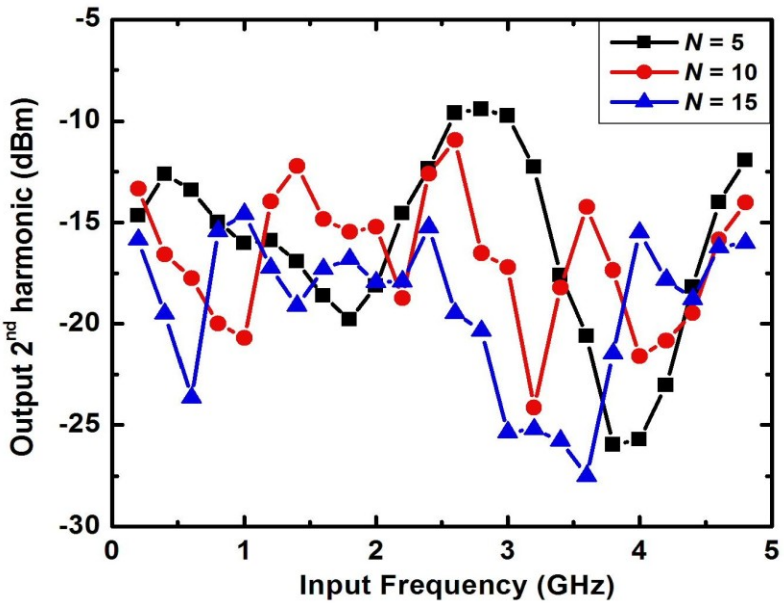

Figure 3-8 Simulated output 2nd harmonic power versus input frequency for the open-ended NLTLs with different stage number. (P_{in} = 0 dBm)

increasing N, the harmonic signal would first grow linearly, saturate to a certain value and then drop due to out of phase interaction. Considering extra attenuation, the whole process happens earlier with less N, as shown in Figure 3-4. As we mentioned previously, the optimal input frequency for the open-ended NLTL can be roughly estimated with Eq. (3.3): f_{in} should be the frequency where $|2\beta_1 - \beta_2| = \pi/2N$. Thus, larger N requires a weaker dispersion on the input frequency, which leads to lower optimal input frequency.

To explore how the input matching changes with stage number, Figure 3-9 shows the simulated S_{11} of the open-ended NLTL with different N. We can find that there are more oscillations in S_{11} with larger N. The number and location of the oscillations can be roughly estimated by Eq. (3.8). In addition, the longer NLTL achieves better matching within a broader bandwidth, which is also shown in Figure 3-4 (a). Especially, the best matching point is shifted toward the lower frequency with

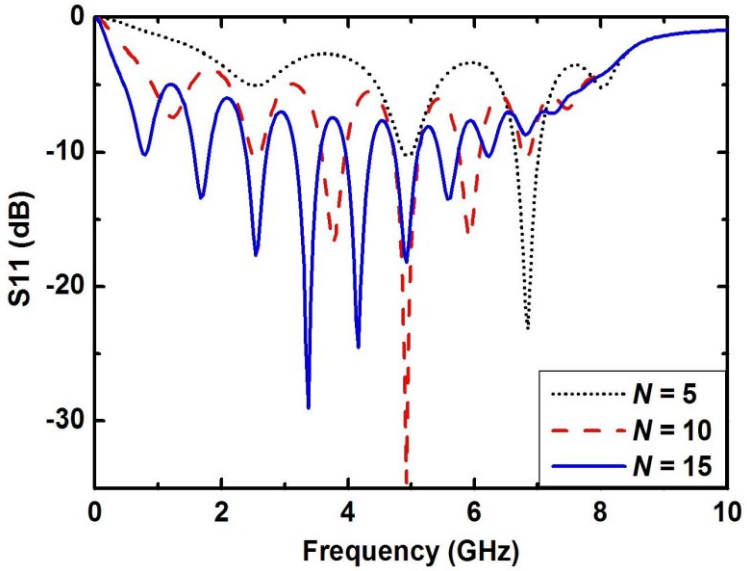

Figure 3-9 Simulated input matching for the open-ended NLTLs with different stage number.

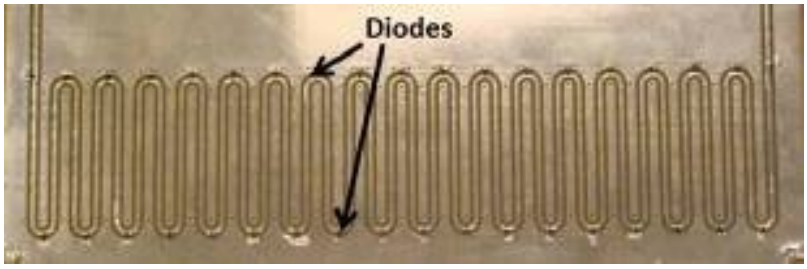

Figure 3-10 The microwave PCB holds the 37-stage CPW-based NLTL.

increasing *N*. Given the operation frequency band, we can always achieve good matching by selecting the stage number without any additional matching network. However, the stage number may not be the optimal value for the harmonic generation. Therefore, a tradeoff needs to be made in designing the section number for the reflective NLTLs to achieve both efficient harmonic generation and reasonable impedance matching.

3.5 Measurements and Discussion

To verify the concept of reflective NLTLs, we first start the design with f_{bragg} = 1 GHz on FR-4 laminate (high Q) and then implement on-chip NLTLs with f_{bragg} = 10 GHz and 15 GHz (low Q) in the IBM 0.13 μm CMOS process.

3.5.1. CPW-based NLTL on PCB

Our first implementation uses conductor-backed coplanar waveguides (CPW) transmission lines which are periodically loaded by reverse biased diodes on FR-4 laminate. In the long wavelength regime, a transmission line can be modeled as an inductance, $L \approx \tau Z_{TL}$, where τ is the delay time and Z_{TL} is the transmission line impedance. To save the design area, a serpentine structure is used. Figure 3-10 shows the PCB board with the folded CPW-based NLTLs. The parameters of CPW and loaded diodes are carefully chosen for f_{bragg} = 1 GHz according to [9].

To investigate the transmission loss, we first measured the quality factor Q of the NLTL versus frequency. As shown in Figure 3-11, Q is not constant over the whole frequency band. The peak Q is around 50, which fell in the middle of f_{bragg}. According to Figure 3-4, larger stage number should be chosen with small transmission loss for both impedance matching and harmonic generation. We picked 37-stage for the reflective NLTLs.

We configured the NLTLs of different reflective loads with open and short load connectors. Figure 3-12 shows the measured output 2nd harmonic power versus input frequency for matched, open and short NLTLs with 0 dBm input power generated by Agilent E8257D. Among three configurations, the short-ended NLTL exhibits the largest harmonic output power, which is around 6 dB larger than the matched and the open ones. This result matches well with the theoretical prediction. When the

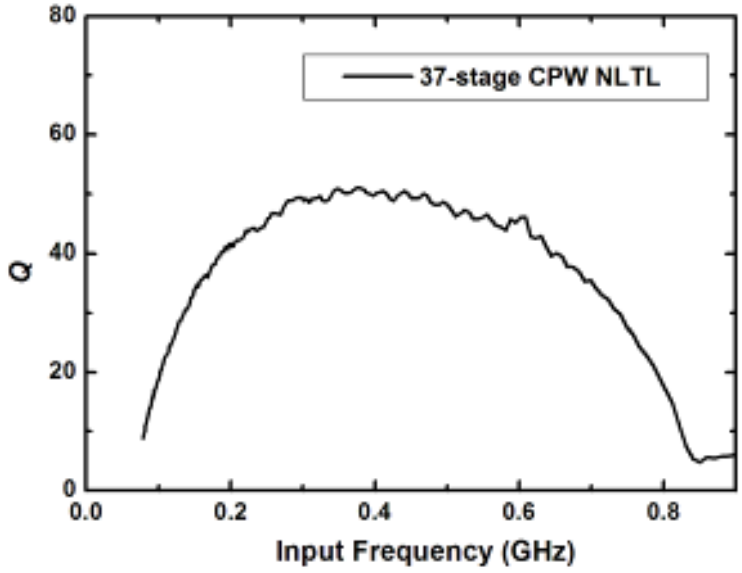

Figure 3-11 Measured quality factor of 37-stage CPW NLTL on FR-4 laminate.

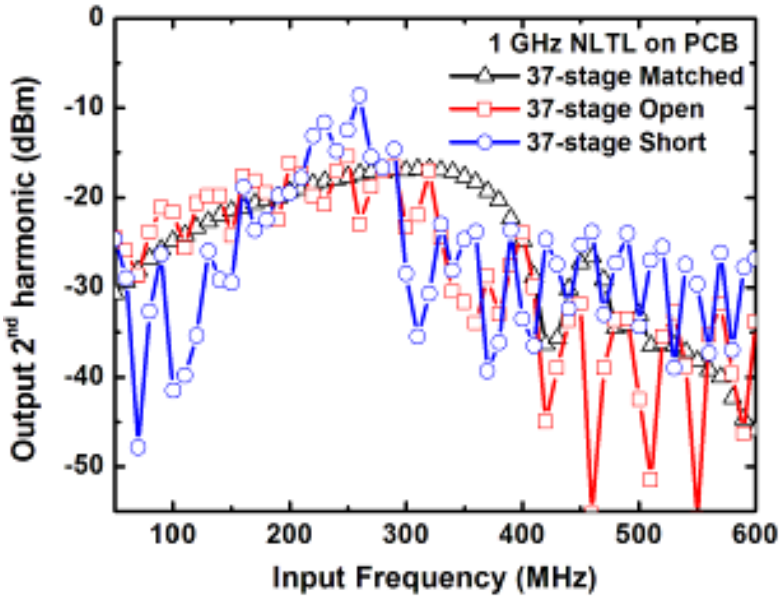

Figure 3-12 Measured output 2nd harmonic power of 37-stage NLTL with matched, open and short loads.

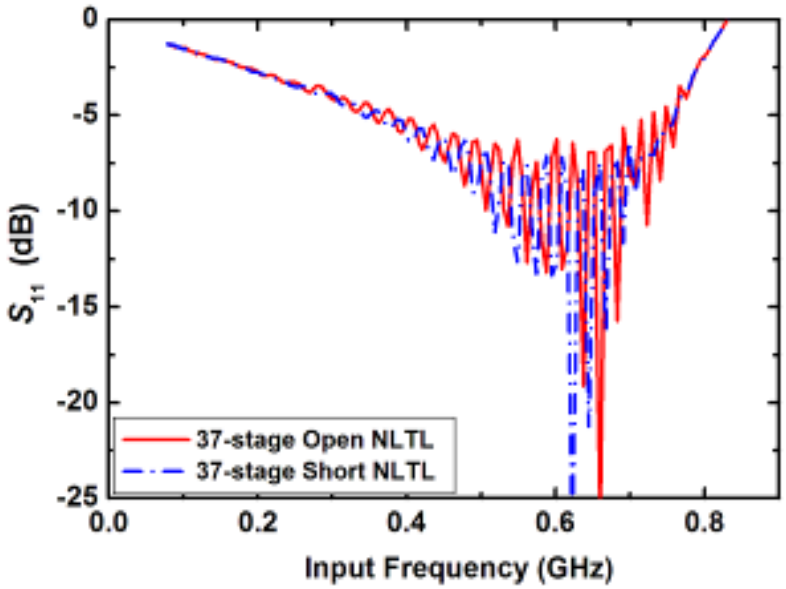

Figure 3-13 Measured input matching for open-ended and short-ended NLTLs.

transmission loss is small (Q > 10), the maximum 2nd harmonic of the short-ended NLTL would be larger than the other two configurations. Ideally, the maximum difference can be 6 dB according to Eqs. (3.3) and (3.5). By comparing the open-ended and matched NLTLs, we can find the open one has a little bit larger harmonic amplitude than the matched one. Intuitively, this is because the open one would provide additional 37-stage NLTLs to generate harmonic by reflecting back both of the fundamental and harmonic signals. However, this increase would be limited by the dispersion and loss effects. In addition, the optimal input frequency to achieve maximum harmonic generation for open-ended and short-ended NLTLs is near 250 MHz, which corresponds to the output 2nd harmonic frequency at 500 MHz. From Figure 3-11, we can find that both of the frequencies are located near the peak-Q.

Next, S_{11} is measured for both of the open-ended and short-ended NLTLs with Agilent E8364B. As shown in Figure 3-13, the two reflective NLTLs have a reasonable matching performance of $S_{11} < -10$ dB over 0.5 – 0.7 GHz. However, this

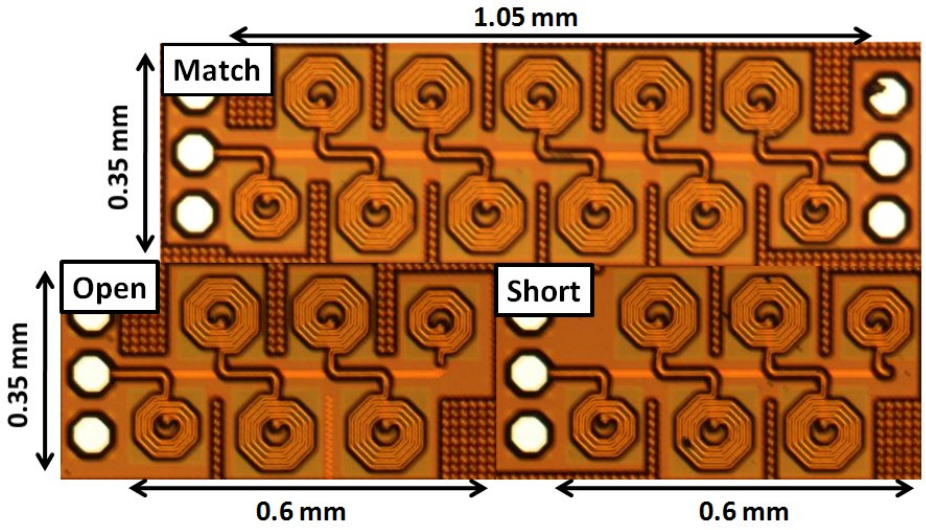

Figure 3-14 Die photo of the 10-stage matched, 5-stage open-ended and 5-stage short-ended NLTLs (f_{bragg} = 10 GHz).

frequency band is not the optimal range for harmonic generation according to Figure 3-11 and Figure 3-12. To match the frequencies for efficient harmonic generation, more stages can be added to lower the frequency band for impedance matching.

3.5.2. On-Chip reflective NLTLs

Then we implement on-chip NLTLs with f_{bragg} = 10 GHz and 15 GHz. We fabricated 5-stage open-ended and short-ended NLTLs in IBM 8RF 0.13μm CMOS process. For comparison, the 10-stage matched NLTLs are also implemented. Figure 3-14 shows the die photograph. The core areas are around 0.6 mm × 0.35 mm for reflective NLTLs and 1.05 mm× 0.35 mm for matched NLTL, not including the RF GSG (ground-signal-ground) pads. In all the designs, we use ground-shielded spiral inductors with peak Q around 17 at 10 GHz and 15 GHz, respectively. Accumulation-mode nMOS varactors are used with minimum-to-maximum capacitance ratio around

Design Frequency [GHz]	Inductance [nH]	Minimum Capacitance [fF]
10	1.39 (peak Q = 17)	530 (C_{max}/C_{min} = 3)
15	0.77 (peak Q = 18)	300 (C_{max}/C_{min} = 3)

Table 3-1 Inductor and capacitor values for NLTLs. The minimum capacitance values are taken at a bias of –0.5 V.

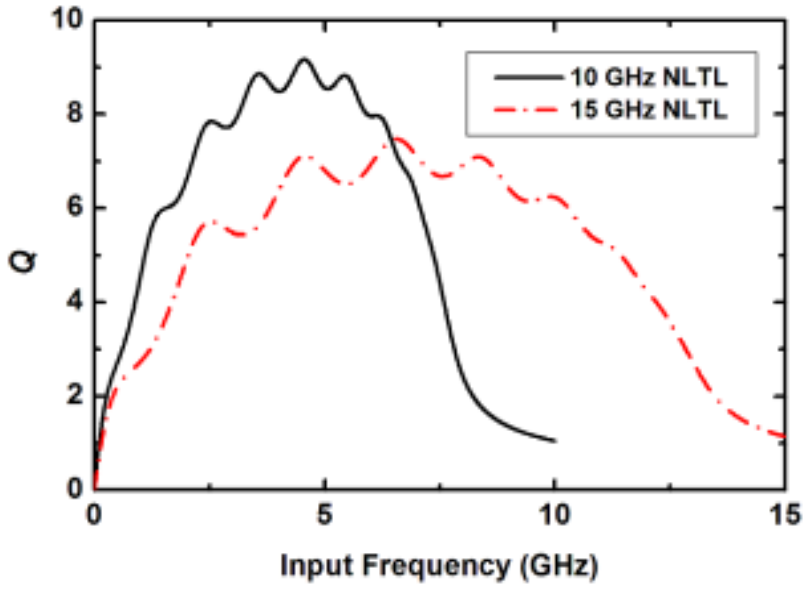

Figure 3-15 Measured quality factor Q for 10 GHz and 15 GHz NLTLs.

3.5. The inductor and capacitor values are shown in Table 3-1.

To evaluate the transmission line loss, we first measure the transmission coefficients S_{21} to extract the phase and attenuation constant β and α. De-embedding is

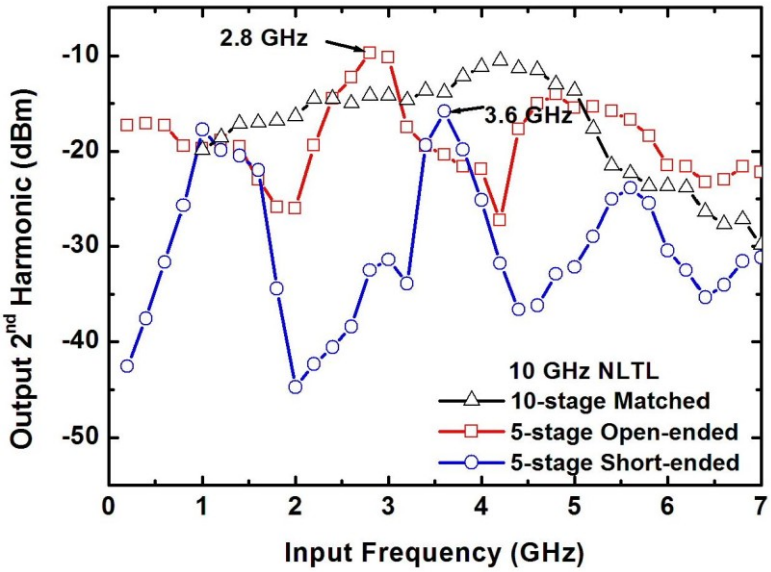

Figure 3-16 Measured output second harmonic power of the 10 GHz 10-stage matched, and 5-stage open-ended and short-ended NLTL with 0 dBm sinusoidal input signal (P_{in} = 0 dBm).

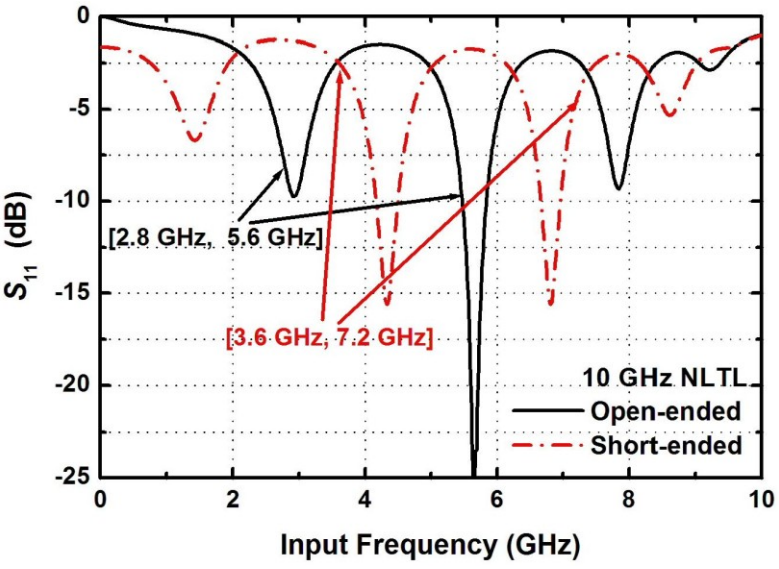

Figure 3-17 Measured input matching by S_{11} for 10 GHz open-ended and short-ended NLTLs (P_{in} = −17 dBm).

done by TRL (Through-Reflect-Line) calibration with Agilent E8364B. The quality factor Q ($Q = \beta/2\alpha$) for 10 GHz and 15 GHz NLTLs are shown in Figure 3-15. Due to significant substrate losses, Q of the on-chip NLTLs is below 10. The peak Q is around 9 for the 10 GHz NLTL and 7 for the 15 GHz NLTL. According to Section II, the open-ended configuration is preferred in the lossy environment when $Q < 10$.

Figure 3-16 shows the reflected second harmonic power measured against the input frequency. The directional coupler Marki C20-0R612 is used to measure the reflected signals. The NLTLs are excited by a 0 dBm CW RF signal generated by Agilent E8257D. From Figure 3-16, we can find that the open-ended NLTL achieves the same maximum harmonic power around −10 dBm as the matched one, while only half of the stages are needed. Comparing the open-ended and the short-ended ones, the open configuration exhibits larger conversion efficiency with Q of NLTL lower than 10, consistent with the calculation in Figure 3-2. The optimal input frequencies for the 10 GHz open-ended and short-ended NLTLs are around 2.8 GHz and 3.6 GHz, respectively.

To investigate the input matching, S_{11} is measured using Agilent E8364B. De-embedding is done by TRL calibration. As shown in Figure 3-17, the open-ended NLTL has a good matching performance of $S_{11} < -10$ dB at the optimal input frequency 2.8 GHz and second harmonic 5.6 GHz. For the short-ended one, there is more reflection for the second harmonic 7.2 GHz since it is close to the Bragg frequency. In addition, worse matching for the input frequency 3.6 GHz is also another reason of the short- ended NLTL showing 6 dB less maximum harmonic power than the open-ended configuration.

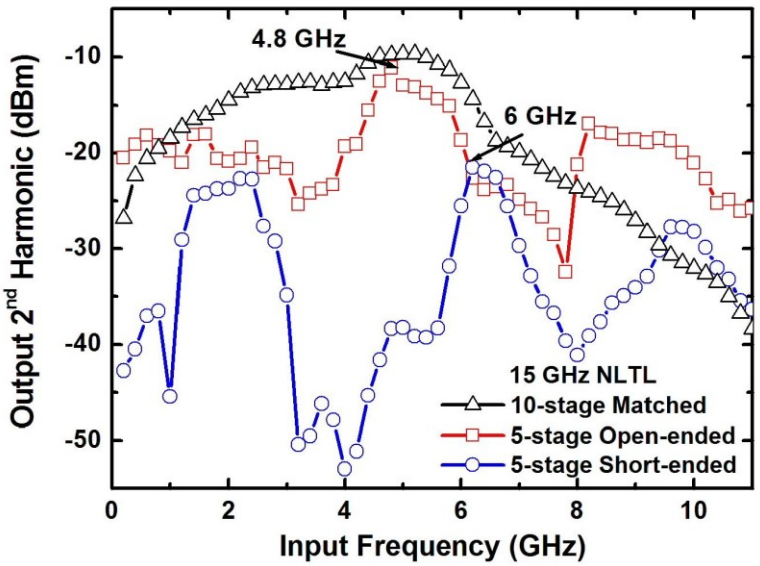

Figure 3-18 Measured reflected second harmonic power of the 15 GHz 10-stage matched, 5-stage open-ended and short-ended NLTLs with 0 dBm sinusoidal signal (P_{in} = 0 dBm).

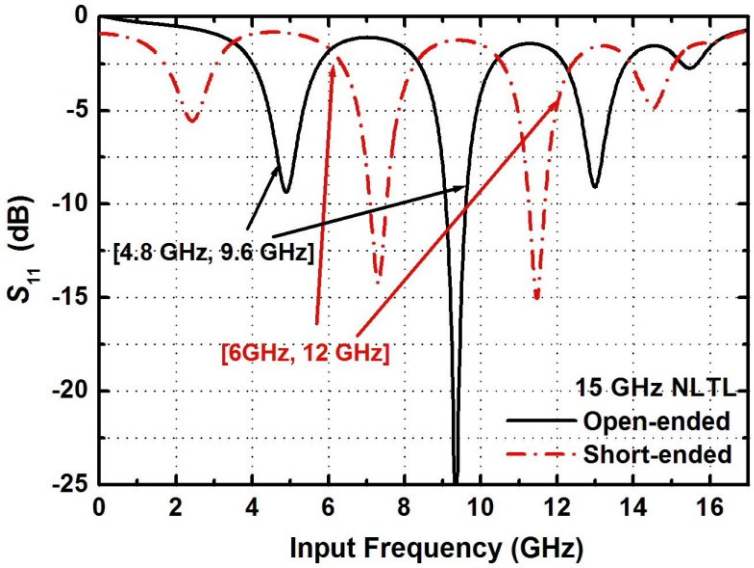

Figure 3-19 Measured input matching by S_{11} for 15 GHz open-ended and short-ended NLTLs (P_{in} = –17 dBm).

Similarly, we measured the second harmonic power of the 15 GHz NLTLs, shown in Figure 3-18. The open-ended one only needs half of the stage number of the matched NLTL to achieve almost similar maximum harmonic power of −10 dBm. The short-ended one shows more attenuation of the maximum harmonic compared to the 10 GHz NLTL due to smaller Q in high frequency and worse input matching condition. S_{11} performance is also measured by TRL calibration in Figure 3-19. The open-ended NLTL has good matching for both of the optimal input and output frequencies while the short-ended one experiences larger reflection for the second harmonic.

3.6 Conclusion

We present a harmonic radio frequency identification (RFID) transponder based on reflective nonlinear transmission lines (NLTLs). By employing the single antenna configuration, the total footprint of the device can be reduced significantly without degradation in the harmonic conversion efficiency. For the feasibility and design procedure, both open-ended and short-ended reflective NLTLs are implemented in IBM 0.13μm CMOS process. The 0.35 mm by 0.6 mm open-ended NLTLs show around −10 dBm reflected second harmonic by 0 dBm RF input. In addition, the reflective NLTL can also achieve reasonable dual-band impedance matching without any additional matching network.

REFERENCES

[1] M. Bouthinon, J. Gavan, and F. Zadwomy, "Passive microwave transponder, frequency doubler for detecting avalanche victims," in *Proc. 10th European Microwave Conf.*, Sept. 1980, pp, 579-583.

[2] K. Finkenzeller*, RFID Handbook*, *2nd Ed*. New York: Wiley, 2003.

[3] J. P. Curty, N. Joehl, C. Dehollain, and M. J. Declercq, "Remotely powered addressable UHF RFID integrated system," *IEEE J. Solid-State Circuits*, vol. 40, no. 11, pp. 2193-2202, Nov. 2005.

[4] U. Karthaus and M. Fischer, "Fully integrated passive UHF RFID transponder IC with 16.7-μW minimum RF input power," *IEEE J. Solid-State Circuits*, vol. 38, no. 10, pp. 1602-1608, Oct. 2003.

[5] S. M. Aguilar and T. M. Weller, "Tunable harmonic re-radiator for sensing applications," in *IEEE MTT-S International Microwave Symposium Digest*, pp. 1565–1568, June 2009.

[6] F. Alimenti, V. Palazzari, G. Orecchini, G. Pinca, P. Mezzanotte, M. M. Tentzeris and L. Roselli, "Crossed dipole frequency doubling RFID TAG based on paper substrate and ink-jet printing technology," in *IEEE MTT-S International Microwave Symposium Digest*, pp. 840–842, May 2010.

[7] C. W. Pobanz and T. Itoh, "A microwave noncontact identification transponder using subharmonic interrogation," *IEEE Trans. Microwave Theory and Tech.*, vol. 43, no. 7, pp. 1673-1679, July 1995.

[8] F. Kocer and M. P. Flynn, "A new transponder architecture with on-chip ADC for long-range telemetry applications," *IEEE J.Solid-State Circuits*, vol. 41, no. 5, pp. 1142–1148, May 2006.

[9] F. Yu, K. G. Lyon and E. C. Kan, "Harmonic generation from integrated nonlinear transmission lines for RFID applications," in *IEEE MTT-S International Microwave Symposium Digest*, pp. 844–847, May 2010.

[10] F. Yu, K. G. Lyon and E. C. Kan, "A novel passive RFID transponder using harmonic generation of nonlinear transmission lines," *IEEE Trans. Microwave Theory and Tech*., vol. 58, no. 12, pp. 4121-4127, Dec. 2010.

[11] B. G. Colpitts and G. Boiteau, "Harmonic radar transceiver design: miniature tags for insect tracking," in *IEEE Trans. Antennas and propagation*, vol. 52, no. 11, pp. 2825 - 2832, Nov. 2004.

[12] K. G. Lyon and E. C. Kan, "Microwave pulse generation using the Bragg cutoff of a nonlinear transmission line," in *IEEE MTT-S International Microwave Symposium Digest*, Jun. 2008, pp. 1461–1464.

[13] K. S. Champlin and D. R. Singh, "Small-signal second harmonic generation by a nonlinear transmission line," *IEEE Trans. Microwave Theory and Tech*., vol. 34, no. 3, pp. 351-353, Mar. 1986.

CHAPTER 4

WIRELESS LINK

The purpose of this chapter is to characterize the interrogation distance and simple magnitude and phase modulation abilities of NLTL based RFID tag. Detailed designs of digital and analog modulation schemes will be discussed in Chaps. 5 and 6.

4.1 Link Budget Calculation

4.1.1. Conversion gain of NLTLs

In practical RFID applications, the received interrogating signal varies with distances. To explore the communication range for NLTLs-based RFID system, it is important to evaluate the harmonic generation ability of an NLTL as a function of input power. Conversion gain G_m for m-th harmonic is defined as:

$$G_m = 10\log(\frac{P_m}{P_{in}}) \tag{4.1}$$

where P_{in} is the input power of the fundamental wave and P_m is the output power of m-th harmonic. Figure 4-1 plots the conversion gain of the 2nd and 3rd harmonics of matched NLTLs (Designs 1 and 2 of Fig. 2.5) versus the input power at the corresponding optimal input frequencies of 3.4 GHz and 5.8 GHz. We can see that the conversion gain decreases with smaller input power and the 3rd harmonics exhibit larger slope than the 2nd harmonics, which matches well to the prediction of (2.1).

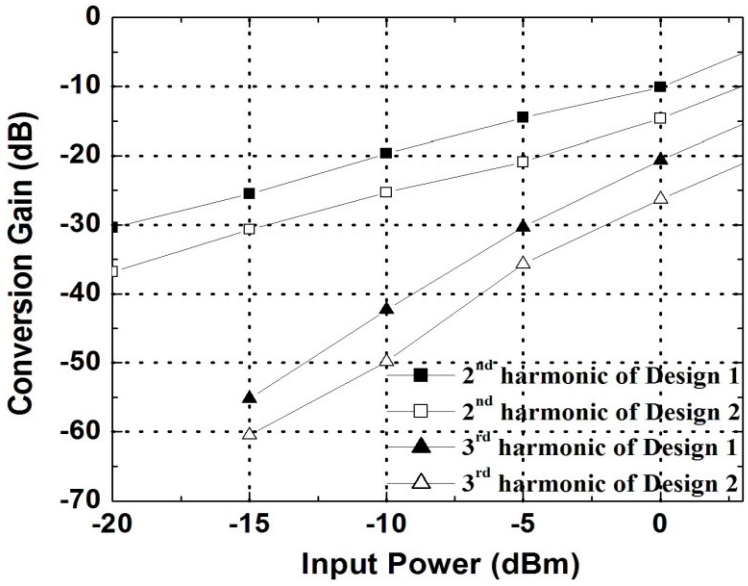

Figure 4-1 Measured conversion gain of matched NLTLs for the 2nd and 3rd harmonic power versus input power: Design 1 at 3.4 GHz; Design 2 at 5.8 GHz.

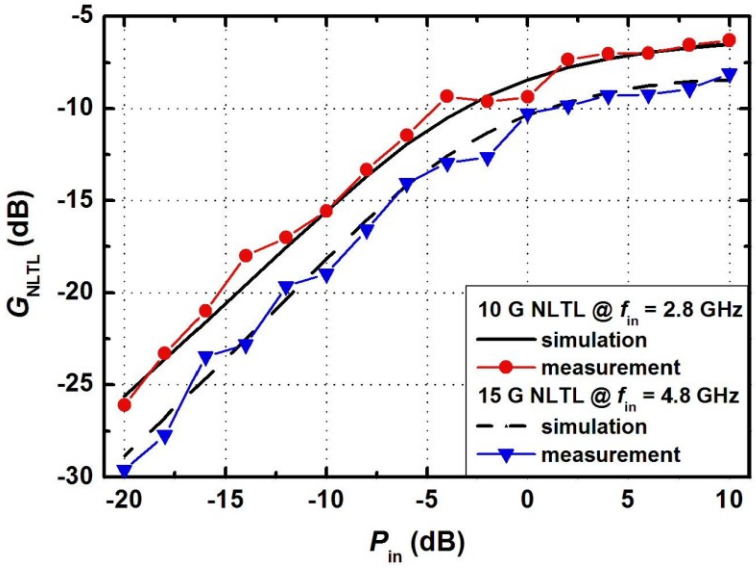

Figure 4-2 Simulated and measured output 2nd harmonic conversion gain versus input power for the 10 GHz and 15 GHz open-ended NLTLs.

Figure 4-2 plots both of the simulated and measured 2nd harmonic conversion gain of the open-ended 10 GHz and 15 GHz NLTLs versus the input power at the corresponding optimal input frequencies of 2.8 GHz and 4.8 GHz. We can see that the conversion gain grows almost linearly with the input power when $P_{in} < 0$ dBm. The saturation of conversion gain is due to the impedance mismatch at the input of the NLTL, as the NLTL's impedance varies significantly with large input signal.

For link calculations, we characterize the conversion gain of the NLTL according to Eq. (2.1), which can be expressed as:

$$G_{2nd} = \frac{P_{2nd}}{P_{in}} = \left(\frac{q^{(2)}(V_{bias})\gamma_2}{2q^{(1)}(V_{bias})(2\gamma_1 - \gamma_2)} \right)^2 V_{in}^{\ 2}$$
$$= K \frac{V_{in}^{\ 2}}{2R_{ant}} = K \cdot P_{in} \tag{4.2}$$

For a given transponder and operation frequency, all the parameters (q, γ, V_{bias}, R_{ant}) can be lumped into the constant K. As a result, the conversion gain of the NLTL varies with the power received from the interrogation beam.

4.1.2. Distance characterization

A typical NLTL based RFID link is shown in Figure 4-3. Compared to the reflective NLTL based RFID, the matched one has the similar wireless link setup except for the additional harmonic transmitting antenna. Assume the transmitting and receiving antennas of the reader and transponder have gains G_T and G_R, G_t and G_r, respectively. When the interrogation power from the reader is P_T, applying Friis transmission formula to the link, the received 2nd harmonic power would be:

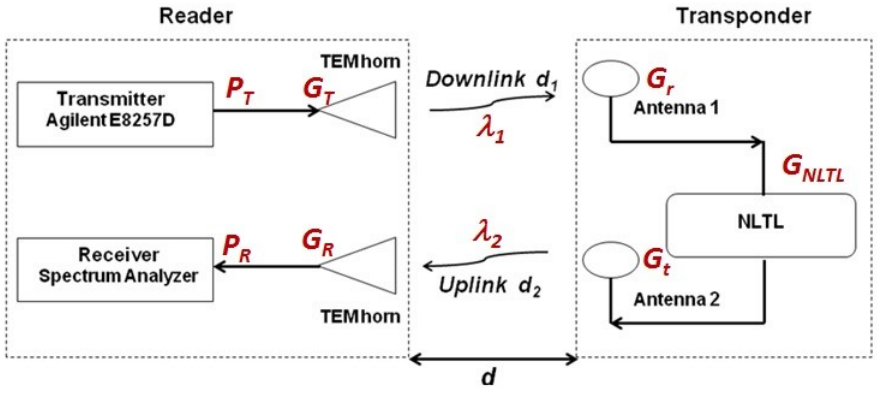

(a)

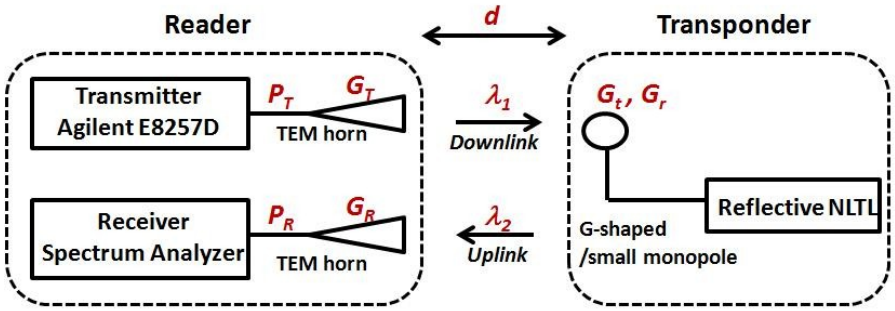

(b)

Figure 4-3 The reader-transponder radio link (a) the matched NLTL based RFID tag (b) the reflective NLTL based RFID tag.

$$P_R = \frac{\left(P_T G_T G_r\right)^2 G_t G_R K \lambda_1^4 \lambda_2^2}{\left(4\pi d\right)^6} \propto \frac{1}{d^6} \tag{4.3}$$

From Eq. (4.3), we can see that the transponder would have $1/d^6$ range behavior for the whole radio link.

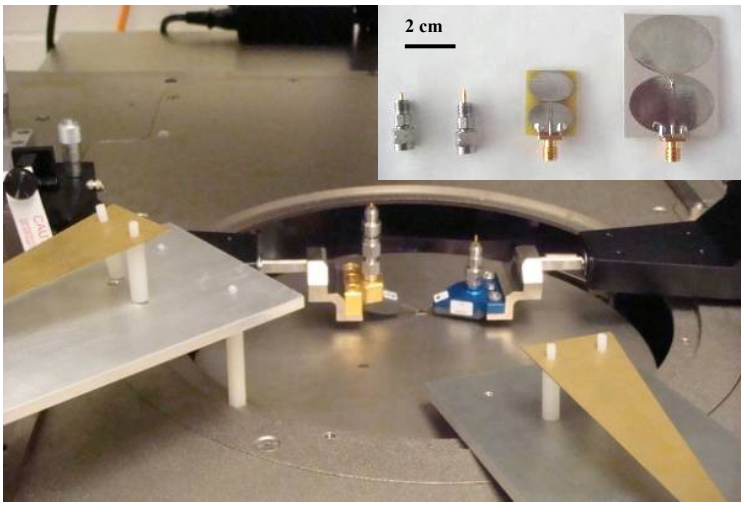

Figure 4-4 Photograph of the experiment setup showing D*dot antennas attached to the wafer probe by a coax adapter. Inset: antennas used for transponder testing (from the left to the right): D*dot 2, D*dot 1, Monopole 2 and Monopole 1.

4.2 Wireless Link Measurements

In order to characterize the interrogation distance of the matched NLTL based RFID tag, a test setup in Figure 4-3 (a) was implemented. The downlink distance d_1 is the distance between the transmitter of the reader and the transponder. The uplink distance d_2 is the distance between the receiver of the reader and the transponder. The transponder is under interrogation from the transmitter of the reader at a distance of 12 cm. The transmitted power from Agilent E8257D is 20 dBm, and a R&S®FSU spectrum analyzer is used as a receiver with –90 dBm sensitivity. NIST-standard TEM horn antennas are employed for transmitting and receiving signals on the reader side. For the transponder, we use two pairs of antennas: planar monopole antennas and D*dot probe antennas, where D*dot 1 and Monopole 1 are used for receiving the interrogating signal; D*dot 2 and Monopole 2 are used for transmitting the second

harmonic signal [1]–[2]. Figure 4-4 shows the photographs of the experiment setup and the antennas used in the test. The length of center conductor of D*dot 1 and D*dot 2 are approximately 7 mm and 4 mm, respectively. This setup is to demonstrate that the transponder system can still be operational with mm-scale D*dot antennas. Different antennas and configurations can be employed according to specific applications.

Using the network analyzer Agilent E8364B, the Friis transmission loss for the antenna setup can be characterized as:

$$\frac{P_r}{P_t} = G_t G_r \left(\frac{\lambda}{4\pi d} \right)^2 \tag{4.4}$$

The measured transmission loss is 32 dB at interrogating frequency of 3.5 GHz from the horn antenna to Monopole 1(downlink). From Monopole 2 to the reader horn antenna (uplink), the transmission loss is 30 dB at the second harmonic frequency of 7 GHz. For D*dot antennas, the transmission loss of the downlink is around 40 dB at 3.5 GHz and the uplink loss is 32 dB at 7 GHz.

To obtain the range characterisitic of the NLTL-based transponder, we measured the received harmonic power with different downlink distance d_1 from the transmitter to the tag, shown in Figure 4-5. The uplink distance d_2 from the tag to the reader is maintained as 12 cm. It can be found that the second harmonic signal received by the interrogator varies as $1/d_1^4$, independent of the antenna choices. This $1/d_1^4$ relation contrasts with the conventional $1/d_1^2$ characteristic from the transmitter to the transponder with the conventional backscattering scheme. This is mainly due to the additional second harmonic conversion dependence from the NLTL, which is also quadratic with the received input power. When increasing both of the downlink distance d_1 and the uplink distance d_2, since the uplink range has the characteristic of

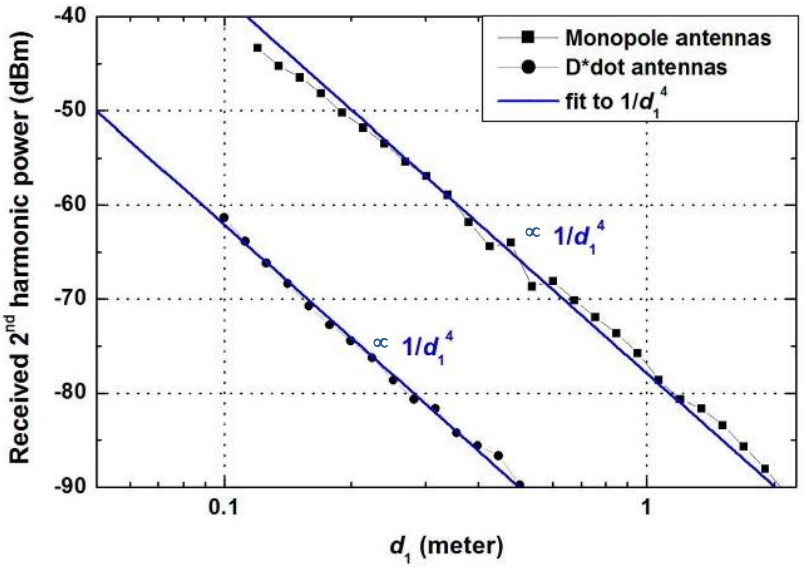

Figure 4-5. The measured second harmonic signal power received by the reader at operating frequency of 3.5 GHz with P_t = 20 dBm. The uplink distance d_2 from the tag to the reader is maintained as 12 cm.

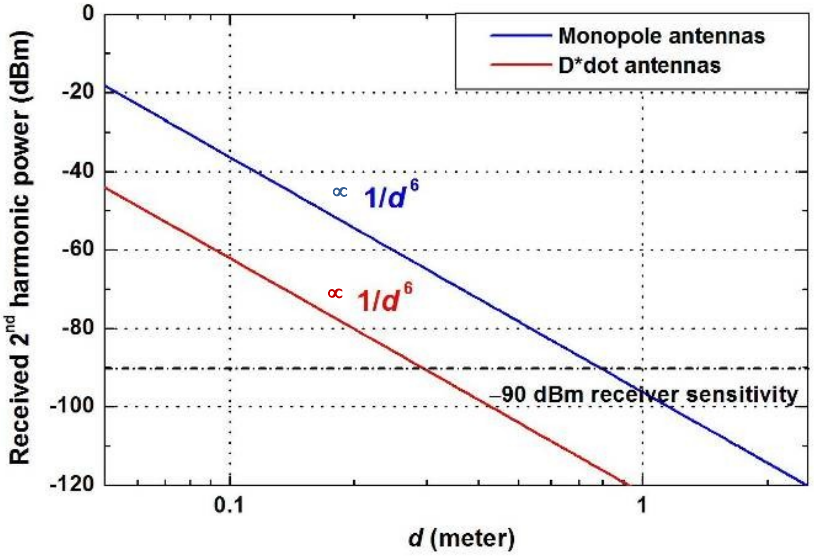

Figure 4-6. The received second harmonic power at the receiver versus the interrogation distance d with transmitting power 20 dBm and operating frequency 3.5 GHz, where $d = d_1 = d_2$. Both of the uplink distance d_2 and the downlink distance d_1 are varied.

$1/d_2^2$ from the tag back to the receiver, the NLTL-based transponder would have $1/d^6$ range behavior for the whole radio link shown in Figure 4-6, which is also found in single diode subharmonic tag [3]. From Figure 4-6, it can be found that the maximum read range is around 0.3 m for D*dot antennas and 0.8 m for monopole antennas with the receiver sensitivity of –90 dBm. The interrogation distance can be readily improved by increasing the transmitting power, enhancing the gain of transponder antennas, or using a receiver with higher sensitivity.

Similarly, to experimentally characterize the link of the reflective NLTL RFID tag, a wireless test bench has been set up as shown in Figure 4-7. The interrogation signal is at 20 dBm, and transmitted by the NIST-standard TEM horn antenna. The same receiver horn antenna is connected to the R&S® FSU spectrum analyzer. For the tag antenna, it should not only provide good input impedance match but also offer proper antenna gains (with peak gain larger than 0 dBi) and radiation patterns as omnidirectional as possible for both interrogation and second harmonic frequencies. Many dual-band or broadband antennas are sufficient to satisfy the dual-band applications, such as the double inverted-F antenna, the planar monopoles (double-L, double-T, G-shaped), the broadband fat-dipole and etc. Among these antennas, the monopole antennas have received more interests owing to their potential in providing required radiation features of dual or broad bandwidth, simple structure of a single metallic layer and easy integration with system circuit. In the test, a dual-band G-shaped monopole antenna and a broadband small monopole antenna [1, 4] are used for illustration. The G-shaped antennas comprise two folded strips L_1 and L_2 to resemble the antenna in a "G" shape. According to [4], the smaller strip L_1 mainly controls the lower operating band, while the length of L_2 affects the impedance matching condition of the higher operating band. By increasing the smaller strip length L_2 from 1.7 cm to 3.2 cm, the lower resonant mode is shifted from 4.9 GHz to 2.6 GHz, which is

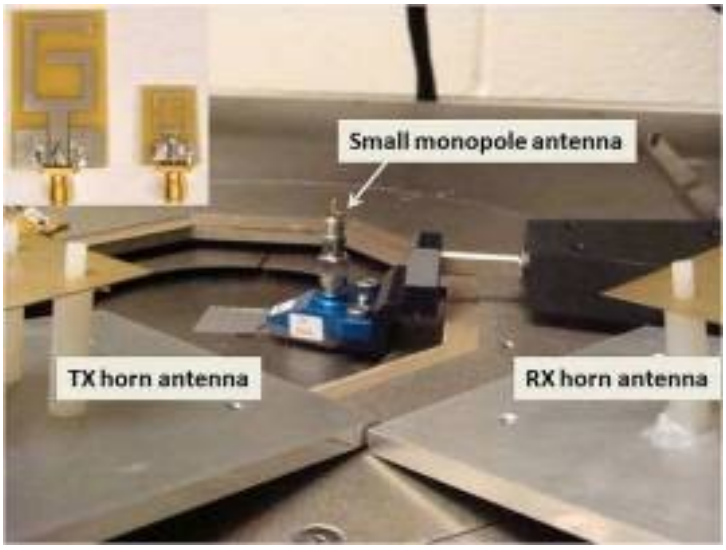

Figure 4-7 Photograph of the measurement setup showing the monopole antenna attached to the wafer probe and the G-shaped antennas in the inset.

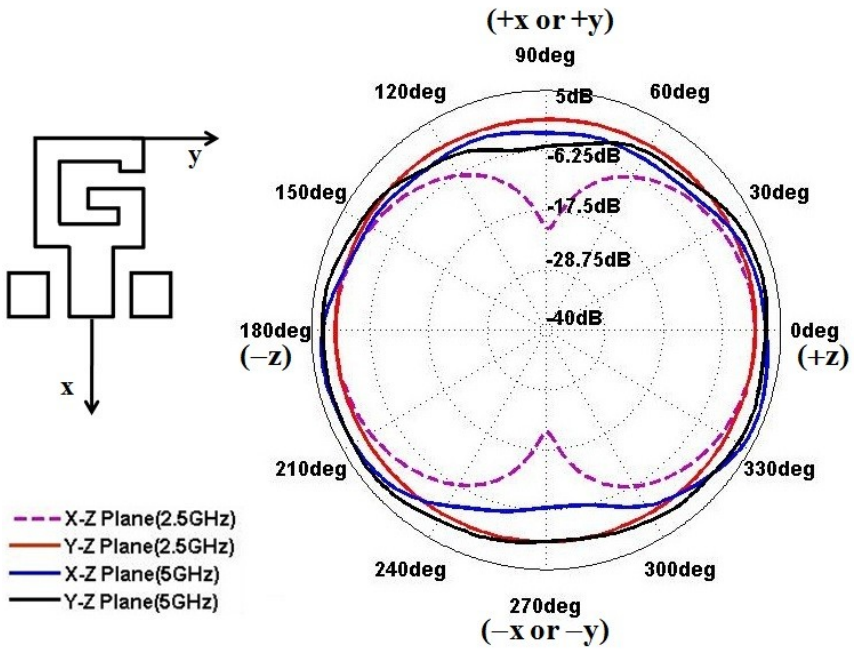

Figure 4-8 Simulated radiation pattern of G-shaped antenna modeled in HFSS.

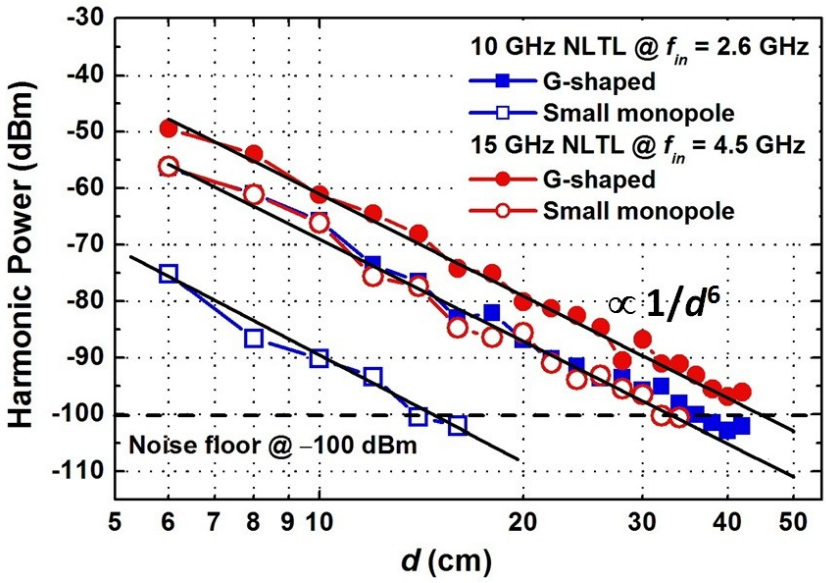

Figure 4-9 Received harmonic power for 10 GHz and 15 GHz open-ended NLTLs versus the distance between the tag and the reader.

applicable for the 15 GHz and 10 GHz GHz NLTLs respectively. Figure 4-8 shows the simulated radiation pattern of a G-shaped antenna for dual 2.5 – 5 GHz bands in Ansoft's 3D HFSS. The antenna exhibits nearly non-directional pattern in both of the x-z and y-z plane.

The small monopole antenna consists of the 7 mm extended center conductor of the coax adapter. Figure 4-9 shows the measured received 2nd harmonic power versus range for the 10 GHz and 15 GHz open-ended NLTL, respectively. We can find that the 15 GHz NLTL shows higher received harmonic power compared to the 10 GHz NLTL. This is due to better impedance matching of the small monopole and higher gains of G-shaped antennas at 4.5 GHz and 9 GHz. In our HFSS simulations, the 1.8 cm × 1.3 cm G-shaped antenna for 15 GHz NLTL has the average gains of G_r = –1.27 dBi at 4.5 GHz and G_t = +2.0 dBi at 9 GHz. When P_T = 20 dBm and K = 0.05, using the horn antennas (G_T = +3 dBi, G_R = +6 dBi) at the reader, the received harmonic

power is estimated to be around −79 dBm at the distance of d = 30 cm, compared to the measured value of −86 dBm.

The discrepancy may come from the cable, probe losses and multipath delay. Despite of the different received harmonic power, all the NLTL measurements with the antennas demonstrate the $1/d^6$ range characteristic, as we predicted in (4.3). This behavior is also found in other harmonic tags [3, 5]. With a noise floor at −100 dBm, the maximum detectable range for 10 GHz and 15 GHz open-ended NLTLs would be 35 cm and 45 cm.

4.3 Magnitude and Phase Modulation Demonstration

Utilizing the power and phase of second harmonic dependence on the bias voltage of the NLTLs, the amplitude or phase modulation schemes can be readily achieved without additional switches required [5]. By biasing the NLTL from 0 V to 1 V, the output harmonic power can be amplitude-modulated from 'On' to 'Off' states. Figure 4-10 shows the measured spectrum using monopole antennas at the two bias states with the operating frequency 3.5 GHz at the interrogation distance of 12 cm. The measured second harmonic at 7 GHz is −41. 6 dBm at 0 V bias and −86.2 dBm at 1 V bias. At the data rate of 100 MHz, the modulated second harmonic signal from the open-ended 10 GHz NLTL is captured using the Oscilloscope 86100C, shown in Figure 4-11, along with the reference bias control signal.

By tuning the bias voltage, the loaded varactor capacitance would be changed, resulting in the phase constant difference of the NLTL. Therefore, the reflected second harmonic can be also modulated with Binary Phase Shift Keying (BPSK) by switching the bias voltage as well. To avoid more Bragg reflection from the increased

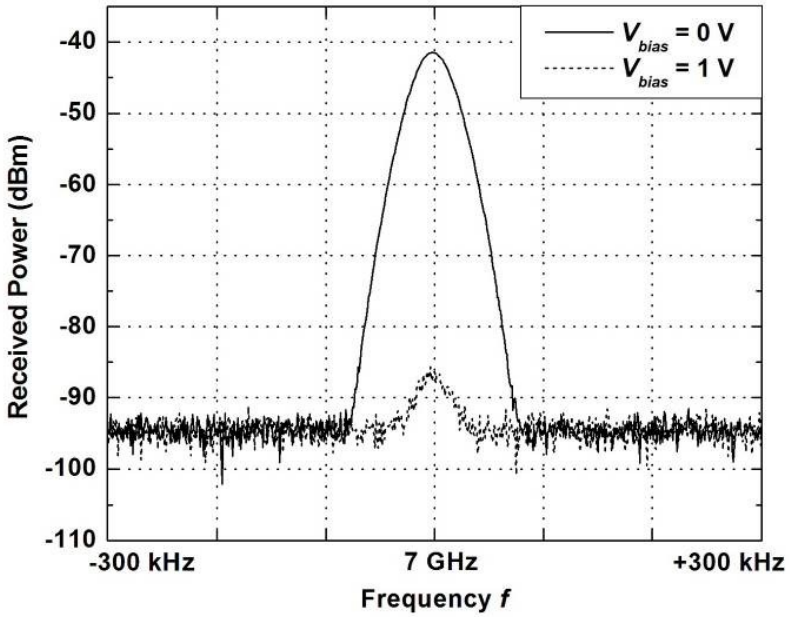

Figure 4-10 The measured spectrum with operating frequency f_{in} = 3.5 GHz and the interrogation distance d = 12 cm with V_{bias} = 0 V and V_{bias} = 1 V. Resolution bandwidth is 30 kHz.

loaded capacitance with the positive bias, the bias voltage is chosen from 0 V to –0.25 V to maintain the second harmonic amplitude while achieving 180^o phase difference according to Figure 2-7. In a bulk CMOS technology, the bias can be applied on the varactor nwells to realize negative bias voltage. Figure 4-12 shows the measured phase-modulated harmonic signals for two words '0101' and '1010' with the data rate of 100 MHz.

For both amplitude and phase modulation schemes, the maximum data rate is limited by the charging and discharging time of the varactors. For example, to achieve BPSK modulation, the varactor nwells needed to be first charged to a bias voltage of 0.25 V, then discharged to 0 V to complete the cycle. Therefore, the required time to charge and discharge the varactors imposes an upper-bound on the maximum data rate, which is around 1 GHz for the 5-stage 10 GHz open-ended NLTLs. For the NLTLs

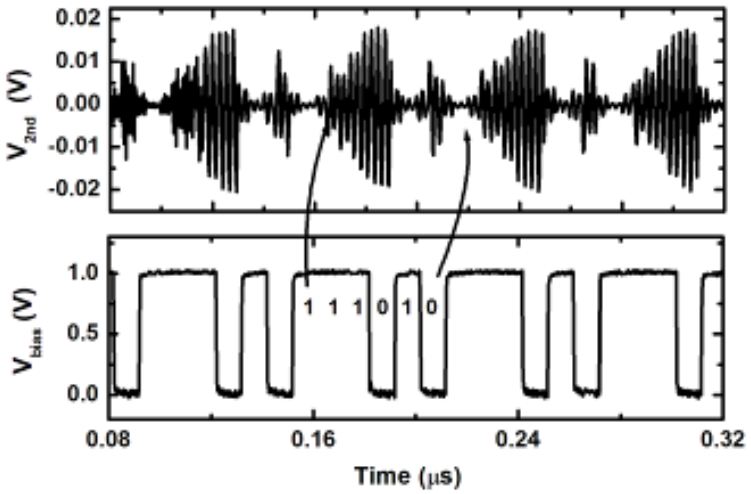

Figure 4-11 Captured output amplitude-modulated second-harmonic signal with a reference bias control signal.

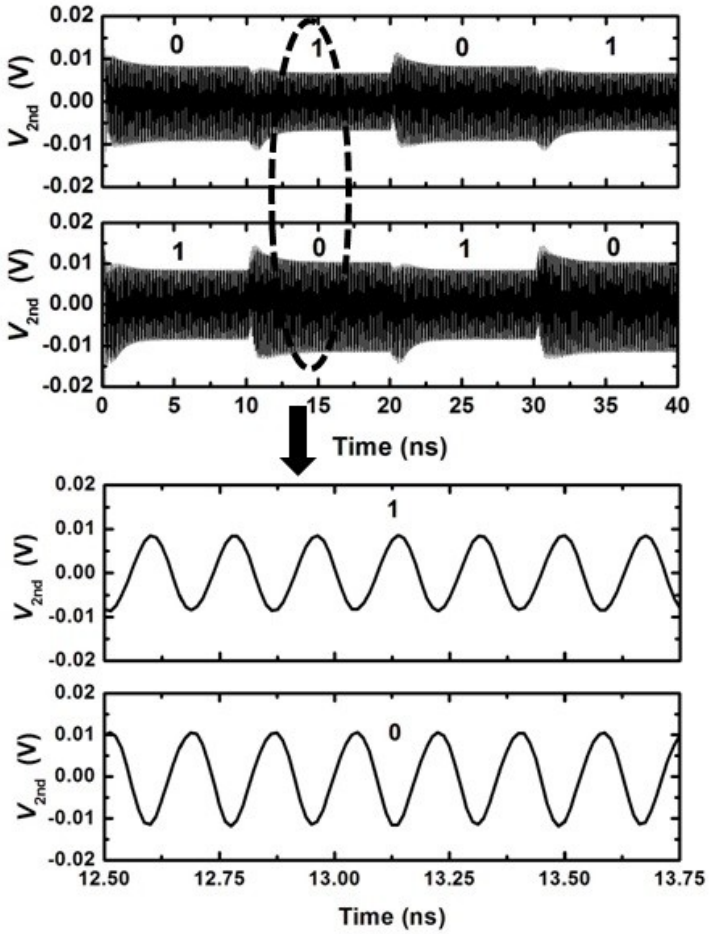

Figure 4-12 Captured output phase-modulated second harmonic signals for two words '0101' and '1010'(f_{in} = 2.6 GHz).

with higher f_{bragg}, faster data rate can be achieved with smaller loaded varactors.

4.4 Conclusion

The performance of proposed tag is summarized in Table 4-1 and compared to existing harmonic RFID transponders. Present read range of 0.45 m can be easily increased by using a high-power transmitter or a high-gain transponder antenna, since the received harmonic power P_R is proportional to the 2^{nd} power of the transmitting power P_T and the receiving gain G_r of the transponder according to (4.3). By employing the single antenna configuration, the total footprint of the device can be reduced significantly without degradation in the harmonic conversion efficiency. The reflective NLTL can also achieve reasonable dual-band impedance matching without any additional matching network. Effective data transmission between the reader and the tag is demonstrated using single G-shaped/small monopole antennas in both amplitude and phase modulation. Further optimization of antennas and interrogation power can readily extend the present reading range.

Table 4-1 Comparison with prior art.

	This work	[6]	[7]	[8]
Downlink Freq.	4.5GHz	1.3GHz	3.5GHz	0.45GHz
Uplink Freq.	9GHz	2.6GHz	7GHz	0.9GHz
Substrate	Silicon	Taconic	Paper/Plastic	Silicon
Interrogation power	0.1W	0.1W	0.1W	7 W
Read range	0.45m	/	Paper: 0.2 m Plastic: 0.3 m	18m
Conv. gain (P_{in}= −20dBm)	−30 dB	−35.4 dB	/	/
Power consumption	/	/	/	2mW
Antenna size	17 ×12 (mm^2)	10×5+8×3 (mm^2)	32×1.6+16×2 (mm^2)	/
Total Size (w/o antenna)	0.21mm^2	110 mm^2	12 mm^2	1mm^2

Implementation summary: one antenna + NLTL on integrated circuits [this work]; two antennas + discrete component assembly [6]; two antennas + discrete four-diode bridge [7]; two antennas + integrated circuits [8].

REFERENCES

[1] J. R. Andrews, "UWB signal sources, antennas and propagation," *Picosecond Pulse Labs, Boulder,* CO, Oct. 2003.

[2] N. P. Agrawall, G. Kumar, and K. P. Ray, "Wide-band planar monopole antennas," *IEEE Antennas & Propagation*, vol. 46, no. 2, pp. 294-295, Feb.1998.

[3] C. W. Pobanz, and T. Itoh, "A microwave noncontact identification transponder using subharmonic interrogation," *IEEE Trans. Microwave Theory and Tech.*, vol. 43, no. 7, pp. 1673-1679, July 1995.

[4] W. C. Liu, "Optimal design of dualband CPW-fed G-shaped monopole antenna for WLAN application," *Progress In Electromagnetics Research*, PIER 74, pp. 21-38, 2007.

[5] F. Yu, K. G. Lyon and E. C. Kan, "A novel passive RFID transponder using harmonic generation of nonlinear transmission lines," *IEEE Trans. Microwave Theory and Tech*., vol. 58, no. 12, pp. 4121-4127, Dec. 2010.

[6] S. M. Aguilar and T. M. Weller, "Tunable harmonic re-radiator for sensing applications," in *IEEE MTT-S International Microwave Symposium Digest*, pp. 1565–1568, June 2009.

[7] F. Alimenti, V. Palazzari, G. Orecchini, G. Pinca, P. Mezzanotte, M. M. Tentzeris and L. Roselli, "Crossed dipole frequency doubling RFID TAG based on paper substrate and ink-jet printing technology," in *IEEE MTT-S International Microwave Symposium Digest*, pp. 840–842, May 2010.

[8] F. Kocer and M. P. Flynn, "A new transponder architecture with on-chip ADC for long-range telemetry applications," *IEEE J.Solid-State Circuits*, vol. 41, no. 5, pp. 1142–1148, May 2006.

CHAPTER 5

ANALOG MODULATION FOR SENSOR TAGS

A novel RFID sensor tag was proposed based on open-ended non-linear transmission line (NLTL). The phase change in the reflected harmonic signal is utilized to carry the information of capacitive sensors. Comparing to the traditional phase modulation method using a single capacitive load, this new configuration achieves much larger phase variance and results in higher resolution of the sensor capacitance.

5.1 Existing Wireless RFID Sensor Tag

Radio frequency identification (RFID) sensing has attracted much attention in recent years. An RFID sensor tag, in addition to the backscattering radio components, includes a sensor that collects information from the environment [1]. When the communication between a reader and a RFID tag is in the digital form, sensor integration in the tag requires an analog-to-digital (A/D) converter [2]-[3]， which has been challenging in passive RFID tag design with RF-to-DC converters due to the size, power and cost constraints. Analog form of wireless transmission of sensor information was broadly studied. Changes in antenna resonant frequency by the integrated sensors were reported in [4]-[6]. Another proposal detects the capacitor-based sensor information by monitoring the amplitude and phase modulation in the backscattered harmonic signal [7].

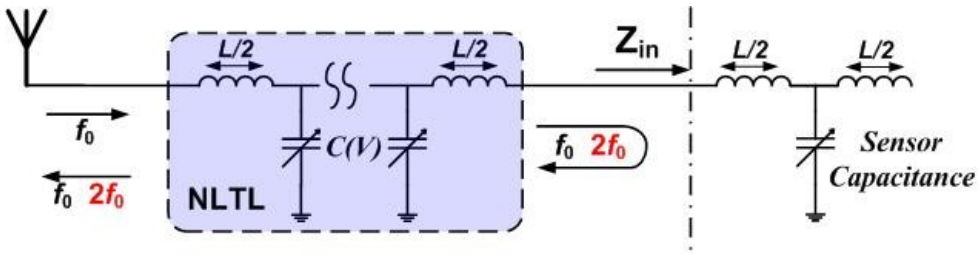

Figure 5-1. The circuit model of the open-ended NLTL integrated with a sensor capacitance near the open load.

5.2 Design Concepts of NLTL RFID Sensor Tag

Figure 5-1 shows the circuit model of the open-ended NLTL with a sensor varactor. The sensor capacitance and the series inductance are connected in the same way as the unit cell of the NLTL. By constructing a transmission line structure, the variance of the loaded sensor capacitance would change the phase constant of the LC cell, which results in the phase variance of the propagating second harmonic signal. In addition, the open load would reflect back the harmonic signal and double its phase difference due to the capacitance change.

In the following, we will investigate the characteristics of the phase variance range of the proposed topology. The input impedance looking into the sensor capacitance cell is given by:

$$Z_{in} = jZ_{NLTL}\cot(\beta_{sen}) \tag{5.1}$$

where $\beta_{sen} = arc\cos(1-\omega^2 LC_{sen}/2)$.

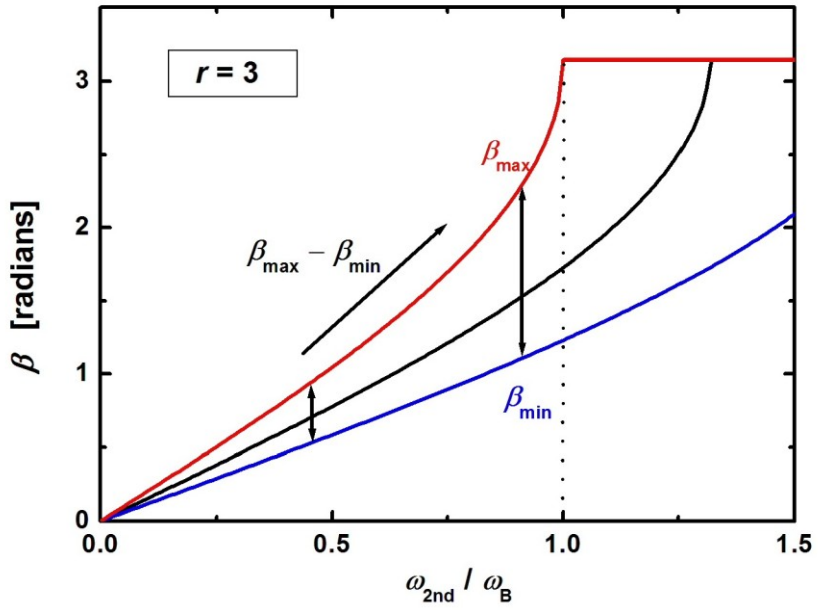

Figure 5-2 The phase constant diagram of NLTL with the capacitance ratio $r = 3$.

Z_{NLTL} is the characteristic impedance of the NLTL; β_{sen} is the phase constant controlled by the sensor varactor; C_{sen} is the center value of the sensor capacitance. Assuming the varying ratio of the sensor capacitance $r = C_{\max}/C_{\min}$, the corresponding center value would be:

$$C_{sen} = C_{\max} \Big/ \sqrt{r} = \sqrt{r} C_{\min} \tag{5.2}$$

From (5.1), the variance of the loaded sensor capacitance would result in the change of the input impedance Z_{in}, which causes a phase variation of the reflected signal:

$$\begin{aligned} \Delta\varphi &= 2\left[\tan^{-1}\left(Z_{\max}/Z_{NLTL}\right) - \tan^{-1}\left(Z_{\min}/Z_{NLTL}\right)\right] \\ &= 2\left(\beta_{\max} - \beta_{\min}\right) \end{aligned} \tag{5.3}$$

According to (5.3), the phase variance is dependent on the phase constant difference with sensor capacitance change. Figure 5-2 shows the diagram of phase constant β versus normalized frequency. By reducing the sensor capacitance, the Bragg frequency f_{bragg} would be shifted to higher frequency. This results in the phase constant difference.

5.3 Design Procedure

As shown in Figure 5-2, the phase variance is increased with increasing operation frequency. Especially when $\beta_{\max}$ just reaches π, the phase constant difference would become the largest, which in turns determines the Bragg frequency of the NLTL:

$$\omega_{bragg} = \frac{2}{Z_{\mathrm{NLTL}} C_{\max}} \tag{5.4}$$

Thus, to achieve the largest phase variance and sensitivity, ω_{bragg} should be designed accordingly to adapt to different capacitance tuning range.

Figure 5-3 shows the calculated phase variance versus capacitance ratio r with different normalized second harmonic frequencies. For comparison, the traditional way to achieve phase modulation with a single capacitive load is also shown. Increasing either $\omega_{2\mathrm{nd}}$ or r can increase the phase variance range. Due to the nonlinear relation between β and ω shown in Figure 5-2, the phase variance increased much faster close to the Bragg frequency ω_{bragg}. Especially when $\omega \to \omega_{bragg}$ and $r \to \infty$, a maximum phase variance range of 360^{o} can be reached, in comparison with the theoretical maximum 180^{o} phase shift achieved by the single capacitance configuration.

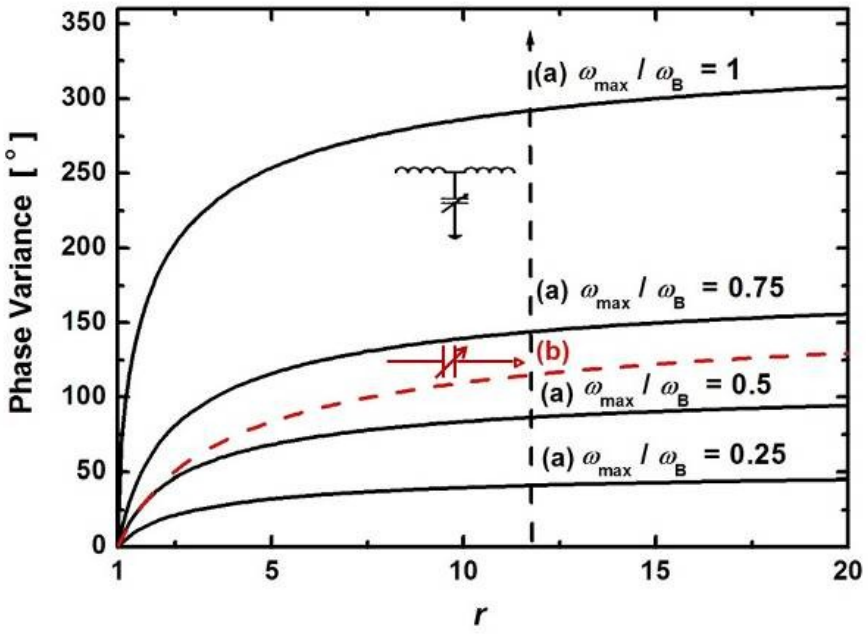

Figure 5-3 Calculated phase variance of the reflected signal versus capacitance ratio *r* (a) solid lines: NLTL with different operation frequency (b) dashed line: the traditional way using a single capacitive load.

In practical applications, the designers have little freedom to control the sensor capacitance ratio. So the most effective way to increase the capacitance resolution is to make ω_{2nd} close to ω_{bragg}. However, the second harmonic signal would be significantly attenuated if it is too close to ω_{bragg} due to the low-pass characteristic of the transmission line structure. Thus, a compromise between maximum phase variance and minimum transmission loss has to be made for a given capacitance change ratio.

To verify the concept of phase modulation, an open-ended NLTL with the varactor model of sensor capacitance is designed and simulated. The designed parameters for the NLTL are: the stage number $N = 5$ and the Bragg frequency $f_{bragg} = 8$ GHz.

By tuning the sensor capacitance from 0.5 pF to 1.6 pF, the phase of reflected second harmonic signal is simulated using the harmonic balance method, shown in

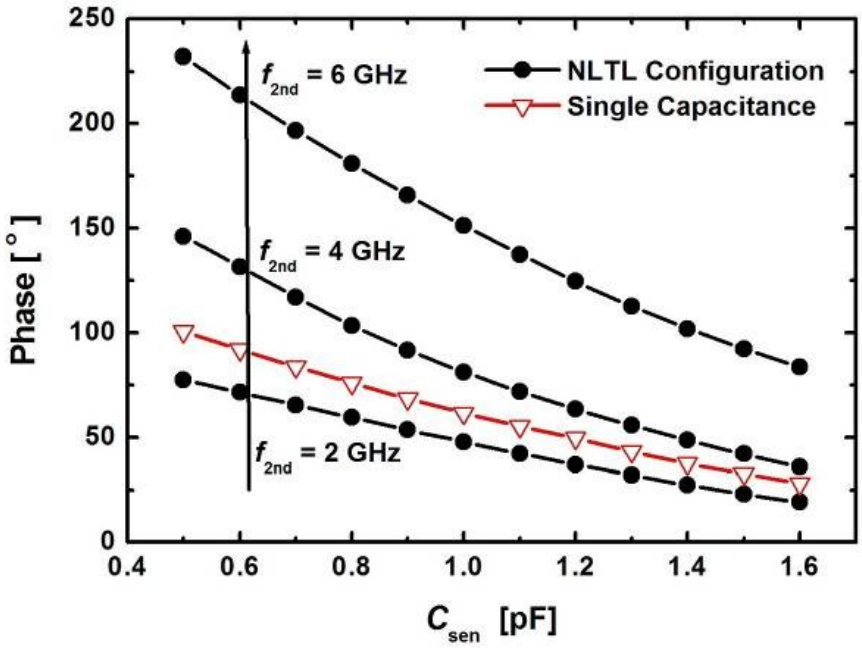

Figure 5-4 Simulated phase of the reflected second harmonic signal for the open-ended NLTL with variable sensor capacitance: (a) NLTL configuration (b) single capacitance configuration.

Figure 5-4. It can be found that the phase variance range increases with the operation harmonic frequency as well as the sensor capacitance range. With f_{2nd} increases from 2 GHz to 6 GHz, the phase variance range is increased from 60^o to 150^o. For comparison, the simulated phase for the configuration with single capacitance is also shown. Note that the single capacitance configuration achieves around 70^o phase variance with the capacitance ratio $r = 3$, which is only around half of the maximal one achieved by the NLTL configuration. Signal attenuation of the signal of $f_{2nd} = 6$ GHz is not yet serious for $f_{bragg} = 8$ GHz.

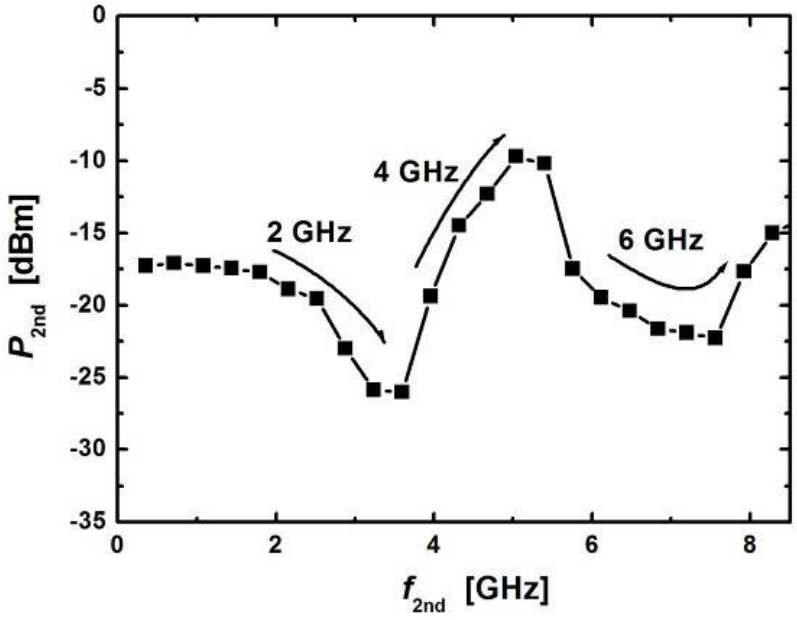

Figure 5-5 Simulated reflected 2nd harmonic power versus frequency of 5-stage open-ended NLTL.

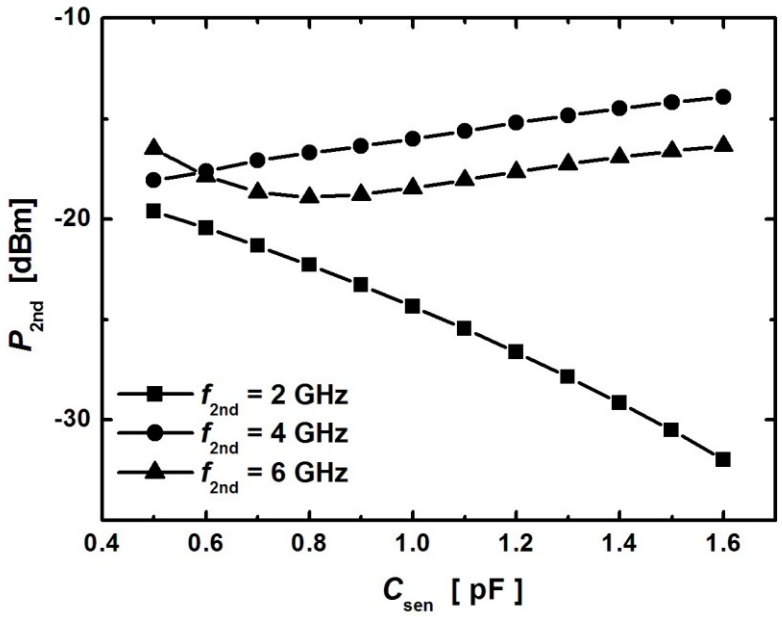

Figure 5-6 Simulated reflected 2nd harmonic power versus C_{sen} with different operation 2nd frequency.

To investigate the effect of C_{sen} on the amplitude of harmonic power (which affects range and amplitude modulation), we first simulate the reflected 2nd harmonic at different operation frequencies for 5-stage open-ended NLTL, as shown in Figure 5-5. The optimal operation frequency for maximum harmonic generation is at 5 GHz. The oscillating behavior in the harmonic power is mainly due to the cyclic input impedance of open-ended NLTL [9].

Figure 5-6 shows the reflected 2nd harmonic power with different C_{sen}. With increasing C_{sen}, the Bragg frequency f_{bragg} of the NLTL would be decreased, which corresponds to the relatively increased f_{2nd}. Thus, when f_{2nd} = 2 GHz, the reflected 2nd harmonic power decreases with increasing C_{sen}, according to Figure 5-5. This could also explain the trend how the reflected 2nd power changes with C_{sen} for f_{2nd} = 4 GHz and 6 GHz.

5.4 Prototypes and Measurements

We fabricated the 10 GHz and 15 GHz open-ended NLTLs in IBM 8RF 0.13μm CMOS process. The stage number is chosen to be 9 to generate enough harmonic power. The nMOS varactor is used to model the sensor capacitance, whose minimum-to-maximum capacitance ratio is around 3.5. By sweeping the bias voltage V_{tune} from −1 V to 1 V, the varactor capacitance varies from 290 fF to 900 fF for the 10 GHz NLTL and from 117 fF to 362 fF for the 15 GHz NLTL. Figure 5-7 shows the die photo of the 10 GHz NLTL with the model varactor. The core area of each device is around 1.08 mm × 0.42 mm, not including the RF GSG pads. To increase the phase variance range, we made f_{bragg} of the LC cell for the sensor varactor lower than the NLTL's f_{bragg} by enlarging the inductor in the last stage, which effectively reduces the difference between f_{2nd} and f_{bragg}.

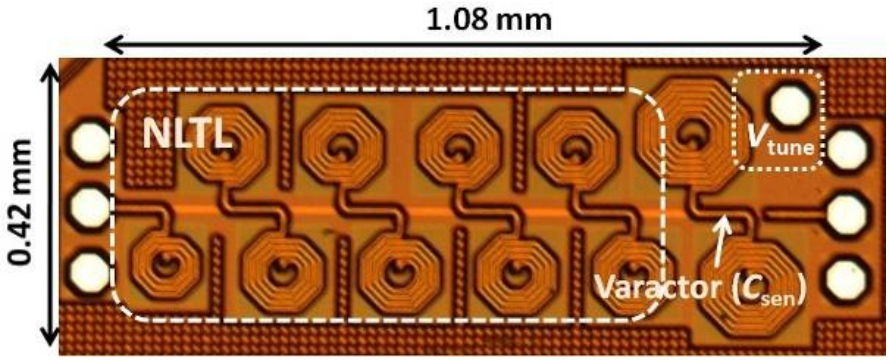

Figure 5-7 Die photo of the 10-stage open-ended NLTL with the model varactor for sensor capacitance (f_{bragg} = 10 GHz).

Using an R&S®FSU Spectrum Analyzer, we first measured the reflected second harmonic power at different frequency to find the optimal 2nd harmonic operation frequency, which is 5 GHz for the 10 GHz NLTL and 8 GHz for the 15 GHz NLTL. Figure 5-8 shows the reflected harmonic power with C_{sen} at the optimal operation frequency. The minimum power is around –21 dBm with less than 5 dBm variation, which guarantees enough signal power at the reader for the entire range of the capacitance change. Figure 5-9 shows the variation in the phase of the reflected 2nd harmonic signal with C_{sen}. The phase decreases almost linearly with increasing C_{sen}. It is observed that the phase of the reflected 2nd harmonic signal changes by 150° for both of the NLTLs. The average change in the phase of reflected signal is around 0.25° /fF for the 10 GHz NLTL and 0.61°/fF for 15 GHz NLTL. Assuming the receiver has a phase resolution of 4 mrad [10], at least 9-bit precision of sensor capacitance can be obtained with the present configurations. The number of bits could be even higher with lower noise floor of the receiver.

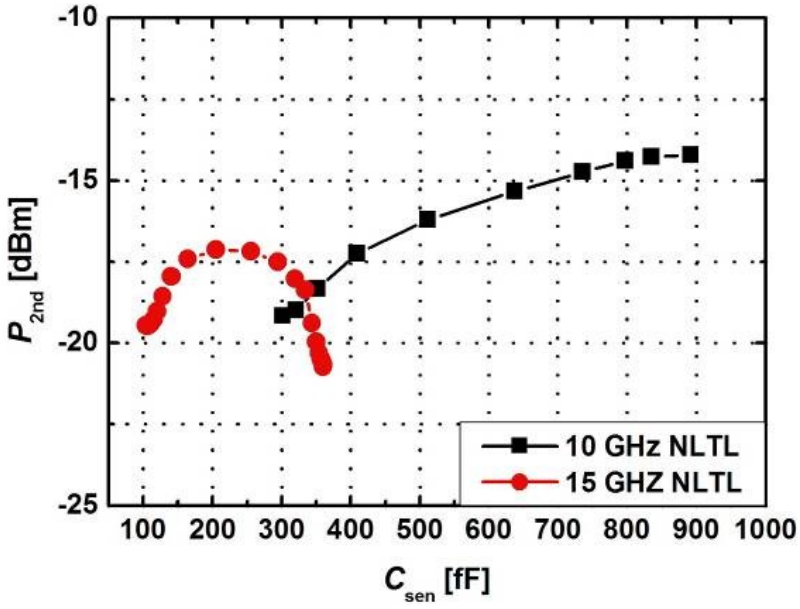

Figure 5-8 Measured 2nd harmonic power versus V_{tune}: f_{2nd} = 5 GHz (10 GHz NLTL); f_{2nd} = 8GHz (15 GHz NLTL).

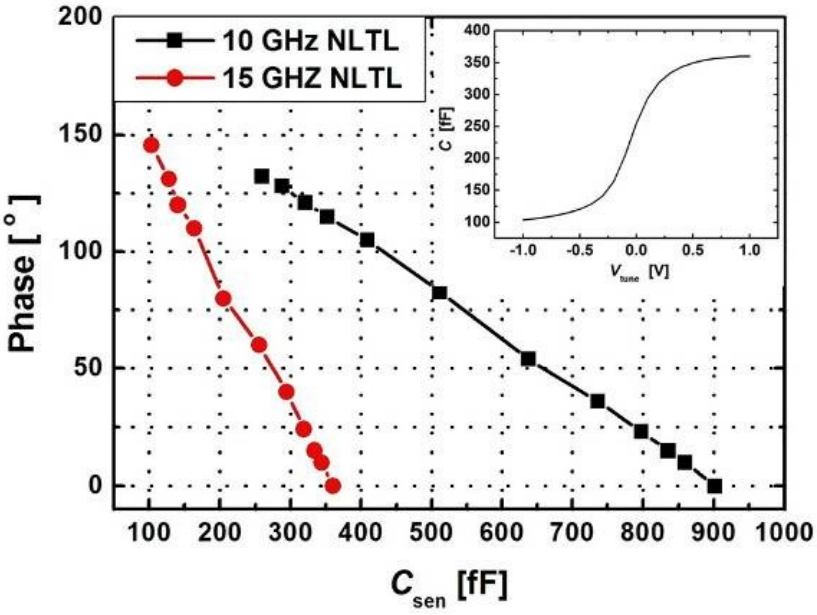

Figure 5-9 Measured phase of the reflected 2nd harmonic signal versus C_{sen}: f_{2nd} = 5 GHz (10 GHz NLTL); f_{2nd} = 8GHz (15 GHz NLTL). Inset: the C-V relation of the varactor model.

5.5 Conclusion

A novel RFID tag consisting of reflective NLTL and model sensor varactor is presented. Compared to conventional discrete load capacitance configuration, the proposed tag is able to achieve much larger phase variance, resulting in higher sensitivity for capacitive signal transduction. With the output power of –17 dBm, the tag with the 10 GHz NLTL and the 15 GHz NLTL achieves around 0.25^{o}/fF and 0.61^{o}/fF phase change in the reflected harmonic signal, respectively. Due to the small size and passive operations, the tag can be applied to a wide variety of wireless capacitive sensors.

REFERENCES

[1] K. Finkenzeller, RFID Handbook Fundamentals and Applications in Contactless Smart Cards and Identification, 2nd ed. West Sussex, U.K.: Wiley, 2004.

[2] T. V. D. Boom, D. Tessmann, R. Lerch, G. V. Bogel ; D. Hammerschmidt, J. Amelung, B. Hosticka, P. Mahdavi, "Remote cmos pressure sensor chip with wireless power and data transmission," *IEEE International Solid-State Circuits Conference*, Feb 07 – 09, 2000.

[3] F. Kocer, and M. P. Flynn, "A new transponder architecture with on-chip ADC for long-range telemetry applications," *IEEE J.Solid-State Circuits*, vol. 41, no. 5, pp. 1142–1148, May 2006.

[4] M. D. Balachandran, S. Shrestha, M. Agarwal, Y. Lvov, and K.Varahramyan, "SnO_2 capacitance sensor integrated with microstrip patch antenna for passive wireless detection of ethylene gas," *Electron. Lett.*, vol. 44, no. 7, pp. 464–466, Mar. 2008.

[5] O. Akar, T. Akin, T. Harpster, and K. Najafi, "A wireless batch sealed absolute capacitive pressure sensor," *The 14th European Conference on Solid-State Transducers*, Aug 27 – 30, 2000, Copenhagen, Denmark.

[6] K. Chang, Y. H. Kim, Y. J. Kim and Y. J. Yoon, "Functional antenna integrated with relative humidity sensor using synthesized polyimide for passive RFID sensing," *Electron. Lett.*, vol. 43, no. 5, pp.7 -8, Mar. 2007.

[7] S. Shrestha, M. Balachandran, M. Agarwal, V. V. Phoha and K. Varahramyan, "A chipless RFID sensor system for cyber centric monitoring applications," *IEEE Trans. Microwave Theory and Tech.*, vol. 57, no. 5, pp. 1303-1309, May 2009.

[8] F. Yu and K. G. Lyon, and E. C. Kan, "A novel passive RFID transponder using harmonic generation of nonlinear transmission lines," *IEEE Trans. Microwave Theory and Tech.*, vol. 58, no. 12, pp. 4121-4127, Dec. 2010.

[9] F. Yu, Y. Ma, and E. C. Kan, "Reflective nonlinear transmission lines for single-antenna non-self-jamming RFID," in *IEEE MTT-S International Microwave Symposium Digest*, June 2011.

[10] Agilent Technologies, *http://www.home.agilent.com*

CHAPTER 6

DIGITAL MODULATION FOR ID TAGS

Applications for radio-frequency identification (RFID) tags proliferates in the recent years rapidly. These include supply chain management, access control to buildings, public transportation, open-air events, airport baggage, express parcel logistics, and many more. The need for high volume, low cost, small size and large data rate is ever increasing. The NLTL-based RFID tag presented in this chapter tries to fulfill all these stringent requirements.

6.1 Architecture

Figure 6-1 shows a block diagram of the proposed system. The individual blocks are described in more detail in the following sections. The receiving and harmonic transmitting antennas are the only external component of the transponder tag. The receiving antenna is power matched to the input impedance of the IC, which consists of the average input impedance of the voltage multiplier in parallel with the NLTL. The demodulator is assumed to have infinite input impedance. The harmonic transmitting antenna is power matched to the NLTL impedance at the 2^{nd} harmonic frequency. The voltage multiplier converts a part of the incoming RF signal power to DC for power supply of all active digital circuits to read the digital memory sequentially.

To generate the system clock, we can use a ring oscillator, or the demodulator to convert the pulse-width modulated input signal to digital data and generate a synchronous system clock. The memory data from the digital part is modulated on the

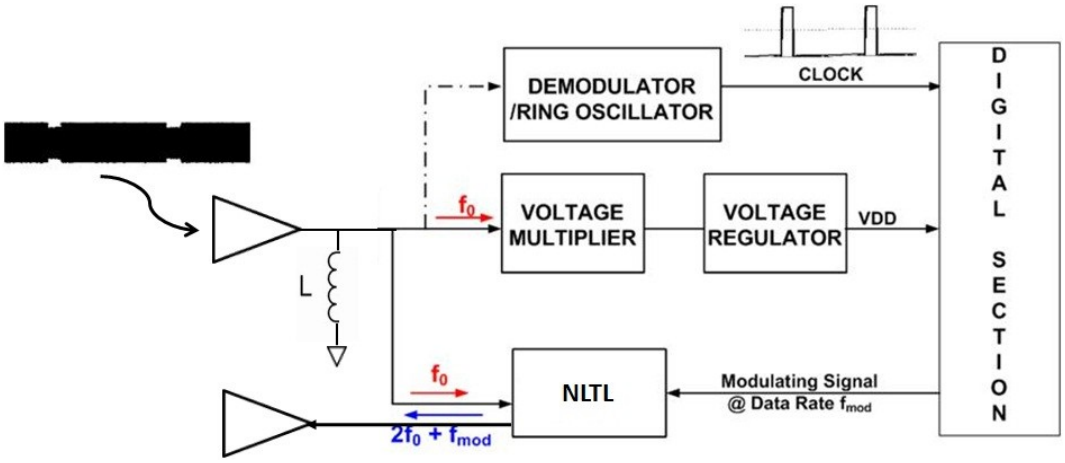

Figure 6-1 Architecture of the NLTL-based transponder RFID.

2nd harmonic signal generated by the NLTL and then sent back to the reader via the harmonic transmitting antenna.

6.1.1. RFDC convertor/voltage multiplier

In RFID tag chips, generally there is a rectifier circuit to generate DC power from the received RF power from a base station as shown in Figure 6-1. In battery-assisted RFID tags, the rectifier converts RF power to DC power when its rectified voltage surpasses the voltage of the embedded battery. Figure 6-2 shows a full-wave rectifier circuit composed of NMOS transistors connected in series. The gate and drain terminals of the NMOS are directly connected. The relationship between the input signal voltage and the generated supply voltage is approximately expressed as follows, assuming negligible leakage currents:

$$V_{DD} = N(V_{rf} - V_{th}) \tag{6.1}$$

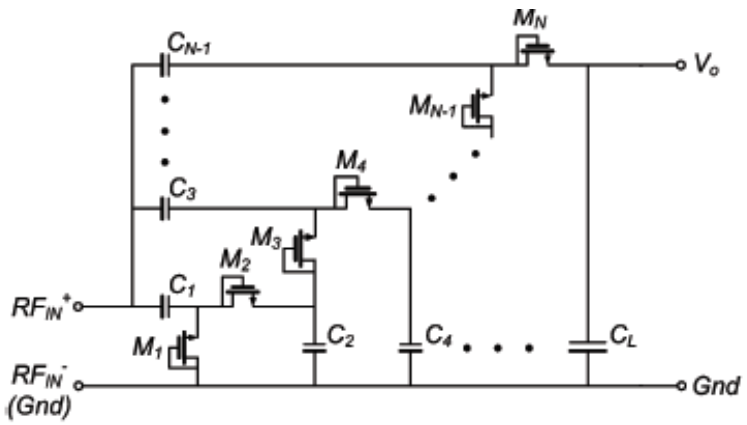

Figure 6-2 *N*-stage rectifier.

where N is the number of diodes, V_{rf} is the amplitude of the RF input signal, and V_{th} is the threshold voltage of the MOS transistors. To guarantee enough amplitude of the supply voltage with small input RF power, the MOS transistor should be chosen with either very low or zero V_{th}.

The rectifier is a key block in every remotely powered system. A thorough study is available in [1]-[2]. The model allows the prediction of the output voltage considering all the parasitic components and leakage. Furthermore, it provides the input impedance and efficiency. According to [2], the shunt resistance of N-stage rectifier can be estimated as by neglecting the parasitic capacitances:

$$R_{RFDC} = \frac{V_{rf}}{4NI_{load}} \tag{6.2}$$

From (6.1), it is clear that R_{RFDC} decreases dramatically with the increase in loading current I_{load} and the stage number N.

The conversion efficiency of rectifier η is defined as

$$\eta = \frac{V_{DD} \cdot I_{load}}{P_{avail}} \tag{6.3}$$

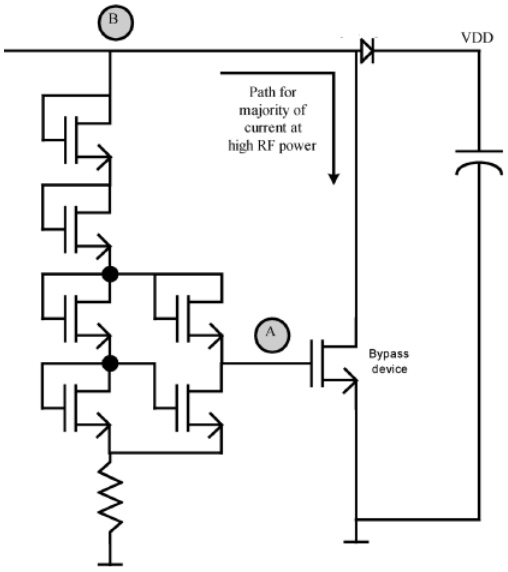

Figure 6-3 Circuit schematic for voltage regulator.

where V_{DD} is the generated supply voltage by the rectifier. P_{avail} is the available RF power to the input of the rectifier:

$$P_{avail} = \frac{V_{rf}^{\ 2}}{2R_{RFDC}} = 2NV_{rf}I_{load} \tag{6.4}$$

From (6.4), we can see that the available power to the rectifier can be increased by increasing the stage number N for given input voltage V_{rf} and loading current I_{load}.

6.1.2. Voltage regulator

In order to avoid a voltage over-drive, a voltage regulator is added at the output of the rectifier, shown in Figure 6-3. When the voltage at node B exceeds four times the MOS threshold voltage V_t, the bypass device turns on and provides an alternate path for the excess rectifier current, thereby clamping the voltage at B to nearly four times V_t. Such a voltage regulation has the advantage of simplicity. The disadvantage is that

there is a significant variation in the clamped voltage due to V_t dependence. For more elaborate designs, a bandgap-based reference can be employed.

6.2 Frontend Optimization

In conventional digital RFID tags [3]-[5], the radio link employs the same operation frequency in the uplink and downlink. For the downlink, when the tag is remotely powered by a RF signal, the communication distance of the downlink is determined by the minimum input RF power required by the tag. For the uplink, when the backscattered RF power is received by the reader, the distance is dependent on the sensitivity of the receiver. Compared the distances of two links, the downlink is usually smaller due to limited conversion efficiency of rectifier (up to 30 %) and power consumption of circuits in the tag (several μWs). Especially, the efficiency of the rectifier would decrease with smaller V_{rf} in longer distance.

For our NLTL-based RFID system, the communication distance can be decided by either the uplink distance or the downlink distance, because there is harmonic conversion loss and the 2^{nd} harmonic signal adds additional 6 dB path loss in the uplink. Based on the given system parameters, like transmitting power P_T, antenna gains, achievable rectifier efficiency η, the front-end of the RFID tag should be designed accordingly to achieve maximum communication distance.

Figure 6-4 shows the simplified circuit model of the frontend of the proposed RFID tag. The input impedance of the RFDC rectifier is represented using a shunt input resistance R_{RFDC} and shunt input capacitance. The input impedance of two-port matched NLTL is modeled as a shunt input resistance R_{NLTL}, which is frequency dependent. V_{ANT} is the open circuit voltage of the antenna and R_{ANT} is the antenna

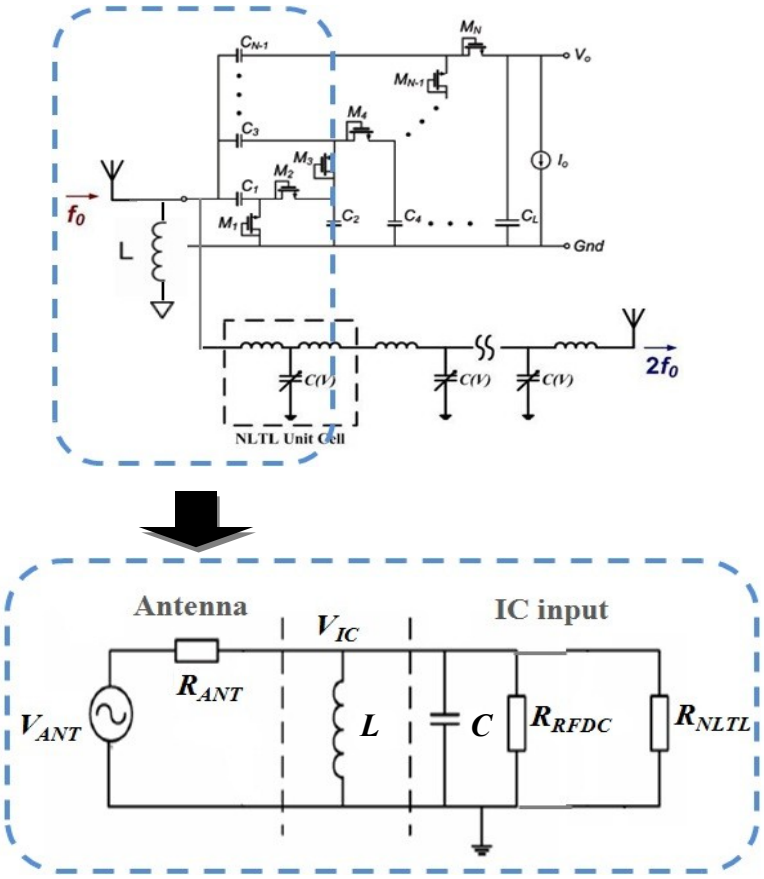

Figure 6-4 Circuit model of the frontend of NLTL based RFID tag.

radiation resistance. To achieve impedance matching, a shunt inductor is connected between the antenna and RFID frontend to cancel the capacitance presented by the RFDC rectifier. In addition, R_{ANT} should be equal to R_{RFDC} in parallel with R_{NLTL}.

According to [4], the open circuit voltage of the antenna V_{ANT} is:

$$V_{ANT} = \sqrt{8 P_{AV} R_{ANT}} \tag{6.5}$$

where $P_{AV} = A_t A_r P_T / d^2 \lambda^2$ is the available RF power from the antenna (P_T is the power transmitted by the reader, A_t and A_r is the aperture of the transmitting and receiving antennas, d is the distance between the reader and the tag). When the condition of

impedance matching is achieved, $R_{ANT} = R_{RFDC} \,||\, R_{NLTL}$ and $\omega_0 L = 1/\omega_0 C$, then the input voltage of the frontend of RFID V_{IC} is:

$$V_{IC} = \sqrt{2 P_{AV} R_{ANT}} \tag{6.6}$$

In a conventional backscattering system, all the available power will flow into the RFDC rectifier since there is no nonlinear device requiring input power to generate harmonics. In Figure 6-4, the input RF power would be divided between the rectifier and NLTL, because the antenna sees both of the rectifier shunt resistance and the NLTL impedance. As a result, the power available to the RFDC rectifier P_{RFDC} is:

$$P_{RFDC} = P_{AV} \frac{R_{NLTL}}{R_{RFDC} + R_{NLTL}} \tag{6.7}$$

Similarly, the power available to the NLTL is:

$$P_{NLTL} = P_{AV} \frac{R_{RFDC}}{R_{RFDC} + R_{NLTL}} \tag{6.8}$$

Assuming the power consumption of the active circuits in the tag is P_{IC} and the rectifier's conversion efficiency is η, the generated supply power by the rectifier needs to be larger than the required power consumption of active circuits to function correctly, which is:

$$P_{AV} \frac{R_{NLTL}}{R_{RFDC} + R_{NLTL}} \cdot \eta \geq P_{IC} \tag{6.9}$$

Given the system parameters: the transmitting power from the reader P_T, the transmitting antenna gain of the reader G_T, the receiving antenna gain of the tag G_r, the wavelength of the operation frequency λ_1 and the distance between the reader and the tag, according to Friis equation, the available RF power from the antenna P_{AV} would be:

$$P_{AV} = P_T G_T G_r \left(\frac{\lambda_1}{4\pi d} \right)^2 \tag{6.10}$$

By substituting P_{AV} with (6.10), the equation (6.9) can be rewritten as:

$$P_T G_T G_r \left(\frac{\lambda_1}{4\pi d} \right)^2 \frac{R_{NLTL}}{R_{RFDC} + R_{NLTL}} \cdot \eta \geq P_{IC} \tag{6.11}$$

From (6.11), it can be found that the maximum communication distance constrained by the downlink requirements is defined as:

$$d_{downlink} \leq \frac{\lambda_1}{4\pi} \sqrt{\frac{P_T G_T G_r R_{NLTL} \eta}{P_{IC} \left(R_{NLTL} + R_{RFDC} \right)}} \tag{6.12}$$

For a set application, the system parameters are usually given, like P_T, P_{IC}, and f_{in}. However, the designers have much freedom to design the NLTL and the RFDC rectifier to optimize the communication distance. Figure 6-5 shows the variation of the maximum downlink distance defined by (6.12) with different R_{NLTL} and R_{RFDC}. From Figure 6-5, it is clear that $d_{downlink}$ increases with larger R_{NLTL} and decreases with larger R_{RFDC}. This is because the available power to the rectifier is larger with bigger R_{NLTL}. Similarly, larger R_{RFDC} results in smaller input RF power for the rectifier.

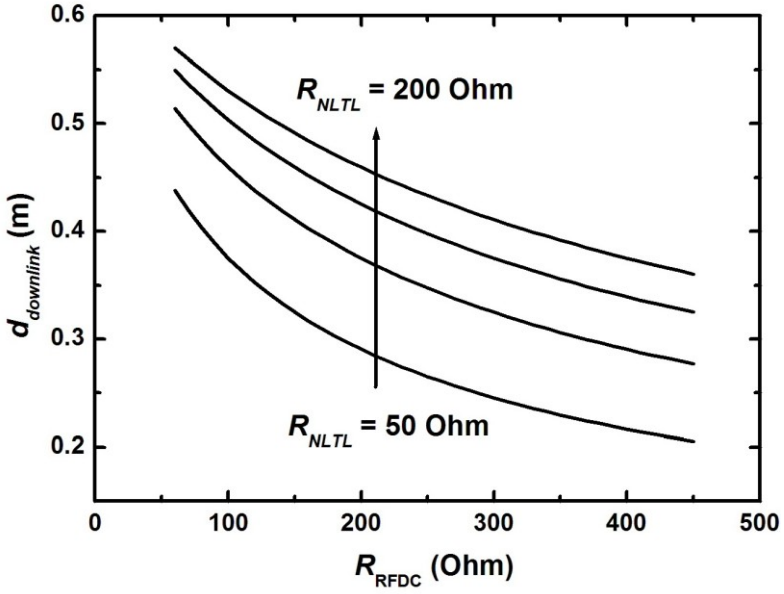

Figure 6-5. The maximum downlink distance versus the shunt resistance of RFDC rectifier with different NLTL impedance. (P_T = 0.1 W, P_{IC} = 3 μW, f_{in} = 3 GHz, RFDC: η = 10%, $G_T = G_R$ = 6 dBi, $G_t = G_r$ = 0 dBi, Reader sensitivity: −100 dBm)

For the uplink, the maximum distance is strongly dependent on the conversion efficiency of NLTL. According to (4.2), the conversion gain of the NLTL G_{2nd} is proportional to the available fundamental signal power. In (4.2), we assume the NLTL impedance has a constant value of 50 Ω. To consider the NLTL impedance's effect, (4.2) can be modified as:

$$G_{2nd} = K' R_{NLTL} P_{NLTL} \tag{6.13}$$

where $K' = 2\left(\frac{q^{(2)}(V_{bias})\gamma_2}{2q^{(1)}(V_{bias})(2\gamma_1 - \gamma_2)} \right)^2$

Thus, the generated 2nd harmonic power of the NLTL P_{2nd} is:

$$P_{2nd} = K' P_T^{\,2} G_T^{\,2} G_r^{\,2} \left(\frac{\lambda_1}{4\pi d} \right)^4 \left(\frac{R_{RFDC}}{R_{NLTL} + R_{RFDC}} \right)^2 R_{NLTL} \tag{6.14}$$

Applying Friis equation, the received 2nd harmonic power by the reader P_R is:

$$\begin{aligned} P_R &= K' P_T^{\,2} G_T^{\,2} G_r^{\,2} G_t G_R \left(\frac{\lambda_1}{4\pi d} \right)^4 \left(\frac{\lambda_2}{4\pi d} \right)^2 \left(\frac{R_{RFDC}}{R_{NLTL} + R_{RFDC}} \right)^2 R_{NLTL} \\ &= \frac{1}{4} K' P_T^{\,2} G_T^{\,2} G_r^{\,2} G_t G_R \left(\frac{\lambda_1}{4\pi d} \right)^6 \left(\frac{R_{RFDC}}{R_{NLTL} + R_{RFDC}} \right)^2 R_{NLTL} \end{aligned} \tag{6.15}$$

where G_t is the harmonic transmitting antenna gain of the tag, G_R is the receiving antenna gain of the reader. Assuming the receiver sensitivity of the reader is P_{sen}, the maximum distance of the uplink is defined as:

$$d_{uplink} \le \frac{\lambda_1}{4\pi} \sqrt[6]{\frac{K' P_T^{\,2} G_T^{\,2} G_r^{\,2} G_t G_R R_{RFDC}^{\,2} R_{NLTL}}{4 P_{sen} \left(R_{NLTL} + R_{RFDC} \right)^2}} \tag{6.16}$$

Figure 6-6 shows the variation of the maximum uplink distance defined by (6.16) with different R_{NLTL} and R_{RFDC}. When R_{RFDC} is small around 100 Ω, increasing R_{NLTL} would not help increase d_{uplink}. However, the distance increases with bigger R_{NLTL} if R_{RFDC} is larger than 250 Ω. This is because larger R_{NLTL} will decrease the available RF power for NLTL while achieve more efficient harmonic generation. With the presence of large R_{RFDC}, the effect of harmonic conversion efficiency is dominant over the available RF power. Because in the practical RFDC rectifier design, the stage number

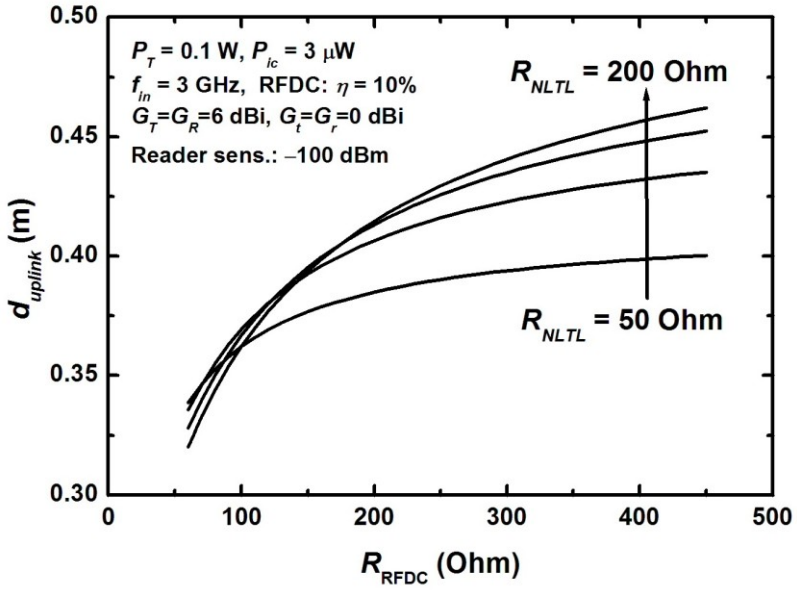

Figure 6-6 The maximum uplink distance versus the shunt resistance of RFDC rectifier with different NLTL impedance.

is less than 20 due to the efficiency and footprint considerations, which results in relatively large input impedance, often larger than 200 Ω. Therefore, a high NLTL impedance should be chosen to increase both of the uplink and downlink distances, which can be verified in the simulation, as shown in Figure 6-7. We can find that the generated supply power from the rectifier is increased from 0.2 μW to 2.5 μW and the 2nd harmonic power is also increased by 2 dB with increased R_{NLTL}. In addition, the high NLTL impedance has more improvement in the generated supply power compared to the 2nd harmonic power, which can be also found comparing Figure 6-5 and Figure 6-6.

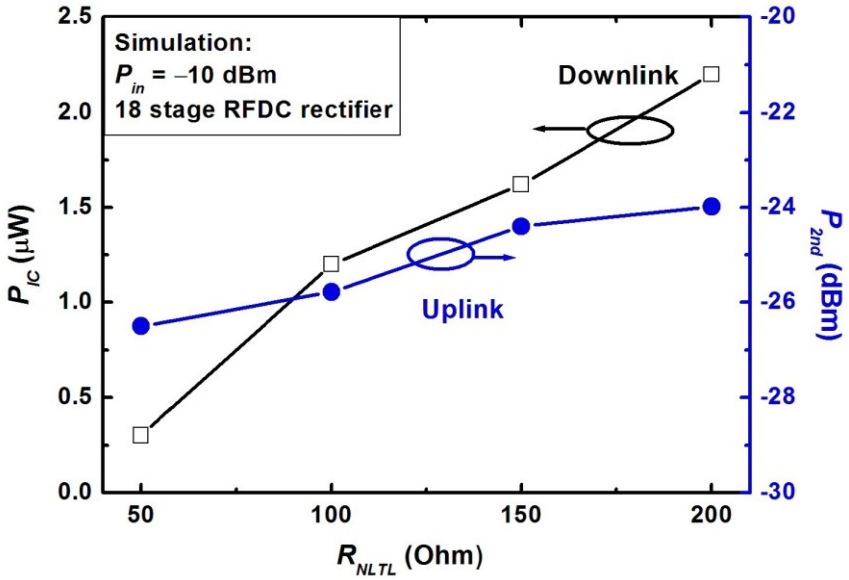

Figure 6-7 The generated supply power and 2nd harmonic power versus the NLTL impedance.

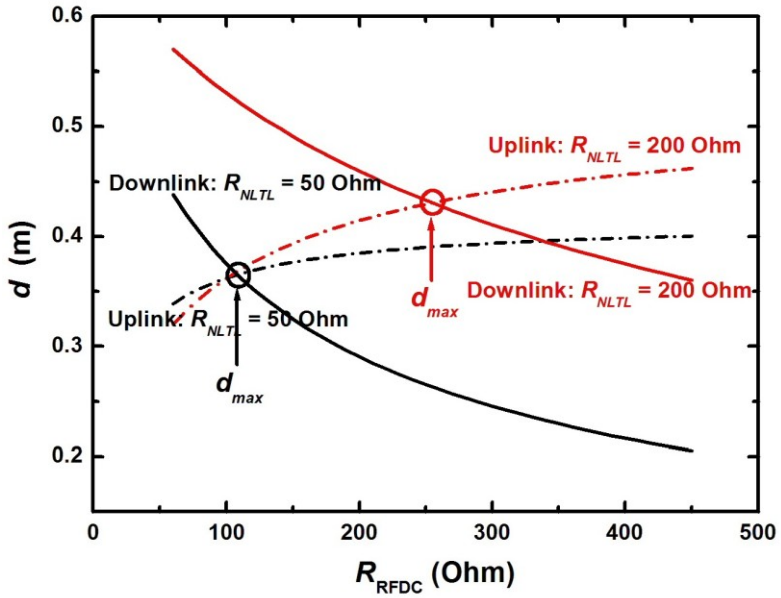

Figure 6-8 The communication distance when R_{NLTL} = 50 Ω and R_{NLTL} = 200 Ω.

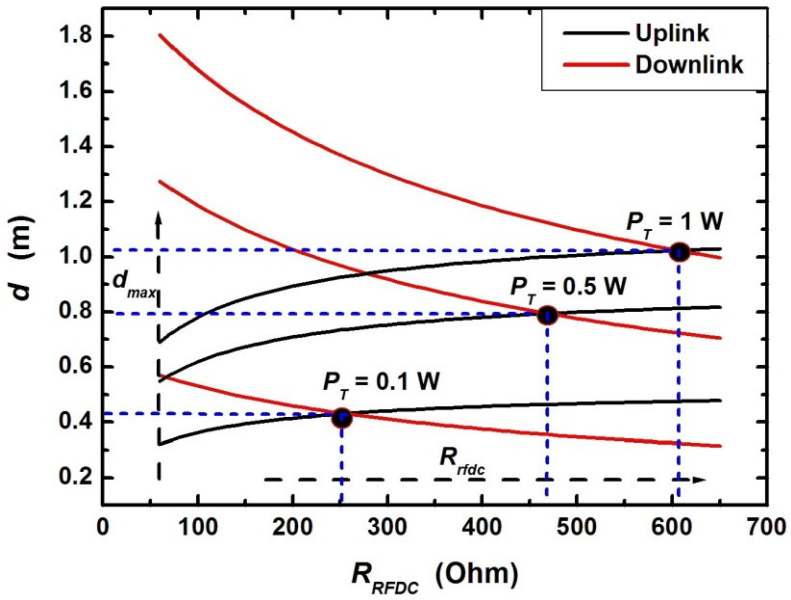

Figure 6-9. The communication distance versus R_{RFDC} with different transmitting power P_T.

Although the uplink and the downlink have their own required maximum distances, only the minimum of d_{uplink} and $d_{downlink}$ is useful in practical applications. As shown in Figure 6-8, the uplink and the downlink distances have different values with different R_{RFDC}. When R_{NLTL} = 50 Ω, to maximize the communication distance, d_{uplink} should be equal to $d_{downlink}$, which results in R_{RFDC} = 100 Ω. Similarly, the optimum R_{RFDC} should be designed to be 250 Ω to reach the maximum distance when R_{NLTL} = 200 Ω. Therefore, the optimum RFDC rectifier design is strongly dependent on the parallel NLTL's parameters to achieve maximum communication distance.

Not only the NLTL affects the optimum design of the RFDC rectifier, other system parameters like the transmitting power P_T, the IC power consumption P_{IC} will also result in different rectifier parameters for maximum communication distance, as shown in Figure 6-9 and Figure 6-10. For example, when P_T is increased from 0.1 W

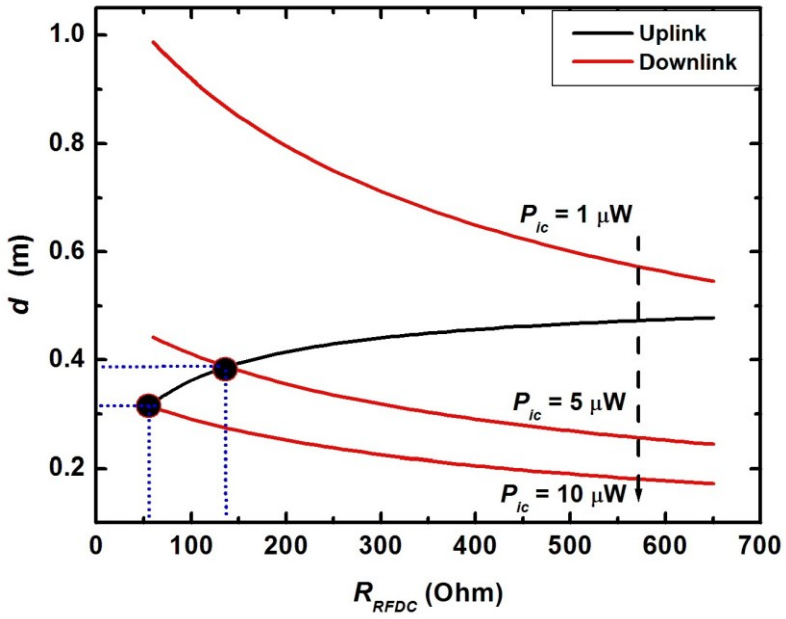

Figure 6-10. The communication distance versus R_{RFDC} with different IC power consumption P_{IC}.

to 1 W, the optimum R_{RFDC} is also increased from 250 Ω to 600 Ω. For the IC power consumption, the increased P_{IC} demands smaller R_{RFDC}.

6.3 Modulation Types

The modulator is a key part of the harmonic RFID tag. It enables the tag-to-reader communication by varying the impedance presented to the transponder's antenna in order to modulate the generated 2nd harmonic signal. Two modulation types are possible: amplitude and phase.

In a conventional RFID tag, ASK can be achieved by modulating the real part of the tag impedance while PSK can be done with the modulation of the imaginary part. In ASK [3] - [5], there is one state with power match and total reflection (short or open)

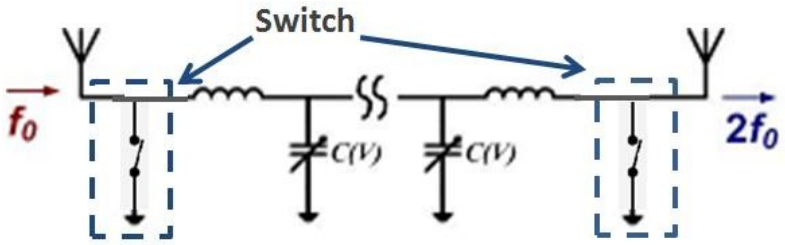

Figure 6-11. NLTL with RF switches for ASK modulation.

in the other state. If each state occupies the same time, only 50% of the available input power is actually available for rectification. In PSK [4], the available power to the tag can be kept constant during both modulation states. This could be an advantage over ASK. However, it is impossible to achieve 180^o modulation angle if the converter absorbs power in both states. Because PSK is achieved by modulating the imaginary part of the input impedance. Especially for BPSK modulation, the impedances for the two states are $Z_{in} = \pm jX_{in}$, which would make the tag totally reflective in both of two states. Hence, there exists a strict tradeoff between the power available to the tag and the power devoted to the backscattered communication.

For the NLTL-based RFID tag, there are mainly two ways to do the modulation. The first method is using the RF switch to achieve ASK modulation, as shown in Figure 6-11. The switch can be either implemented at the input port of NLTL to modulate the tag impedance as the conventional RFID tag or at the output port of NLTL to modulate the NLTL loaded impedance. Compared to the input implementation, the switch at the output port would not be totally reflective in one state, which is more advantageous in the power efficiency.

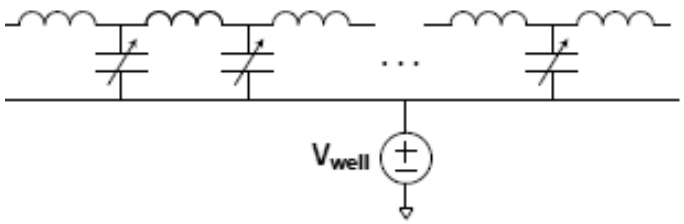

Figure 6-12. NLTL with bias variation for ASK and PSK modulation.

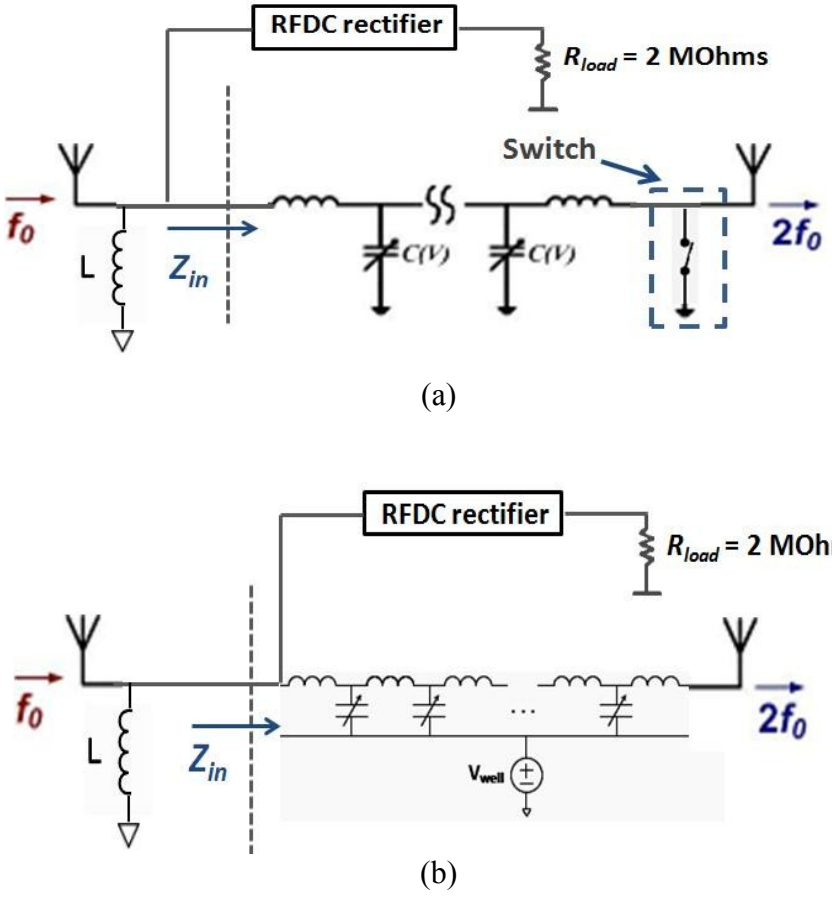

Figure 6-13. ASK modulation (a) ASK I with switch (b) ASK II with bias variation.

The other method to achieve modulation is utilizing the characteristics of NLTL. As shown in Figure 2-7, the amplitude of 2nd harmonic signal is dependent on the nonlinearity of the loaded varactors, which can be controlled by the bias voltage. By switching the bias voltage from 0 V to 1 V, ASK modulation can be achieved. Similarly, the sharp phase change and almost constant harmonic amplitude around 0 V bias make the PSK possible. The detailed implementation of bias modulation is shown in Figure 6-12, which is similar to the implementation in Chapter 4.

6.3.1. ASK modulation

Figure 6-13 shows the two types of ASK modulation. For ASK modulation, one most important thing need to be taken into account is the RF power available for DC supply power generation. It is hence necessary to compare the input impedance at two different states. For ASK I, the input impedance Z_{in} shown in Figure 6-13 (a) when switch is ON and OFF is:

State 'ON': $$Z_{in} = Z_{NLTL} \| Z_{RFDC} \tag{6.17}$$

State 'OFF': $$Z_{in} = Z_{NLTL} \tanh(\gamma N) \| Z_{RFDC} \tag{6.18}$$

where $\gamma = \alpha + j\beta$ is the propagation constant.

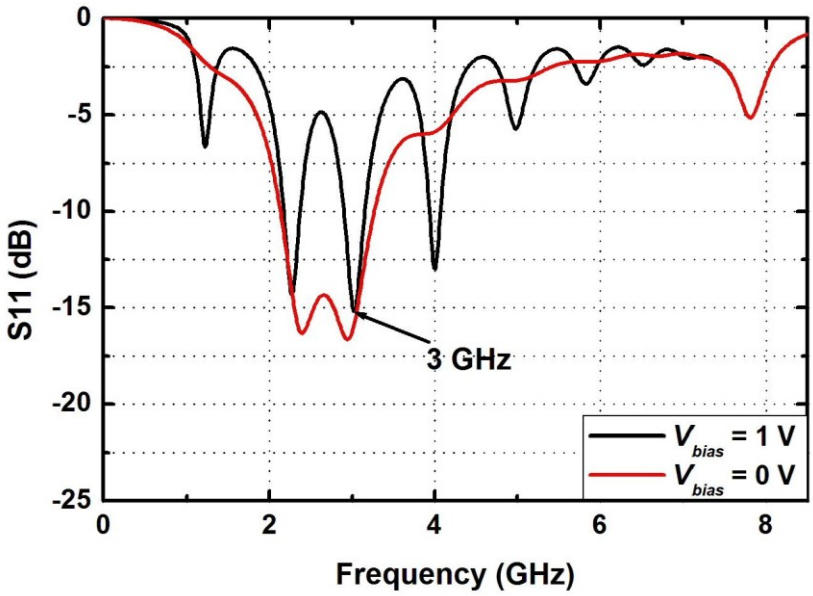

Figure 6-14. The input matching of NLTL based tag with ASK I modulation in two states with V_{bias} = 0 V and V_{bias} = 1 V.

When $\beta = (2k+1)\pi / 2N$, the imaginary part of $\tanh(\gamma N)$ vanishes and (6.18) can be extended as:

$$Z_{in} = Z_{NLTL} \frac{e^{\beta N/Q}+1}{e^{\beta N/Q}-1} \| Z_{RFDC} \tag{6.19}$$

In TSMC 65nm CMOS process, Z_{in} of state 'OFF' would be decreased from 5.0 Z_{NLTL} || Z_{RFDC} to 1.06 Z_{NLTL} || Z_{RFDC} , which is pretty close to Z_{in} of state 'ON', when β is increased from π / N to $9\pi / N$ with Q = 8 and N = 10. For a given frequency and technology, the Bragg frequency f_{bragg} and the stage number N of the NLTL can be designed to achieve a small variation in Z_{in} for reasonable impedance matching in both states. As shown in Figure 6-14, for the interrogation signal at 3 GHz, a NLTL with f_{bragg} = 10 GHz and N = 10 achieves $S_{11} < -15$ dB in both modulation states.

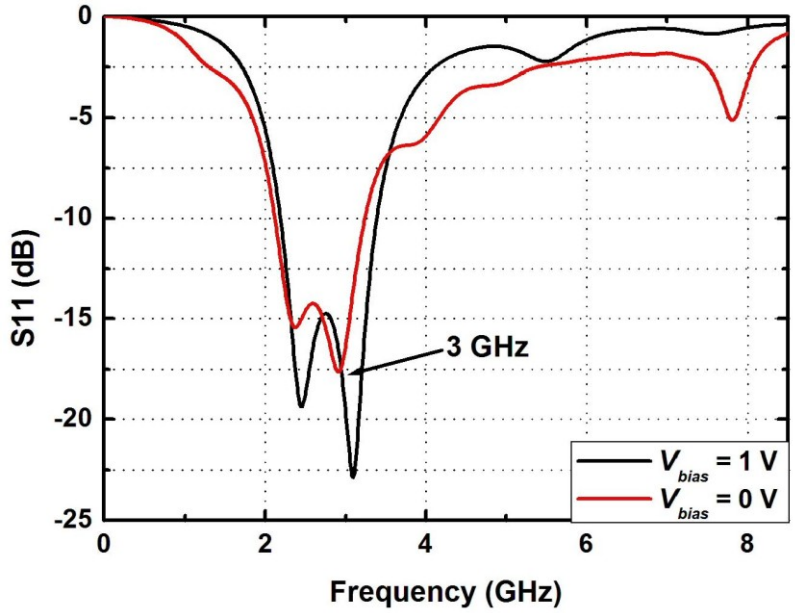

Figure 6-15. The input matching of NLTL based tag with ASK II modulation in two states with V_{bias} = 0 V and V_{bias} = 1 V.

Similarly, we can also get the input impedance of ASK II shown in Figure 6-13 (b) at two states:

state 'ON': $$Z_{in} = Z_{NLTL} || Z_{RFDC} \tag{6.20}$$

state 'OFF': $$Z_{in} = \left(\sqrt{C_0 / C_{\min}} Z_{NLTL} \right) || Z_{RFDC} \tag{6.21}$$

where C_0 is the varactor capacitance at V_{bias} = 0V and C_{min} is the varactor capacitance at V_{bias} = 1V. With a typical C_0/C_{min} = 2 in TSMC 65nm process, Z_{in} in OFF state is around $(1.4Z_{NLTL}) \,||\, Z_{RFDC}$, which would be close to Z_{in} in ON state. As shown in Figure 6-15, both states achieve good matching with ASK II modulation.

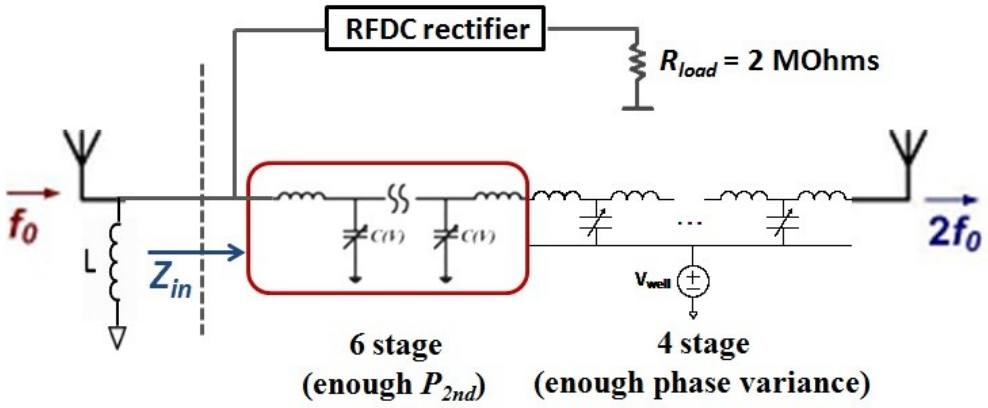

Figure 6-16. Circuit schematic of PSK modulation.

6.3.2. PSK modulation

For PSK modulation, a 6-stage zero-biased NLTL is first utilized to generate enough 2nd harmonic power. It is followed by a 4-stage NLTL with switchable bias voltage to achieve enough phase variance between two different states, as shown in Figure 6-16. Because the changed load capacitance will result in different phase constant of NLTL, the phase of propagating 2nd signal would be also changed with two different bias voltages 0 V and 1 V. The achieved phase variance is defined as:

$$\Delta\varphi = 4\left(\beta_{\max} - \beta_{\min}\right) \tag{6.22}$$

As shown in Figure 6-17, the phase variance of the propagating signal can be achieved by changing the bias voltage. The phase difference between the two states increases with the operation frequency.

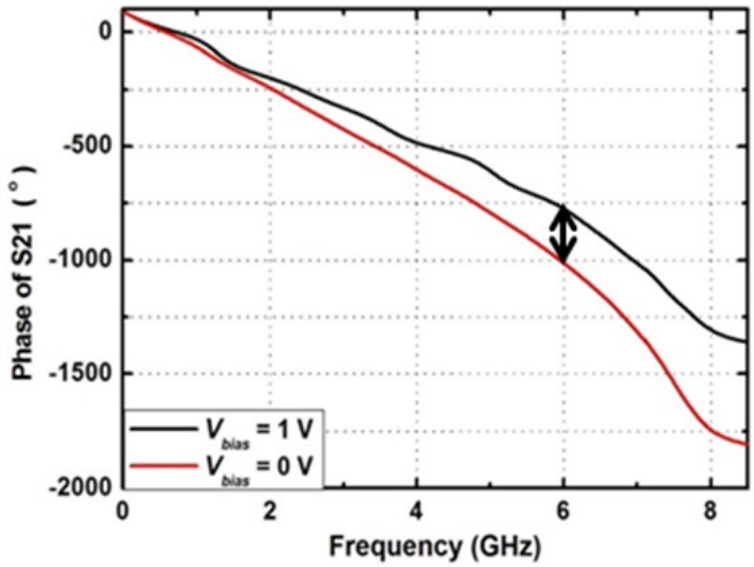

Figure 6-17. Phase of S_{21} parameter with V_{bias} = 0 V and 1 V.

To investigate the power efficiency of the downlink, the input impedances of two states shown in Figure 6-16 are found to be:

state '1': $$Z_{in} = Z_{NLTL} \| Z_{RFDC} \tag{6.23}$$

state '2': $$Z_{in} = Z_{NLTL} \frac{\sqrt{C_0 / C_{\min}} + \tanh(6\gamma)}{1 + \sqrt{C_0 / C_{\min}} \tanh(6\gamma)} \| Z_{RFDC} \tag{6.24}$$

Similar to ASK I, the impedance variation can be minimized by choosing suitable f_{bragg} of NLTL for a given operation frequency. As shown in Figure 6-18, for the peration frequency at 3 GHz, the input matching with S_{11} < -12 dB can be achieved for both states with a f_{bragg} = 10 GHz NLTL.

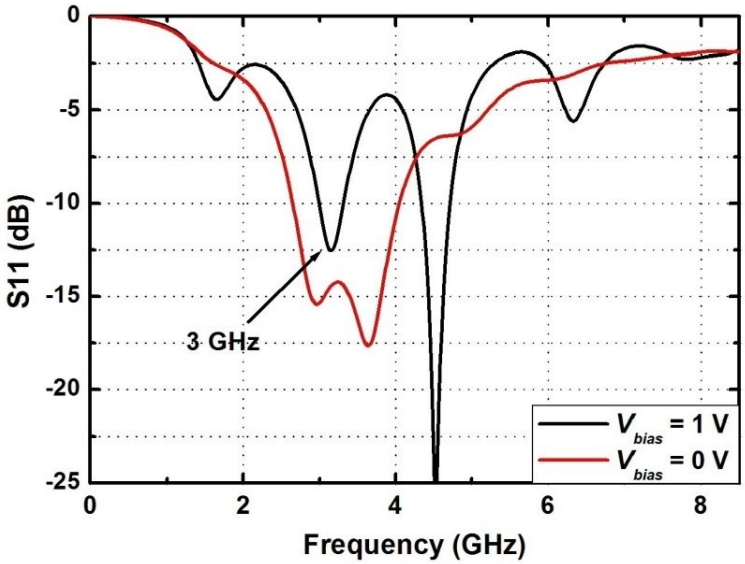

Figure 6-18. The input matching of NLTL based tag with PSK modulation in two states with V_{bias} = 0 V and V_{bias} = 1 V.

6.3.3. Modulator efficiency

After introducing three types of modulation, this section discusses whether it is more advantageous to use ASK or PSK modulation. In this analysis, two things need to be taken into account: the generated supply power and the modulated power for the down link.

a. Power Supply Efficiency:

The dc power generation for the two impedance states 1 and 2 is given by:

$$P_{IC} = p_1 \frac{V_{dd,1}^{\ 2}}{R_{load}} + p_2 \frac{V_{dd,2}^{\ 2}}{R_{load}} \tag{6.25}$$

where p_1 and p_2 are the fraction time of states 1 and 2, $V_{dd,1}$ and $V_{dd,2}$ is the generated supply voltage, and R_{load} is effective load impedance of the circuit in the tag.

	ASK I (switch)	ASK II (bias)	PSK (bias)
V_{dd}	0.75 V	0.78 V	1.25 V
	1.02 V	0.78 V	0.63 V
V_{2nd}	8.9 mV	8.9 mV	9.24 mV, 129°
	1.2 mV	1.48 mV	5.5 mV, –24°
P_{IC}	0.40 μW	0.30 μW	0.49 μW
P_{mod}	148 nW	136 nW	514 nW
P_{cap}	5 nW @ 100 kHz	60 nW @ 100 kHz	24 nW @ 100 kHz
	50 nW @ 1 MHz	600 nW @ 1 MHz	240 nW @ 1 MHz

Table 6-1 Performance summary of three modulation types (P_{in} = –15 dBm, R_{load} = 2 MΩ, R_{ant} = 100 Ω, $p_1 = p_2$ =0.5).

b. Modulation Efficiency:

Assuming that both states are active with equal amount of time, $p_1 = p_2 = 0.5$, the modulated power is:

$$P_{\text{mod}} = \frac{v_{2nd,1}{}^2 + v_{2nd,2}{}^2 - 2v_{2nd,1}v_{2nd,2}\cos(\Delta\theta)}{4R_{ant}} \tag{6.26}$$

where $V_{2nd,1}$ and $V_{2nd,2}$ are the generated 2nd harmonic amplitude of states 1 and 2, $\Delta\theta$ is the phase difference between the 2nd harmonic signal in the two states.

To compare the three modulation types, Table 6-1 summarizes the simulated performance of ASK I, ASK II and PSK. It can be seen that all the three modulation types can receive RF power to generate supply voltage in both of two states, resulting the generated dc power around 400 nW with P_{in} = –15 dBm. For the reverse link, PSK

exhibits more than three times larger modulation power compared to ASK. Since ASK II and PSK need to change the bias of the varactors, there would be additional capacitive charging energy of the NLTL. For ASK II, the charging power P_{cap} is increased from 60 nW to 600 nW when the data rate is increased from 100 kHz to 1 MHz. For PSK, the charging power is much lower compared to ASK II due to less switch biased varactors. However, P_{cap} is still up to 240 nW at 1 MHz data rate, which can't be negligible in passive RFID tag. Therefore, for the applications requiring high data rate faster than 1 Mb/s, ASK I with switch is more suitable considering the efficient power supply generation and the reasonable modulation efficiency. For those applications operating at 100 – 600 kb/s, PSK is a better choice for its much higher modulation power.

6.4 Design Example

A NLTL based digital RFID tag is designed as shown in Figure 6-1. The digital section consists of 256 bits Read-Only-Memory (ROM) and its logic control circuits. The power consumption of the digital part is up to 200 nW with 1 V supply voltage. The ring oscillator is used to generate the system clock, which operates at 1 MHz and dissipates around 250 nW. To enhance the communication distance, the NLTL impedance is designed at 200 Ω. For the RFDC rectifier, diodes are implemented as diode-connected zero V_t NMOS transistors. 18 stages are cascaded to generate the DC voltage higher than 0.8 V. With a 2 MΩ load resistor and an input power of 63 μW at 3 GHz, the output DC power is 6.2 μW, which corresponds to a power efficiency of 9.84 %. The efficiency would be higher with increasing input power.

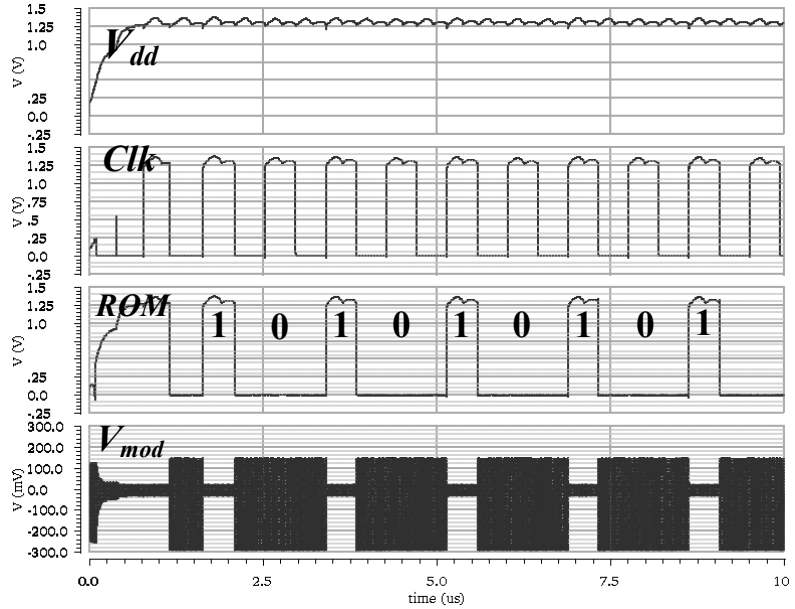

(a)

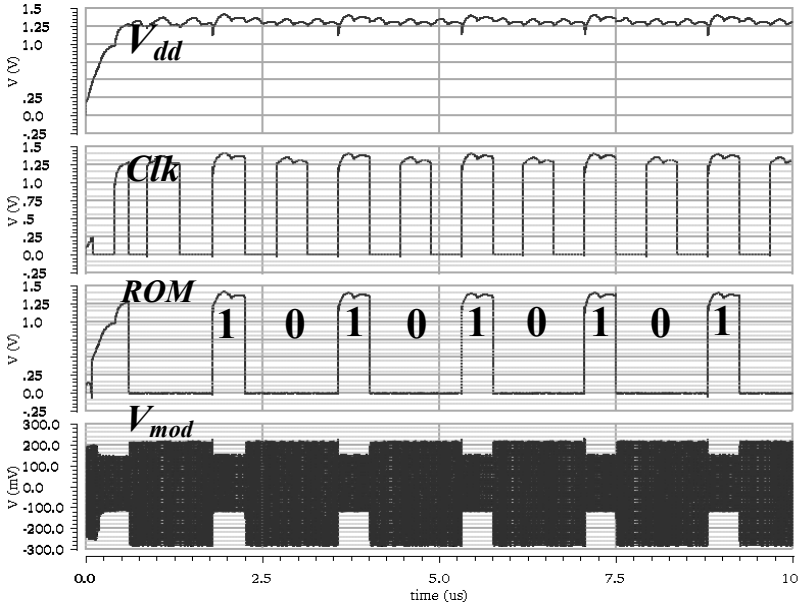

(b)

Figure 6-19. System simulation results with the modulation (a) ASK I (b) PSK (P_{in} = 0 dBm, f_{in} = 3 GHz).

Technology	TSMC65nm
Downlink Frequency	3 GHz
Uplink Frequency	6 GHz
Data Rate	1 Mb/s
Typical Tag Sensitivity	−15 dBm
Typical Distance	5.6 m (@4 W)
P_{2nd} (@ RX of Reader)	−85 dBm
ROM	256 bits

Table 6-2. Performance summary of the NLTL based digital RFID tag with ASK I.

Figure 6-19 shows the simulated performance of the NLTL based RFID tag with different modulation methods. As shown in Figure 6-19 (a), the supply voltage V_{dd} is charged from 0 V to 1.25 V with the input power of 1 mW. After V_{dd} reached the minimum operating voltage, the ring oscillator starts to generate the system clock *Clk* at 1 MHz, which drives the digital circuits (ROM). And the output of the memory would modulate the 2nd harmonic output of the NLTL, as shown in the last curve of Figure 6-19 (a). Due to the significantly long simulation time, there is no extra decoupling capacitance connected between the generated V_{dd} and the ground. That is the reason of the small ripples in V_{dd}. For PSK modulation scheme, it can be seen that there is bigger drop in V_{dd} during the rise time of the data bits '1' in the output of ROM, compared with ASK I using switch. This is due to the extra capacitive charging power requested by the biasing method of PSK, which is more obvious at the data rate larger than 1 Mb/s. The performance of the system with ASK I modulation is summarized in Table 6-2. At the pulse rate of 1 MHz, the typical communication

distance of the tag is 5.6 m with the interrogation power of 4 W at carrier frequency of 3 GHz.

6.5 Conclusion

In this Chapter, we present a passive NLTL based transponder with digital modulation. The system architecture and the operation of key circuit blocks are described respectively. To achieve the maximum communication distance, optimization analysis has been done for the coordinated design of the NLTLs and the RF-to-DC rectifier. In addition, different modulation types based on NLTLs are discussed and compared considering both of the rectification and modulation efficiency. The simulation results show an operating range of 5.6 m can be achieved with 4 W transmitted power and the estimated system power consumption of around 500 nW.

REFERENCES

[1] J. Yi, W.-H. Ki, and C.-Y. Tsui, "Analysis and design strategy of UHF micro-power CMOS rectifiers for micro-sensor and RFID applications," *IEEE Trans. Circuits Syst. I*, Reg. Papers, vol. 54, no. 1, pp. 153–166, Jan. 2007.

[2] R. E. Barnett, J. Liu, and S. Lazar, "A RF to DC voltage conversion model for multi-stage rectifiers in UHF RFID transponders," in *IEEE Journal of solid-state circuits*, vol. 44, No. 2, Feb. 2009, pp. 354–370.

[3] R. Barnett, G. Balanchandran, S. Lazar, B. Kramer, G. Konnail, S. Rajasekhar, V. Drobny, "A passive UHF RFID transponder for EPC Gen 2 with -14dBm sensitivity in 0.13 μm CMOS," *ISSCC Dig. Tech. Papers*, pp. 582-583, Feb. 2007.

[4] U. Karthaus and M. Fischer, "Fully integrated passive UHF RFID transponder IC with 16.7-μW minimum RF input power," *IEEE J.Solid-State Circuits*, vol. 38, no. 10, pp. 1602–1608, Oct. 2003.

[5] J. Curty, N. Joehl, C. Dehollain, M. J. Declercq, "Remotely powered addressable UHF RFID integrated system," *IEEE J.Solid-State Circuits*, vol. 40, no. 11, pp. 2193–2202, Nov. 2005.

CHAPTER 7

TAPERED NLTLS

7.1 Introduction

ULTRA-WIDEBAND (UWB) impulse radio (IR) can provide location and tracking capabilities for sensor networks [1], where the main goal is to reduce power consumption and complexity for longer battery life. It is essential to have an energy-efficient transmitter and shift the complexity to the master device which often has more relaxed power budget.

In the UWB-IR transmitter, many technologies have been developed to meet the spectral mask of 3.1–10.6-GHz set by Federal Communication Commission (FCC) [2]. One such example [3] used a switchable microwave oscillator to generate pulses with a well controlled spectrum. Another proposal used edge combining to generate a short impulse, followed by a bandpass filter to determine the final pulse spectrum [4]. Although these techniques achieve the low energy consumption in the 9– 18 pJ/pulse range, it is difficult to use them above 10 GHz due to the significantly larger power with higher frequency. Our previous work used nonlinear transmission line (NLTL) [5] to generate pulses close to the Bragg frequency and had energy scaling with the inverse of frequency, which is favorable for UWB-IR transmitters above 10 GHz.

In this chapter, we present a new IR transmitter design based on the tapered NLTL to further reduce energy consumption by progressively raising the effective Bragg frequency. In addition, the maximum pulse rate can be increased by decreasing the inductance and varactor sizes gradually, leading to larger operating bandwidth.

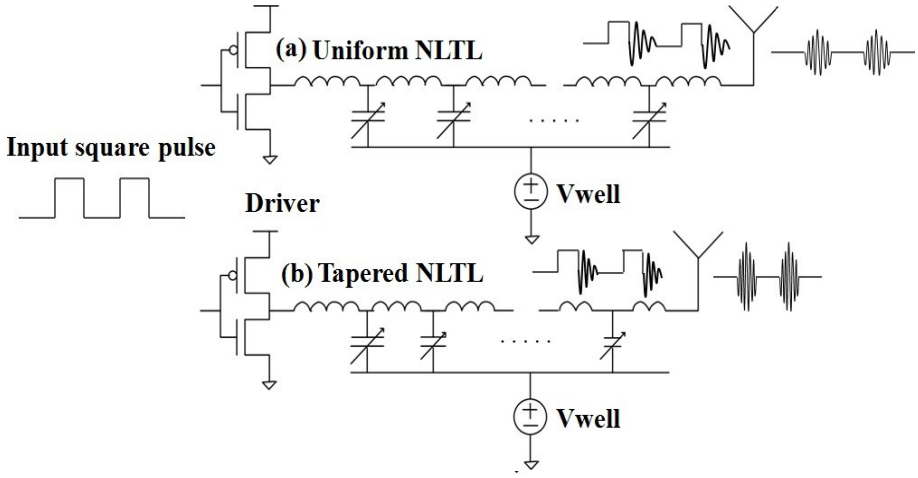

Figure 7-1. UWB transmitters with (a) Uniform NLTL; (b) Tapered NLTL with progressively smaller inductors and varactors. The baseband waveform drives the NLTL and the resulting sharpened edge and ringing are radiated by a suitable antenna.

7.2 Design Theory

The uniform NLTL transmitter architecture [5] is shown in Figure 7-1 (a). The NLTL generates microwave pulses by sharpening the falling edge of its input signal. By utilizing the bandpass characteristic of the antenna, the generated ringing close to the Bragg frequency can be radiated with the rejection of the baseband waveform. Similar to the uniform NLTL transmitter, the tapered design is also driven by a baseband waveform, as shown in Figure 7-1 (b). The difference is that the tapered NLTL uses a continuous progression of the Bragg frequencies along its unit cells, resulting in the reduced sizes of the inductance and varactor. The taper-down designs give higher Bragg ringing, because at the beginning stages where the fall edge is still long, larger varactor sharpens the fall time more. Close to the end of NLTL, smaller inductance and capacitance gives the desirable higher Bragg frequency.

a. Energy Consumption

According to [5], the capacitance charging energy is the main contribution of the energy required to create a pulse on the NLTL, which scales as:

$$E_{Ch} = N\left(V_L^2 + \eta V_H^2\right)\frac{1}{Z_0}\frac{1}{f_{bragg}} \tag{7.1}$$

where N is the total number of sections, Z_0 is the characteristic impedance of the NLTL, f_{bragg} is the Bragg frequency, V_H and V_L are the high and low voltages of the input pulse and η is the ratio of $C(V_H)/C(V_L)$. From (7.1), it can be found that E_{Ch} can be reduced by increasing f_{bragg} while keeping Z_0 constant to avoid the reflection loss. N needs to be sufficiently large to maintain the frequency conversion efficiency. The energy consumption of the NLTL can be minimized by tapering the Bragg frequency along its length. The input to the line uses a low f_{bragg} while the output uses a high f_{bragg}, resulting in gradually decreased inductance and varactor sizes, as shown in Figure 7-1 (b). There are several ways to implement the tapering. The straightforward function is the geometric progression of ratio k. If the first section's Bragg frequency is $f_{bragg,1}$, then the n^{th} section has:

$$f_{bragg,n} = f_{bragg,1}\, k^{n-1} \tag{7.2}$$

where $k > 1$. Substituting (7.2) into (7.1), the charging energy for the tapered NLTL can be reduced to:

$$E_{taper} = \frac{k^n - 1}{N\left(k^n - k^{n-1}\right)} E_{Ch} \tag{7.3}$$

b. Maximum Pulse Rate

In the NLTL configuration, the maximum pulse rate is limited by the time required to recharge the entire line. According to [5], the upper-bound on the pulse repetition frequency (PRF) is:

$$PRF = \frac{\pi f_{bragg}\ C(V_L)}{2N\ C(V_H)} \tag{7.4}$$

Therefore, the maximum PRF can also be increased by pushing up f_{bragg} of the NLTL cell with the tapering configuration.

7.3 Simulation Results

To examine the performance of the tapered NLTL transmitter, we use the lumped models of spiral-inductors and MOS varactors in IBM's 0.13μm RF-CMOS process. The first section's f_{bragg} is chosen to be 10 GHz. The inductor and capacitance values are designed to be 1.39 nH and 530 fF at a bias of –0.5 V. Considering the comprise between the generated pulse amplitude and charging energy, 9 sections is chosen as the length in the further simulations.

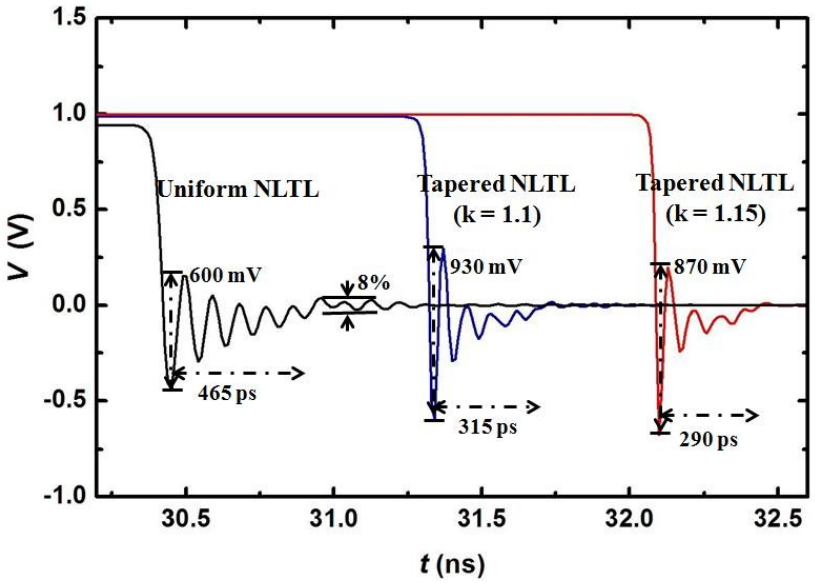

Figure 7-2. Simulated waveforms for the 10 GHz uniform and tapered NLTLs in IBM's 0.13μm RF-CMOS technology. The output is taken at an ideal 50Ω load.

The tapered NLTL transmitters with different k are simulated in the time-domain using Spectre. The input uses a 1.5 V square-wave with 100 ps rise/fall times. For comparison, the uniform NLTL transmitter is also simulated with $N = 9$ and $f_{bragg} = 10$ GHz. Waveforms at the output of the NLTLs are shown in Figure 7-2 with different delays when the output is terminated with a 50 Ω load. From Figure 7-2, we can find that all the resulting output waveforms show strong ringing on the falling edge despite of the small number of sections. For the uniform configuration, the peak-to-peak ringing amplitude is 600 mV and the main pulse duration is around 465 ps. After the main pulse, damped oscillation can be observed, which is due to impedance mismatch, as the NLTL's impedance varies significantly with both bias and frequency. Compared to the uniform structure, the ringing amplitudes of tapered NLTLs with k = 1.1 and 1.15 are increased to 930 mV and 870 mV. The decreasing pulse amplitude

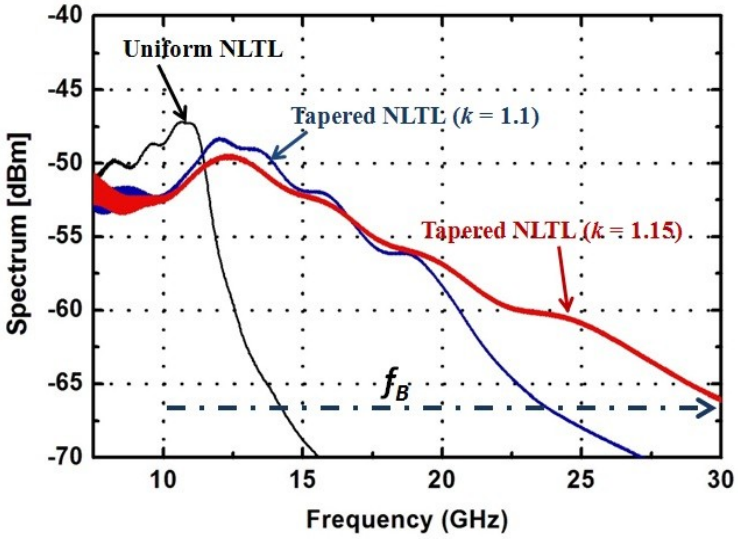

Figure 7-3. Simulated spectrums of the 10 GHz uniform and tapered NLTLs in IBM's 0.13μm RF-CMOS technology.

from k = 1.1 to k = 1.15 is due to the significant substrate and conductor loss experienced by high frequency components up to 30 GHz of the tapered one with k =1.15. In addition, the pulse duration is reduced to 315 ps and 290 ps, which gives higher maximum pulse rate.

Figure 7-3 shows the corresponding spectrums of the output waveforms. The spectrum of the uniform structure has a maximum –47 dBm at 10.7 GHz. For the tapered NLTLs, the peak spectrum powers are –49 dBm at 12 GHz and –50 dBm at 12.5 GHz, respectively. Since the tapered NLTLs increase the Bragg frequencies at the last stage up to 21 GHz and 30 GHz with k = 1.1 and 1.15, the energy is spread into much larger bandwidth, as show in Figure 7-3. Therefore, compared to the uniform one, the antennas for the tapered NLTLs should be made more broadband to radiate all

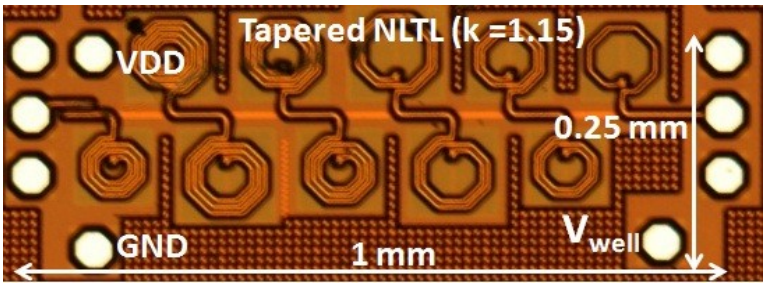

Figure 7-4. The die photograph of the 10 GHz device with tapered NLTL (k = 1.15).

the high frequency components for a full pulse shape, since the final transmitted waveform is very dependent on the bandwidth of the antennas.

To estimate the transmitter's energy consumption, we use a one-port S-parameter model of a UWB dipole antenna with a broadband response at 11 GHz. With each NLTL connected to the antenna load, we integrate the current supplied to the driving inverter over one transmission cycle to obtain the energy consumed per pulse. The resulting energy consumption follows our proposed scaling rule (Table 7-1), but differs from the ideal case of Eq (7.3) by roughly a factor of two. The additional energy consumption mainly comes from process dependent losses, such as the inductors' Q factor and internal transistor and varactor losses.

7.4 Experimental Results

The 10 GHz transmitters with uniform and tapered NLTLs (k = 1.1 and 1.15) are fabricated in IBM's 0.13 μm RF-CMOS technology. The die photograph of the 10 GHz device with k = 1.15 is shown in Figure 7-4. The total area of each transmitter is about 1mm × 0.25mm. The driving inverters are powered with a 1.5V supply and

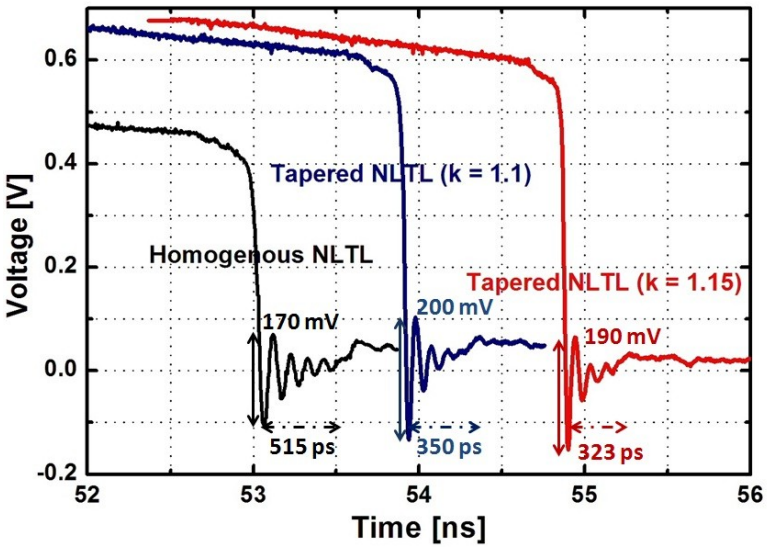

Figure 7-5. Measured waveforms for the 10 GHz uniform and tapered NLTLs in IBM's 0.13μm RF-CMOS technology.

input data are provided by Agilent 8133a with 60 ps nominal rise/fall times. When characterizing the transmission properties, the input waveform is a 10 ns square pulse from 0 V to 1.5 V with a 32 MHz repetition rate.

The pulse generation properties are verified by connecting the NLTL output to a high-speed sampling oscilloscope. Each device shows significant ringing on the falling edge as shown in Figure 7-5. The peak amplitudes are 170 mV, 200 mV, and 190 mV, respectively. Compared to the simulations, the reduced amplitudes are mostly due to propagation loss in the test-cables and RF probes.

The wireless transmission properties are also tested by connecting a 4 mm small monopole antenna to the wafer probe at the NLTL output, which provides broad impedance bandwidth above 10 GHz with return loss > 10 dB. The transmitted waveform is received by a TEM horn antenna and recorded with the high-speed sampling oscilloscope at a distance of 20 cm. Figure 7-6 shows the received decreased

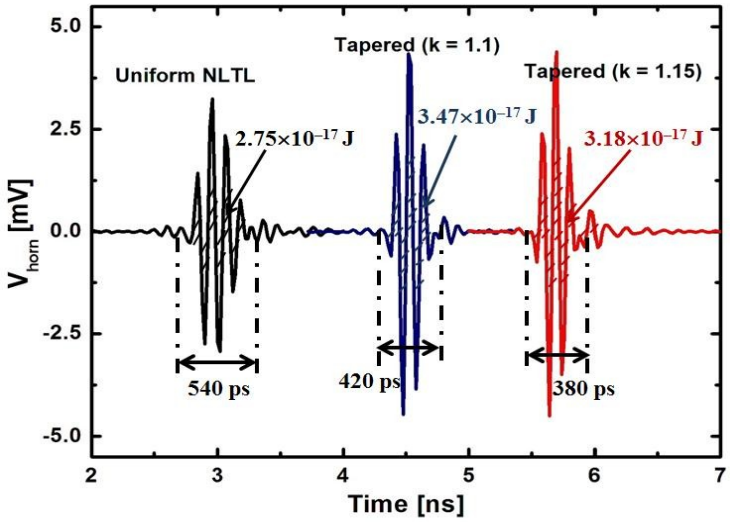

Figure 7-6. Received waveforms from the 10 GHz transmitters at the distance of 20 cm.

Device	Ideal [pJ]	Simulated [pJ]	Measured [pJ]
Uniform NLTL	10.91	23.62	24.65
Tapered NLTL (k = 1.1)	7.68	17.16	17.95
Tapered NLTL (k = 1.15)	6.65	14.89	15.57

Table 7-1. Energy-per-pulse for each device

from 540 ps to 380 ps with the center frequency around 10 GHz. The pulse magnitude and the energy contained in each pulse are also increased.

We then measure the energy consumption by driving the transmitters at a PRF of 32 MHz, and measuring their DC supply currents. The devices draw 526, 383, and 330 μA, respectively, from a 1.5 V supply. The resulting energy consumption of each transmitter is shown in Table 7-1 in terms of the energy per pulse. The measured

figures are very close to the simulated values. The best performing device in terms of energy is the tapered NLTL transmitter (k = 1.15) with 15 pJ/pulse.

7.5 Conclusion

A new IR-UWB transmitter based on the tapered NLTL is proposed. Compared to previous uniform NLTL configuration, the proposed transmitter is not only more power-efficient but also increases the allowable pulse rate. The transmitter shows a best energy performance of 15 pJ/pulse at a pulse rate of 32 MHz. This transmitter provides a potential solution for the low-power transmitter at or above10 GHz.

REFERENCES

[1] I. Oppermann, L. Stoica, A. Rabachin, Z. Shelby, and J. Haapola, "UWB wireless sensor networks: UWEN – A practical example," *IEEE Commun. Mag.*, vol. 42, pp. S27–S32, Dec. 2004.

[2] "Revision of Part 15 of the commission's rules regarding ultra-wideband transmission systems: First report and order," *Federal* Communications *Commission*, Washington, DC, ET-docket 98-153, FCC 02-48, 2002.

[3] A. T. Phan, J. Lee, V. Krizhanovskii, Q. Le, S.-k. Han, and S.-G. Lee, "Energy-efficient low-complexity CMOS pulse generator for multiband UWB impulse radio," *IEEE Transactions on Circuits and Systems I: Regular Papers*, vol. 55, no. 11, pp. 3552–3563, 2008.

[4] S. Bourdel, Y. Bachelet, J. Gaubert, O. Fourquin, and N. Dehaese, "A 9-pJ/Pulse 1.42-Vpp OOK CMOS UWB pulse generator for the 3.1-10.6-GHz FCC Band," *IEEE Transactions On Microwave Theory And Techniques*, vol. 58, no. 1, pp. 65–73, 2010.

[5] K. G. Lyon, F. Yu, and E. C. Kan, "A UWB-IR transmitter using frequency conversion in nonlinear transmission lines with 16pJ/Pulse energy consumption," *IEEE Transactions On Microwave Theory And Techniques*, vol. 58, no. 12, pp. 3617–3625, 2010.

CHAPTER 8

CONCLUSION

8.1 Summary of Major Contributions

The major contributions of the work described in this dissertation are summarized as follows:

1. Proposed a novel NLTL-based RFID transponder to solve the self-interference problem. Analytical modeling is developed to facilitate the design procedures. Both of the simulation and measurements of the NLTL prototypes show the efficient harmonic generation under small input power.
2. Proposed a novel harmonic RFID transponder based on the reflective NLTLs. By employing the single antenna configuration, the total footprint of the device can be reduced significantly without degradation in the harmonic conversion efficiency.
3. Effective data transmission between the reader and the tag is demonstrated using different antennas in both amplitude and phase modulation.
4. Designed a novel RFID tag consisting of reflective NLTL and model sensor varactor. Compared to conventional discrete load capacitance configuration, the proposed tag is able to achieve much larger phase variance, resulting in higher sensitivity for capacitive signal transduction.
5. A theoretical analysis on the frontend design of NLTL based digital RFID tag is performed to optimize the system performance under different conditions.

8.2 Lessons Learned

1. The fabricated NLTLs showed an increasing discrepancy of harmonic power between the simulation and the measurement results as f_{bragg} increased. This was mostly due to the parasitics resulting from the connections from the diode to the inductor/transmission line. Although the parasitics can't be eliminated completely, the effects of the layout connections can be modeled in electromagnetic simulation.
2. Since the reflective NLTLs showed resonant input matching performance, it is important to choose the operating frequency to achieve maximum harmonic power. After that, it requires the corresponding design of the resonant frequency of the antenna used for RFID tag. Otherwise, the received harmonic power by the reader would be greatly decreased.
3. Calibration is the essential step during the experiments. For the harmonic generation measurements, the cable loss needs to be compensated by increasing the output power of the signal generator. Otherwise, the measured harmonic power would be much lower than the expected value, since the conversion gain is proportional to the input power. It is also very important to do calibration for the wireless link demonstration. Because there are many other RF signals in the open measurement environment, like the industrial, scientific and medical (ISM) bands at 2.45 GHz, 5.8 GHz, and etc. The parasitic 2^{nd} harmonic from the signal generator (the reader) is another interfering signal, since its magnitude is comparable to the received harmonic signal from the NLTLs in the long reader-to-tag distance.

8.3 Suggestions for Future Work

1. Study the coupling effect between the fundamental and the harmonic waves in the harmonic generation analysis in the NLTLs. According to [1], power of different frequencies may convert from one to the other and the amplitude of the waves may vary exponentially or periodically depending on the relation of the frequencies and that of the phase constants between the propagating waves. By analyzing the phase condition effects on the coupling between the fundamental and the harmonic waves, the more sophisticated model will offer better understanding in the phase noise performance of the NLTLs.
2. Explore the frequency mixing property of the NLTLs for the multi-tag detection. For the multi-tag system, there would be a local low frequency oscillator to generate the frequency shift in the tag around several MHz. By mixing different frequency shift with the generated 2^{nd} harmonic, all tags can be detected simultaneously with different operation distance. The desirable tag can be distinguished by its corresponding frequency shift. The similar multi-tag idea based on the fundamental frequency has been presented in [2]. Its frequency shift is achieved by the digital phase shifter. The method using NLTLs may be a better candidate for its passive and compact properties.
3. Ranging and sensing abilities can be integrated together in the passive NLTL RFID sensor tag with analog phase modulation. By utilizing multiple frequency bands, the distance to the tag can be also estimated with the phase information of the 2^{nd} harmonic signal. This method would alleviate the multipath phase offset and the self-interference problem in the conventional RFID sensor tag.

4. Revise two-antenna configuration to one-antenna configuration in present NLTL based digital RFID tag. To reduce the whole system size, the reflective NLTL can be used in the digital RFID tag. By replacing the input impedance model of the matched NLTL with the reflective one, the frontend design theory in Section 6.2 can be applied to optimize the performance for different system.

REFERENCES

[1] P. K. Tien, "Parametric amplification and frequency mixing in propagating circuits," *J. Appl. Phys.*, vol. 29, no. 9, pp. 1347–1357, Sep. 1958.

[2] I. B. Shirokov, "The multitag microwave RFID system," *IEEE Transactions On Microwave Theory And Techniques*, vol. 57, no. 5, pp. 1362–1369, 2009.